

**$L1_0$ -Ordered Thin Films with  
High Perpendicular Magnetic Anisotropy for  
STT-MRAM Applications**

Submitted in partial fulfillment of the requirements for

the degree of

Doctor of Philosophy

in

Electrical and Computer Engineering

Efrem Yuan-Fu Huang

B.S.E., Electrical Engineering, Princeton University

Carnegie Mellon University  
Pittsburgh, PA

July, 2016

## Acknowledgements

The research discussed in this dissertation was supported by the Data Storage Systems Center (DSSC) and their industrial sponsors. I am very grateful for their financial support throughout my time at Carnegie Mellon University.

I would like to sincerely thank my advisor, Professor Mark H. Kryder, for his mentorship and insight over the last four years. The encouragement and advice he so generously provided have been invaluable throughout my research. His wealth of experience in both academia and industry has shaped my pursuit of the Ph.D. and, I am certain, my endeavors beyond Carnegie Mellon. It has truly been an honor and a privilege to work with Mark and to learn from his illustrious career.

I am very thankful to my committee members, Professor Jian-Gang (Jimmy) Zhu, Professor James A. Bain, and Professor Sara A. Majetich, for sharing their time and lending their expertise. The feedback and guidance they offered have been indispensable in completing my thesis. Their knowledge of both underlying scientific theory and state-of-the-art technology has been a valuable resource.

I greatly appreciate the support of Carnegie Mellon faculty and staff members, without whom this research would not have been possible. Their training and cooperation have allowed me to focus on the challenges of research. Special thanks to Prof. Andrzej Strojwas, James Rosvanis, Norman Gottron, Matthew Moneck, Carsen Kline, Chris Bowman, Andrew Gamble, Adam Wise, Jason Wolf, Tom Nuhfer, Jacqueline Chraska, Patricia Grieco, and Lauren Demby.

I want to thank several past and present students at Carnegie Mellon University for their friendship and assistance. Thanks to Vignesh Sundar, Hoan Ho, Abhishek Sharma, Hai Li, Xiaoyu Bai, Min Xu, David Bromberg, Ahmed Abdelgawad, Stephan Piotrowski, Varaprasad Bollapragada, and Mohamed Darwish for the many discussions, research-related and otherwise, that have helped me through the past four years. Thanks to my predecessors Chang Soo Kim and Steven Granz for not only laying the foundations for this work, but keeping in touch and offering advice well beyond their obligations.

Finally, I express my most heartfelt gratitude to my parents, Yung-Min Huang and Cybill Wei, and to my brother, Edward Huang. Their unconditional love and unwavering support have been there every step of the way. I dedicate this work to them.

## Abstract

The objective of the research conducted herein was to develop  $L1_0$ -ordered materials and thin film stack structures with high perpendicular magnetic anisotropy (PMA) for spin-transfer-torque magnetoresistive random access memory (STT-MRAM) applications. A systematic approach was taken in this dissertation, culminating in exchange coupled  $L1_0$ -FePt and  $L1_0$ -MnAl heterogeneous structures showing great promise for developing perpendicular magnetic tunnel junctions (pMTJs) with both high thermal stability and low critical switching current.

First, using MgO underlayers on Si substrates, sputtered MnAl films were systematically optimized, ultimately producing a Si substrate/MgO (20 nm)/MnAl (30)/Ta (5) film stack with a high degree of ordering and large PMA.

Next, noting the incompatibility of insulating MgO underlayers with industrial-scale CMOS processes, attention was turned to using conductive underlayers. TiN was found to excel at promoting growth of  $L1_0$ -MnAl, with optimized films showing improved magnetic properties over those fabricated on MgO underlayers.

Although the MnAl films grown on TiN underlayers on Si substrates demonstrated good magnetic properties, it was found that the high deposition and ordering temperatures contributed to high film roughness. In an effort to reduce ordering temperature and surface roughness of  $L1_0$ -MnAl films, adding other materials (Ni, C, and  $\text{SiO}_x$ ) to the MnAl film in conjunction with various underlayers was studied. MnAl:Ni films with a fixed 3 volume% Ni content deposited on TiN underlayers revealed that PMA was reduced compared to MnAl films, and surface roughness increased dramatically below the ordering temperature. MnAl:C films with 1

volume% C showed an increase in PMA, while C in excess of the solubility limit (1.7 atomic %) diffused to the grain edges, degrading PMA. MnAl:SiO<sub>x</sub> films demonstrated poor PMA.

The use of different post-annealing processes was then studied as an alternative to *in situ* annealing. Rapid thermal annealing (RTA) was found to produce PMA in films at lower annealing temperatures than tube furnace annealing, but tube furnace annealing produced films with higher maximum PMA than RTA. While annealed samples had lower surface roughness than those ordered by high *in situ* deposition temperatures, relying solely on annealing to achieve *L*<sub>10</sub>-ordering resulted drastically reduced PMA.

Since the material additions, underlayer systems, and annealing techniques studied either did not reduce film roughness or resulted in reduced PMA of thin films, attention was turned to MTJ stack structures employing heterogeneous material systems for top and bottom electrodes, which might produce film stacks with both high PMA and low surface roughness. As a way to potentially mitigate roughness issues with using MnAl-based thin films as both free and reference layers in an MTJ, exchange coupled heterogeneous structures were studied. Given the high PMA of *L*<sub>10</sub>-FePt and low damping of *L*<sub>10</sub>-MnAl, *L*<sub>10</sub>-FePt/MnAl heterogeneous structures were studied as a way to take advantage of STT potentially being a surface process. Unfortunately, depositing the MnAl at elevated temperatures resulted in interdiffusion between FePt and MnAl, and caused a degradation in PMA. High- and low-anisotropy thin films separated by a thin barrier were then examined in the form of in-plane hard-FePt/barrier layer/in-plane soft-FePt film stacks. It was found that significant exchange coupling energy was still observed at barrier thicknesses of around 1 nm. Since scaled MTJs have tunnel barriers below 1 nm, interlayer exchange coupling between the electrodes might thus be used for partially pinning the free layer, thereby increasing effective PMA. It is suggested that pinning a low-damping free

layer by a high-PMA reference layer may therefore result in an MTJ with both high effective PMA and low effective damping.

Finally, heterogeneous  $L1_0$ -ordered FePt/MgO/MnAl film stacks were explored for pMTJs. Film stacks with MgO barrier layers thinner than 2 nm showed significant interdiffusion between the FePt and MnAl, while film stacks with thicker MgO barrier layers exhibited good ordering and high PMA in both the FePt and MnAl films. It is believed that this limitation is caused by the roughness of the underlying FePt, which was thicker than 2 nm. Unfortunately, MgO barrier layers thinner than 2 nm are needed to make good MTJs.

With further study, thin, continuous barriers may be achievable for high-PMA,  $L1_0$ -ordered materials with more materials exploration, deposition optimization, and more advanced thin film processing techniques and fabrication equipment. Use of appropriate underlayers, capping layers, dopant elements, and improved fabrication techniques may help reduce surface roughness while preserving PMA. If smooth electrodes can be developed, the heterogeneous structures discussed have great potential in taking advantage of exchange coupling for developing pMTJs with both high thermal stability and low critical switching current.

# Table of Contents

Acknowledgements	ii
Abstract	iv
Table of Contents	vii
List of Figures	xi
Chapter 1 - Motivation and Background	1
1.1 Introduction	1
1.2 STT-MRAM Metrics	4
1.2.1 Retention and Scalability	4
1.2.2 Power and Speed	7
1.2.3 Non-Volatility and Endurance	9
1.3 STT-MRAM Applications	9
1.4 The Thesis	11
1.5 References	12
Chapter 2 - Fundamentals of $L1_0$ -Ordered Materials and STT-MRAM	13
2.1 Introduction	13
2.2 $L1_0$ -Ordering and Perpendicular Magnetic Anisotropy (PMA)	13
2.3 Comparing $L1_0$ -FePt and $L1_0$ -MnAl Thin Films	16
2.4 Magnetic Tunnel Junctions (MTJs) and Tunneling Magnetoresistance (TMR)	18

2.5 Spin-Transfer-Torque (STT) and Critical Switching Current	21
2.6 Summary	26
2.7 References	27
Chapter 3 - Experimental Methods and Equipment	28
3.1 Introduction	28
3.2 Thin Film Deposition	28
3.2.1 Leybold-Heraeus Z-400 Sputtering System #2	30
3.2.2 Custom 5-Target Sputtering System #2	31
3.3 Annealing	32
3.3.1 Micro Magnetics SpinTherm-1000 Magnetic Annealing System	32
3.3.2 AG Associates Heat Pulse Rapid Thermal Annealing System	32
3.3.3 Tube Annealing Furnace	33
3.4 Magnetic Characterization	34
3.4.1 Quantum Design Vibrating Sample Magnetometer (VSM)	34
3.4.2 Princeton Measurement Corp. Micromag 2900 Alternating Gradient Force Magnetometer (AGFM)	35
3.5 Microstructural and Physical Characterization	35
3.5.1 Philips X'Pert Pro X-Ray Diffractometer (XRD)	36
3.5.2 NT-MDT Solver Next Atomic Force Microscope (AFM)	37
3.5.3 NT-MDT NTegra Prima AFM	37
3.5.4 JEOL 2000EX Transmission Electron Microscope (TEM)	38
3.5.5 Philips Tecnai F20 Field Emission TEM	38
3.6 Summary	39

Chapter 4 - $L1_0$ -Ordered MnAl Thin Films on MgO Underlayers	40
4.1 Introduction	40
4.2 Experimental Details	41
4.3 Results and Discussion	43
4.4 Summary	50
4.5 References	52
Chapter 5 - $L1_0$ -Ordered MnAl Thin Films on Conductive Underlayers	54
5.1 Introduction	54
5.2 Experimental Details	55
5.3 Results and Discussion	56
5.4 Summary	65
5.5 References	67
Chapter 6 - Addressing MnAl Film Roughness	68
6.1 Introduction	68
6.2 Additions to MnAl Film	68
6.2.1 MnAl:Ni	69
6.2.2 MnAl:C	76
6.2.3 MnAl:SiO <sub>x</sub>	82
6.3 Post-Annealing Methods	83
6.3.1 Experimental Details	83
6.3.2 Results and Discussion	84
6.4 Summary	93

6.5 References	96
Chapter 7 - Exchange Coupled $L1_0$ -Ordered Magnetic Thin Films	97
7.1 Introduction	97
7.2 $L1_0$ -FePt/MnAl Heterogeneous Structures	97
7.2.1 Experimental Details	98
7.2.2 Results and Discussion	98
7.3 High- and Low-Anisotropy Thin Films Separated by a Thin Barrier	102
7.3.1 Experimental Details	103
7.3.2 Results and Discussion	104
7.4 Summary	114
7.5 References	117
Chapter 8 - FePt/MgO/MnAl Film Stacks for Perpendicular Magnetic Tunnel Junctions	118
8.1 Introduction	118
8.2 Experimental Details	118
8.3 Results and Discussion	119
8.4 Summary	124
8.5 References	125
Chapter 9 - Conclusion	126
9.1 Summary of Present Work	126
9.2 Conferences and Publications	129
9.3 Recommendations for Future Work	130
9.4 References	132

## List of Figures

<u>FIGURE</u>		<u>PAGE</u>
1-1	Example implementation of STT-MRAM with pMTJ (magnified) or in-plane MTJ.	2
1-2	Switching delay dependence on voltage applied across pMTJ.	8
1-3	Power-delay-product (PDP) dependence on voltage applied across pMTJ.	8
2-1	(a) The disordered fcc unit cell. All sites have equal occupation probability of the two (or more) atoms of the alloy and (b) the $L1_0$ structure showing the alternating stacking of (001) planes.	14
2-2	The three orientational domains or variants that form when an fcc crystal orders to $L1_0$ .	15
2-3	Schematic of simple MTJ structure with in-plane electrodes magnetized in parallel.	18
2-4	Electrons with spins aligned with the magnetized material pass through relatively unhindered, while electrons with spins misaligned encounter significant scattering.	19
2-5	Spin-dependent tunneling of electrons from one ferromagnetic electrode (FM) to another across a tunnel barrier (gray) for parallel (left) and antiparallel (right) magnetization configurations. Density of states for each scenario are shown on the bottom.	20
2-6	Two Current Model of TMR.	20
2-7	Magnetization dynamics of a macrospin $\mathbf{M}$ in the presence of an external field $\mathbf{H}$ .	22
3-1	Leybold-Heraeus Z-400 Sputtering System #2.	30
3-2	Custom 5-Target Sputtering System #2.	31
3-3	AG Associates Heat Pulse Rapid Thermal Annealing System.	33
3-4	Tube Annealing Furnace.	33

4-1	Out-of-plane $\theta/2\theta$ XRD patterns of 30 nm MnAl films deposited at various <i>in situ</i> substrate temperatures, 40 W DC power, and $T_a = 350$ °C.	44
4-2	Schematic of epitaxial growth relationship at MgO/ $\tau$ -MnAl interface.	44
4-3	Sputtering temperature dependence of (a) out-of-plane coercivity $H_c$ and squareness $M_r/M_s$ and (b) saturation magnetization $M_s$ and anisotropy constant $K_u$ of 30 nm MnAl films deposited using 40 W DC power and annealed at $T_a = 350$ °C.	45
4-4	Out-of-plane $\theta/2\theta$ XRD patterns of MnAl films with various thicknesses deposited using 40 W DC power, $T_s = 530$ °C, and $T_a = 350$ °C.	46
4-5	DC sputtering power dependence of (a) out-of-plane coercivity $H_c$ and squareness $M_r/M_s$ and (b) saturation magnetization $M_s$ and anisotropy constant $K_u$ of 30 nm MnAl films deposited at $T_s = 530$ °C, and $T_a = 350$ °C.	46
4-6	Magnetic annealing temperature dependence of (a) out-of-plane coercivity $H_c$ and squareness $M_r/M_s$ and (b) saturation magnetization $M_s$ and anisotropy constant $K_u$ (error bars indicate possible range of values adjusting for thickness of MnAl/Ta interdiffusion layer). 10 nm MnAl films were deposited using 40 W DC power and $T_s = 530$ °C.	47
4-7	(a) Out-of-plane/in-plane magnetic hysteresis loops and (b) 50,000 magnification TEM cross-sectional image of the Si substrate/MgO (20 nm)/MnAl (30)/Ta (5) film stack deposited using 40 W DC power, $T_s = 530$ °C, and $T_a = 350$ °C.	49
5-1	Sputtering temperature dependence of (a) out-of-plane coercivity $H_c$ and squareness $M_r/M_s$ and (b) saturation magnetization $M_s$ and anisotropy constant $K_u$ of 30 nm MnAl films deposited using 40 W DC power, 4 mTorr Ar gas pressure, and annealed at $T_a = 350$ °C.	57
5-2	Film thickness dependence of (a) out-of-plane coercivity $H_c$ and squareness $M_r/M_s$ and (b) saturation magnetization $M_s$ and anisotropy constant $K_u$ of MnAl films deposited at $T_s = 400$ °C using 40 W DC power and annealed at $T_a = 350$ °C.	58
5-3	Ar gas pressure dependence of (a) out-of-plane coercivity $H_c$ and squareness $M_r/M_s$ and (b) saturation magnetization $M_s$ and anisotropy constant $K_u$ of 30 nm MnAl films deposited at $T_s = 400$ °C using 40 W DC power and annealed at $T_a = 350$ °C.	59
5-4	(a) Out-of-plane $\theta/2\theta$ XRD pattern and (b) out-of-plane/in-plane magnetic hysteresis loops of the Si substrate/TiN (10 nm)/MnAl (50)/Ta (5) film stack deposited using 1 mTorr Ar gas pressure, $T_s = 400$ °C, and	60

$T_a = 350$  °C.

5-5	TEM cross-sectional image of the Si substrate/TiN (10 nm)/MnAl (30)/Ta (5) film stack deposited using 1 mTorr Ar gas pressure, $T_s = 400$ °C, and $T_a = 350$ °C.	61
5-6	RMS roughness values after each film layer from AFM measurements.	62
5-7	Root-mean-square surface roughness of films with varying MnAl film thicknesses.	63
5-8	MgTiO underlayer thickness dependence of out-of-plane coercivity $H_c$ and squareness $M_r/M_s$ of Si substrate/TiN (10 nm)/MgTiO (0-20)/MnAl (10) film stacks deposited at $T_s = 400$ °C and annealed at $T_a = 350$ °C.	64
5-9	TEM cross-sectional image of the Si substrate/TiN (10 nm)/MgTiO (10)/MnAl (10) film stack deposited at $T_s = 400$ °C and annealed at $T_a = 350$ °C.	64
6-1	Sputtering temperature dependence of out-of-plane coercivity $H_c$ and root-mean-square surface roughness $R_q$ of 5 nm MnAlNi films.	71
6-2	AFM surface contour plot of 5 nm MnAlNi film deposited at $T_s = 500$ °C.	71
6-3	MnAlNi film thickness dependence of out-of-plane coercivity $H_c$ and root-mean-square surface roughness $R_q$ of Si substrate/TiN (15 nm)/MgTiO (0.9 nm)/MnAlNi (10-100 nm) film stacks deposited at $T_s = 400$ °C.	72
6-4	MgTiO underlayer thickness dependence of out-of-plane coercivity $H_c$ and saturation magnetization $M_s$ of Si Substrate/TiN (15 nm)/MgTiO (0-10)/MnAlNi (5) film stacks.	73
6-5	TEM cross-sectional image of the Si/TiN (15 nm)/MgTiO (2)/MnAlNi (5) film stack.	74
6-6	CrRu underlayer thickness dependence of out-of-plane coercivity $H_c$ and squareness $M_r/M_s$ of Si substrate/CrRu (0-10 nm)/MnAlNi (5) film stacks.	74
6-7	CrRu underlayer thickness dependence of out-of-plane coercivity $H_c$ and squareness $M_r/M_s$ of Si substrate/TiN (15 nm)/CrRu (0-10)/MnAlNi (5) film stacks.	76
6-8	Carbon volume percentage dependence of out-of-plane coercivity $H_c$ and root-mean-square surface roughness $R_q$ of 10 nm MnAl:C films with MnAl deposited first.	78

6-9	Carbon volume percentage dependence of out-of-plane coercivity $H_c$ and root-mean-square surface roughness $R_q$ of 10 nm MnAl:C films with C deposited first.	79
6-10	TEM cross-sectional image of a 10 nm MnAl:1%C film with C deposited first.	79
6-11	TEM cross-sectional image at TiN/MnAl:C interface of a 10 nm MnAl:1%C film with C deposited first.	80
6-12	TEM cross-sectional image at dark/light boundary of a 10 nm MnAl:1%C film with C deposited first.	80
6-13	SiO <sub>x</sub> volume percentage dependence of out-of-plane coercivity $H_c$ and root-mean-square surface roughness $R_q$ of 10 nm MnAl:SiO <sub>x</sub> films deposited on buffer HF-cleaned Si substrate/TiN (15 nm).	82
6-14	TEM cross-sectional image of the natively oxidized Si/MnAl (5 nm) film deposited at room temperature and annealed with RTA at $T_a = 650$ °C.	85
6-15	Annealing temperature dependence of out-of-plane coercivity $H_c$ of natively oxidized Si/MnAl (5 nm) films deposited at room temperature and annealed with rapid thermal annealing (RTA) or tube furnace (TF).	85
6-16	Annealing temperature dependence of out-of-plane coercivity $H_c$ of natively oxidized Si/MnAl (15 nm) films deposited at room temperature and annealed with rapid thermal annealing (RTA) or tube furnace (TF).	86
6-17	Annealing temperature dependence of out-of-plane coercivity $H_c$ of buffer HF-cleaned Si/MnAl (10 nm) films deposited at room temperature and annealed with rapid thermal annealing (RTA) or tube furnace (TF).	87
6-18	Annealing temperature dependence of out-of-plane coercivity $H_c$ of natively oxidized Si/TiN (10 nm)/MnAl (5) films deposited at room temperature and annealed with rapid thermal annealing (RTA) or tube furnace (TF).	89
6-19	Annealing temperature dependence of out-of-plane coercivity $H_c$ of natively oxidized Si/TiN (10 nm)/MnAl (5) films deposited at $T_s = 200$ °C and annealed with rapid thermal annealing (RTA) or tube furnace (TF).	89
6-20	TEM cross-sectional image of the natively oxidized Si/TiN (10 nm)/MnAl (5) film stack deposited at room temperature and annealed with tube furnace at $T_a = 900$ °C.	90

6-21	TEM cross-sectional image of TiN in natively oxidized Si/TiN (10 nm)/MnAl (5) film stack deposited at room temperature and annealed with tube furnace at $T_a = 900$ °C.	90
6-22	Annealing temperature dependence of $H_c$ of buffer HF-cleaned Si/TiN (10 nm)/MnAl (10) films deposited at $T_s = 200$ °C and annealed with RTA or tube furnace (TF).	91
6-23	Annealing temperature dependence of $H_c$ of buffer HF-cleaned Si/TiN (10 nm)/MnAl (10) films deposited at $T_s = 300$ °C and annealed with RTA or tube furnace (TF).	91
6-24	Maximum values of out-of-plane coercivity $H_c$ for MnAl film stacks annealed at various temperatures with RTA (red crosses) and tube furnace (TF, black circles).	93
7-1	Out-of-plane/in-plane magnetic hysteresis loops of the baseline Si substrate/MgO (20 nm)/FePt (10) film stack.	99
7-2	MnAl sputtering temperature dependence of out-of-plane coercivity $H_c$ and saturation magnetization $M_s$ of Si Substrate/MgO (20 nm)/FePt (10)/MnAl (30) film stacks.	99
7-3	MnAl thickness dependence of out-of-plane coercivity $H_c$ and saturation magnetization $M_s$ of Si Substrate/MgO (20 nm)/FePt (10)/MnAl (0-50) film stacks deposited at 425 °C.	101
7-4	Experimental model for intergranular region of perpendicular HAMR media using in-plane film stack structure.	102
7-5	TEM cross-sectional image of Si substrate/FePt (10 nm)/Cr (1)/FePt (9.4)/Ta (5) film stack.	105
7-6	(a) In-plane $\theta/2\theta$ XRD pattern and (b) In-plane (thick, black) versus out-of-plane (thin, red) magnetic hysteresis loops for hard FePt (10 nm)/MgO (20 nm).	105
7-7	Idealized in-plane magnetic hysteresis loop showing shift in reversal field $H_{\text{shift}} = H_r - H_{r,0}$ .	106
7-8	(a) In-plane measured temperature dependence of saturation magnetization and coercivity and (b) In-plane room temperature magnetic hysteresis loop for Si substrate/MgO (20 nm)/soft FePt (9.4) film stack.	107
7-9	In-plane magnetic hysteresis loops for film stack with 1.0 nm Cr barrier layer at various temperatures.	108

7-10	In-plane magnetic hysteresis loops for film stack with 1.0 nm TaO <sub>x</sub> barrier layer at various temperatures.	109
7-11	In-plane magnetic hysteresis loops for film stack with 1.0 nm SiO <sub>x</sub> barrier layer at various temperatures.	110
7-12	Exchange coupling energy density vs. measurement temperature for (a) 1.0 nm barrier layer, (b) TaO <sub>x</sub> , (c) SiO <sub>x</sub> , and (d) Cr.	111
7-13	Thickness dependence of interlayer exchange coupling energy density for various barrier layer materials.	113
7-14	Enlarged view of antiferromagnetic behavior shown in hysteresis loop of film stack with 0.5 nm TaO <sub>x</sub> barrier layer at 700 K.	113
8-1	Out-of-plane magnetic hysteresis loops of buffer HF-cleaned Si substrate/MgO (5 nm)/FePt (10)/MgO (0.25-5)/MnAl (10) film stacks with varying MgO barrier layer thickness.	120
8-2	MgO barrier layer thickness dependence of saturation magnetization $M_s$ of buffer HF-cleaned Si substrate/MgO (5 nm)/FePt (10)/MgO (0.25-5)/MnAl (10) film stacks.	120
8-3	Cross-sectional TEM image of buffer HF-cleaned Si substrate/MgO (5 nm)/FePt (10)/MgO (1)/MnAl (10) film stack.	121
8-4	Cross-sectional TEM image of buffer HF-cleaned Si substrate/MgO (5 nm)/FePt (10)/MgO (1)/MnAl (10) film stack showing large FePt grains and high film roughness.	121
8-5	Cross-sectional TEM image of buffer HF-cleaned Si substrate/MgO (5 nm)/FePt (10)/MgO (2)/MnAl (10) film stack.	122
8-6	Calculated MnAl contribution to out-of-plane magnetic hysteresis loops of buffer HF-cleaned Si substrate/MgO (5 nm)/FePt (10)/MgO (0.25-5)/MnAl (10) film stacks.	123

# Chapter 1

## Motivation and Background

### 1.1. Introduction

The demand for data storage has been doubling every 18 months and will grow to more than 40,000 exabytes by 2020, up from 3,500 exabytes in 2013 [1]. By 2020, 61% of shipped storage is projected to be for cloud storage, where each file is replicated four times on average [2]. The ubiquitous hard drive disk (HDD) has been integral to computing since 1956, but recently the areal density growth rate has slowed to less than 40% per year as perpendicular recording is approaching fundamental limits, and a change in technology to heat-assisted magnetic recording (HAMR) is likely in the future. Flash memory has found its way into many portable devices, but its cost per megabyte and fundamental limits prevent it from ever becoming a main form of storage [3]. Various alternatives are therefore being pursued. Identified by the Emerging Research Devices Group of the International Technology Roadmap for Semiconductors [4] as one of the two most promising non-volatile memory (NVM) technologies, spin-transfer-torque magnetoresistive random access memory (STT-MRAM) has the potential for 4 nm scaling, low power consumption, nanosecond switching speeds, CMOS compatibility, storage class retention, and multi-level cell (MLC) capability. A possible implementation is shown in FIG. 1-1, adapted from reference [5].



manufacturing processes. Additionally, since the operating parameters for STT-MRAM devices (e.g. switching speed and power consumption, retention time, etc.) can be tailored through material selection and design geometry, the technology can be engineered to meet a wide range of specifications. This design flexibility is particularly valuable as devices become more specialized and application-focused.

However, despite the great potential of STT-MRAM and the amount of research effort invested, significant challenges must still be overcome. Most notably, a perpendicular magnetic tunnel junction (pMTJ) with high thermal stability and low critical switching current will be necessary for the realization of scalable STT-MRAM, and appropriate materials and film stack structures must be developed.

In this chapter, a brief overview of metrics relevant to STT-MRAM is provided and the relationships and design tradeoffs among them are discussed (Section 1.2). The most promising applications for STT-MRAM are also highlighted and the most important metrics for each application are suggested (1.3). Lastly, the thesis is presented and the dissertation is outlined (1.4).

## 1.2. STT-MRAM Metrics

To understand the advantages and disadvantages of STT-MRAM, it is helpful to analyze the technology in terms of several performance attributes: retention, scalability, power, speed, non-volatility, and endurance. Kryder and Kim [3], [7] provide a thorough comparison of various emerging memory technologies using similar parameters. In this section, these metrics are introduced and their dependencies are discussed.

### 1.2.1 Retention and Scalability

Retention time is a measure of how long a storage device can hold information in a retrievable state. Due to thermal perturbations, small ferromagnetic volumes can randomly flip magnetic directions. Following the Maxwell-Boltzmann model for activation energy, the probability per unit time  $p$  of a reaction occurring is given by

$$p = f_0 e^{-\frac{E_b}{k_B T}}$$

Equation 1-1

where  $f_0 \approx 10^9$  Hz is the attempt frequency per unit time,  $E_b$  is the reaction energy barrier, and  $k_B T$  is the average thermal energy of the system. For a magnetic element of volume  $V$  and uniaxial anisotropy constant  $K_u$ , the anisotropy energy is  $E_a = K_u V \sin^2 \theta$ . When there is no field present, the energy minima occur at  $\theta = 0^\circ$  and  $\theta = 180^\circ$  ( $E_i = 0$ ), while the energy maximum occurs at  $\theta = 90^\circ$  ( $E_f = K_u V$ ). For the magnetization to switch from one easy axis

direction to the opposite direction requires overcoming this energy maximum, so the energy barrier is  $E_b = E_f - E_i = K_u V$ . This leads to a thermally activated switching probability of

$$p = f_0 e^{-\frac{K_u V}{k_B T}}$$

Equation 1-2

Let  $n^+$  denote the proportion of moments in the arbitrarily “positive” direction, and  $n^-$  denote the proportion of moments in the arbitrarily “negative” direction, the overall normalized moment of the domain in the positive direction is  $m = n^+ - n^-$ . The instantaneous change in moment is given by its derivative

$$\frac{dm}{dt} = \frac{dn^+}{dt} - \frac{dn^-}{dt}$$

Equation 1-3

In the absence of an applied field, the probabilities of switching to and from either direction are the same, simply  $p$ , which gives

$$\begin{aligned} \frac{dm}{dt} &= (pn^- - pn^+) - (pn^+ - pn^-) \\ &= 2pn^- - 2pn^+ \\ &= 2p(n^- - n^+) \\ &= -2pm \end{aligned}$$

Equation 1-4

Solving this first order differential equation yields the solution

$$\frac{m(t)}{m_0} = \exp\left(-2tf_0 e^{-\frac{K_u V}{k_B T}}\right)$$

Equation 1-5

This ratio indicates the proportion of the overall moment retained after time  $t$  has passed. For example, in order for a magnetic volume to have at least 75% retention after 10 years, a conventional magnetic storage benchmark, solving EQ. 1-5 gives the inequality

$$K_u V \geq 40k_B T$$

Equation 1-6

Plugging in  $k_B = 1.38 \times 10^{-16} \text{ erg/K}$  and  $T = 300 \text{ K}$  gives  $K_u V \geq 1.656 \times 10^{-12} \text{ erg}$ . As one can see, this sets a lower bound on the anisotropy-volume product. For a pMTJ cell with free layer volume of  $V = 100 \text{ nm}^3$ , this sets a lower limit on the anisotropy constant as  $K_u \geq 1.656 \times 10^7 \text{ erg/cm}^3$ . For any fixed retention benchmark, magnetic volume and anisotropy constant are inversely related. Therefore, the smaller the device is to be scaled, the higher the anisotropy of the material must be. Nevertheless, practical STT-MRAM applications are unlikely to require 10 years of thermal stability. Instead, the retention and scalability requirements will depend on the specific role of STT-MRAM in each system.

## 1.2.2 Power and Speed

The power consumption of pMTJ cell in an STT-MRAM device is given by Ohm's Law  $P = I^2R$ . Specifically, the maximum current passed through the junction is the critical switching current. Given the second order dependency of the power on current, minimizing the critical switching current is crucial for low-power operation. Several factors affect the critical switching current, including the effective damping parameter and the  $K_uV$  of the free layer, discussed further in Section 2.4. The resistance is often characterized in terms of the resistance-area (RA) product of the junction. Minimizing fabrication defects and using high-conductivity electrodes, underlayers, and capping materials can all help to reduce the RA product of an MTJ.

The speed of an MTJ is limited by magnetization dynamics. In a real application, an STT-MRAM device is expected to have a read/write time on the order of 10 ns [3]. While an MTJ's speed can be increased by applying a higher voltage (equivalently a larger switching current, according to  $V = IR$ ), as seen in FIG. 1-2, the second order dependence of power on voltage makes this a costly tradeoff, as illustrated in FIG. 1-3. Nevertheless, this may be a viable option depending on the application.

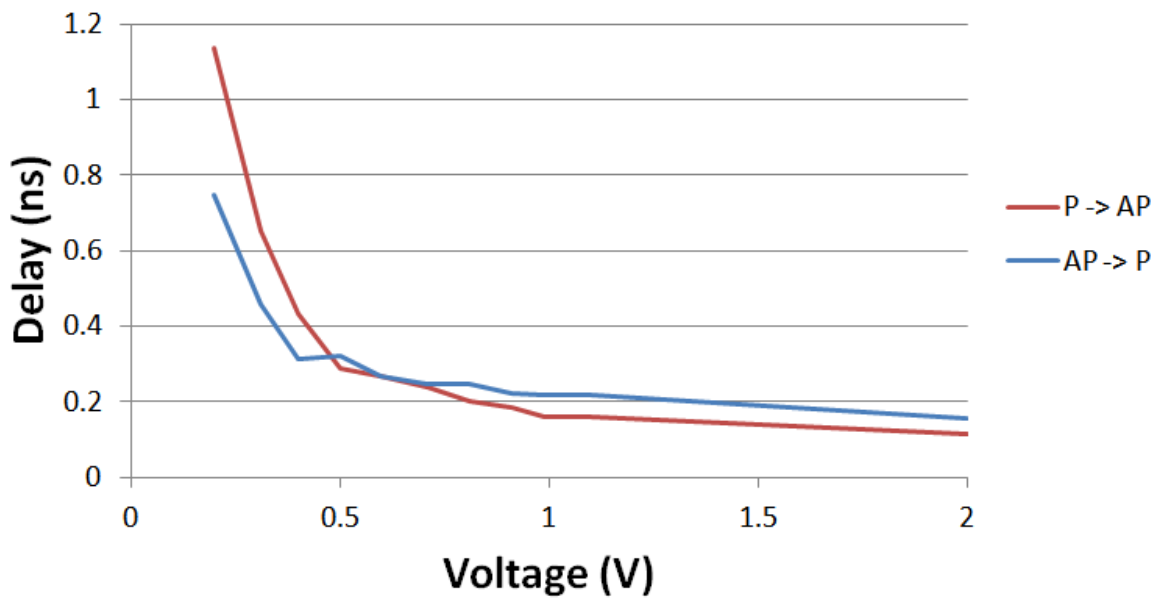


Figure 1-2 Switching delay dependence on voltage applied across pMTJ.

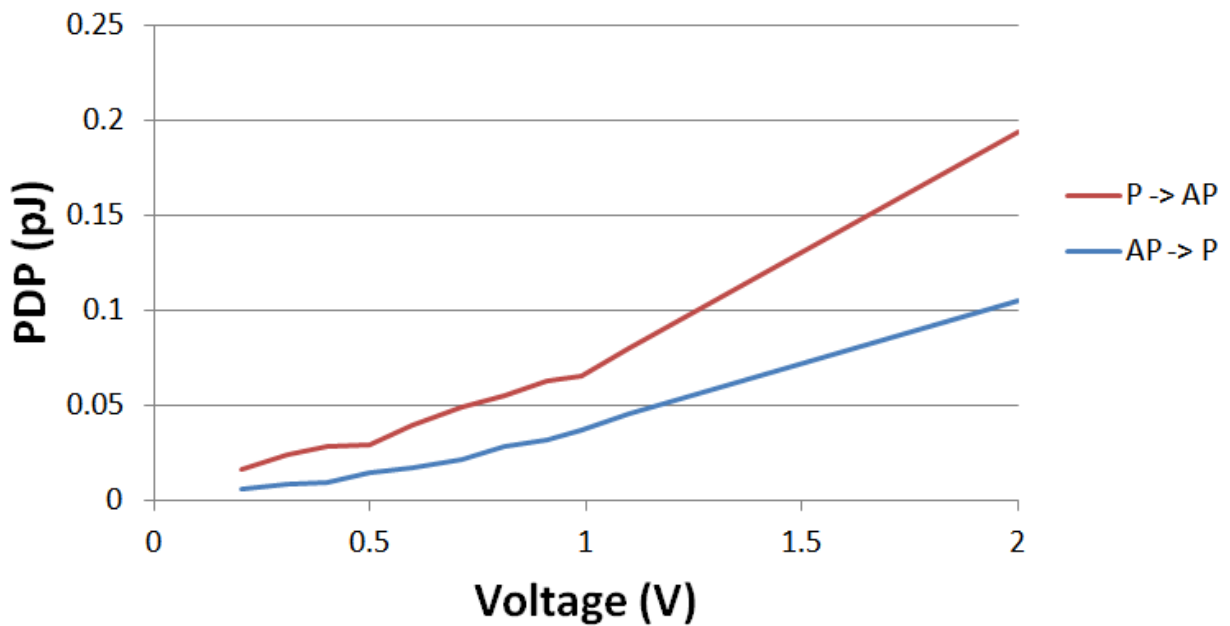


Figure 1-3 Power-delay-product (PDP) dependence on voltage applied across pMTJ.

### **1.2.3 Non-Volatility and Endurance**

As a non-volatile memory (NVM), STT-MRAM can retain stored data even when no power is supplied to the devices. This is in contrast to DRAM technology, in which data is stored in leaky capacitors and requires frequent read-write refresh cycles to maintain stored information. Instead, information is stored in magnetic states in STT-MRAM, which do not require refresh operations. This not only allows instant-on return from “deep sleep” states when used in computation, but confers significant power savings by avoiding the power-intensive refresh operations required in DRAM technology.

Endurance is the measure of how many times a storage device can be accessed before unfixable degradation occurs. Since STT-MRAM is electrically controlled and involves switching of magnetic moments rather than mechanical components, endurance is practically unlimited. Issues familiar to the semiconductor industry such as electromigration of contacts and vias or degradation of the underlying access device are more likely to be the limiting factor.

### **1.3. STT-MRAM Applications**

For data storage, STT-MRAM has great potential as a NAND flash replacement, particularly for ultra-low-power mobile platforms. The low power consumption and non-volatility of STT-MRAM is very attractive for Internet-of-Things applications, often envisioned as a vast network of numerous low-power, low-performance sensors and devices. In such a system, the high density of pMTJ-based STT-MRAM would reduce costs and still meet the performance needs of the application. STT-MRAM could also be useful as storage in applications valuing reliability over speed. For example, automotive, aeronautic, and space applications emphasize safety and availability of the system over performance. Unlike charge-

trap devices such as flash, STT-MRAM stores information in magnetic material, which can be engineered to be robust against extreme temperatures, radiation, and other environmental factors. These attributes are very attractive for mission critical, environmentally sensitive applications.

For computation memory, STT-MRAM has advantages for use as high-density memory for replacing or supplementing DRAM. The maturation of 3D integration with through-silicon-vias (TSVs) will enable ultra-high-bandwidth stacked memory chips, possibly even situated directly above processor cores. Intel's recently announced 3D-XPoint technology also offers another implementation of integrating STT-MRAM into computation. Compared to DRAM, STT-MRAM potentially has higher density, lower power, and higher speeds. Going one step down the memory hierarchy, STT-MRAM can potentially be tuned for use as high-level cache. In such an application, long-term retention is not necessary, and the design tradeoffs discussed in Section 1.2 can be applied to tailor STT-MRAM for both high density and high-speed performance.

## 1.4. The Thesis

The objective of the research presented in this dissertation is to develop  $L1_0$ -ordered materials and thin film stack structures with high perpendicular magnetic anisotropy (PMA) for spin-transfer-torque magnetoresistive random access memory (STT-MRAM) applications.

The dissertation is divided into nine chapters. Chapter 1 introduces STT-MRAM, provides an overview of relevant metrics, and identifies promising applications. Chapter 2 discusses the theories behind  $L1_0$ -ordered ferromagnetic materials, magnetic tunnel junctions (MTJs), and spin-transfer-torque (STT). Chapter 3 describes the experimental methods and equipment used throughout the research. In Chapter 4, the development of  $L1_0$ -ordered MnAl thin films with high PMA on Si substrates using MgO underlayers is described. Chapter 5 describes the development of  $L1_0$ -ordered MnAl thin films with high PMA on Si substrates using conductive underlayers. In Chapter 6, the effectiveness of material additions, various underlayers in conjunction with material additions, and post-annealing methods in reducing ordering temperature and film roughness of MnAl thin films is investigated. In Chapter 7, exchange coupled heterogeneous FePt/MnAl films and hard-FePt/barrier/soft-FePt structures are investigated. Chapter 8 explores FePt/MgO/MnAl film stacks for pMTJs. Finally, Chapter 9 provides a summary and recommendations for future work.

## 1.5. References

- [1] “The Digital Universe in 2020: A Universe of Opportunities and Challenges.” IDC study sponsored by EMC, Dec-2012.
- [2] “The Demand for Storage Devices in a Connected World of Data.” Seagate Technology LLC.
- [3] M. H. Kryder and C. S. Kim, “After Hard Drives-What Comes Next?,” *IEEE Trans. Magn.*, vol. 45, no. 10, pp. 3406–3413, Oct. 2009.
- [4] “Emerging Research Devices.” International Technology Roadmap for Semiconductors, 2011.
- [5] G. Hilson, “Avalanche Samples Spin Transfer Torque Magnetic RAM,” *EE Times*, 13-Jul-2015.
- [6] IBM, “Storage Class Memory: Towards a disruptively low-cost solid-state non-volatile memory,” IBM Almaden Research Center, Jan-2013.
- [7] C. S. Kim, “Feasibility of a Multi-bit Cell Perpendicular Magnetic Tunnel Junction Device,” Ph.D. Dissertation, Carnegie Mellon University, Pittsburgh, PA, 2013.
- [8] E. Y. Huang, M. O. Darwish, A. A. Sharma, and J. A. Weldon, “Spin-Transfer-Torque Based Magnetic Tunnel Junctions for Logic Applications - Document,” presented at the 18-819K Course Project, 2016.

## Chapter 2

# Fundamentals of $L1_0$ -Ordered Thin Films and STT-MRAM

### 2.1. Introduction

In order to appreciate the advantages and challenges of using  $L1_0$ -ordered thin films for STT-MRAM applications, it is first necessary to grasp the relevant underlying theories. In this chapter, the theoretical foundations useful for understanding the rest of the dissertation are presented, starting with an examination of  $L1_0$ -ordering and perpendicular magnetic anisotropy (Section 2.2), followed by an introduction to magnetic tunnel junctions and tunneling magnetoresistance (2.3), and finally concluding with spin-transfer-torque and critical switching current (2.4).

### 2.2. $L1_0$ -Ordering and Perpendicular Magnetic Anisotropy (PMA)

$L1_0$ -ordered alloys have crystal structures geometrically identical to those of face-centered-cubic (fcc) crystal structures, but instead of a random distribution of each element among the lattice sites,  $L1_0$ -ordered materials have alternating layers of each element. This difference is illustrated in FIG. 2-1, reproduced from reference [1]. Such a structure is also known as the CuAu structure. In addition to breaking symmetry, ordering can distort the lattice geometry. For example, certain pairings of elements in  $L1_0$ -ordered structures have a compressed  $c$ -axis and increased  $a$ -axis, exhibiting magnetocrystalline anisotropy. The resulting anisotropy is typically uniaxial along the [001]  $c$ -axis. For crystals exhibiting ferromagnetic behavior, the

magnetic easy axis is oriented across the alternating planes of elements. However, an  $L1_0$ -ordered crystal can be textured in one of three ways, shown in FIG. 2-2. In the context of thin films, both the second and third orientations would produce in-plane magnetic anisotropy, with only the first orientation demonstrating perpendicular magnetic anisotropy (PMA). Nonetheless, well-ordered  $L1_0$ -Fe- and  $L1_0$ -Mn-based alloys are known to show extremely high PMA, with anisotropy constant  $K_u > 10^7$  erg/cm<sup>3</sup>. In these alloys, the anisotropy is understood as arising from crystal field interactions and spin-orbit coupling [1]–[3].

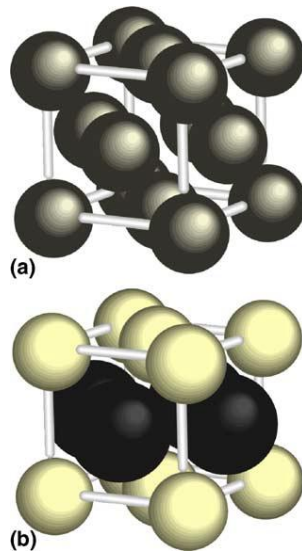


Figure 2-1 (a) The disordered fcc unit cell. All sites have equal occupation probability of the two (or more) atoms of the alloy and (b) the  $L1_0$  structure showing the alternating stacking of (001) planes [1].

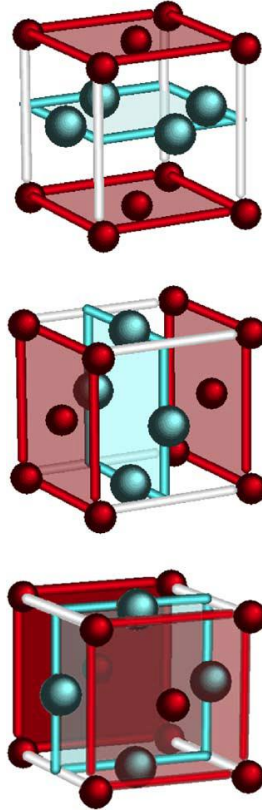


Figure 2-2 The three orientational domains or variants that form when an fcc crystal orders to  $L1_0$  [1].

One of the most well-studied  $L1_0$ -ordered materials is FePt, due to its application potential for heat-assisted-magnetic-recording (HAMR) media. The existing body of work shows that a substrate or underlayer with atomic configurations similar to that of  $L1_0$ -FePt is critical for promoting subsequent  $L1_0$ -ordering in FePt films. However, while MgO (001) single crystal substrates have proven especially useful in this role, the high material cost prohibits this from being a practical commercial solution. Instead, MgO underlayers, deposited under appropriate conditions, have been widely used to seed the growth of  $L1_0$ -FePt [4]–[6]. In an attempt to further improve the ordering of  $L1_0$ -FePt films, Ding et al. found that underlayers with slightly larger  $a$ -axis lattice parameters was advantageous for growing out-of-plane  $L1_0$ -FePt [5]. It is believed that since the  $L1_0$ -FePt  $a$ -axis is longer than its  $c$ -axis, the expanded lattice of the

underlayer favors growth of the  $L1_0$ -FePt  $a$ -axis rather than the  $c$ -axis. This ensures the anisotropy of the film lies out-of-plane. Using different underlayers can produce dramatically different results in ordering subsequent films, with a number of underlayers examined in Chapter 4, Chapter 5, and Section 6.2.

In addition to underlayers, thermal treatment is also a crucial process for achieving  $L1_0$ -ordering and improving PMA in films. Both *in situ* deposition temperature and post-annealing techniques are useful for ordering films, with favorable temperatures and exposure durations highly dependent on various factors, such as substrate, underlayer, material, film thickness, etc. Several thermal treatment techniques are studied in Chapter 4, Chapter 5, and Section 6.3.

Lastly, the addition of other materials into the film can assist  $L1_0$ -ordering and enhance PMA. Such techniques have been used extensively in HAMR media research, with added materials and proportions varying widely [4], [7]. The effects of adding materials to  $L1_0$ -ordered films are investigated in Section 6.2.

### **2.3. Comparing $L1_0$ -FePt and $L1_0$ -MnAl Thin Films**

Given the large ongoing effort in developing smooth  $L1_0$ -FePt thin films for use in HAMR media, several of the techniques effective at achieving  $L1_0$ -ordering and reducing film roughness may also be applicable to MnAl thin films, which are the focus of much of this dissertation. Both materials have similar lattice structures and have been shown to grow high-PMA films on similar underlayers (MgO, TiN). Employing underlayers with an elongated  $a$ -axis appears to favor out-of-plane orientation over in-plane. This is due to the  $c$ -axis of both  $L1_0$ -FePt and  $L1_0$ -MnAl being smaller than the  $a$ -axis, with an out-of-plane structure having better lattice matching with the underlayer than an in-plane structure. This phenomenon is observed in

Chapters 4 and 5 with the shift from MgO underlayers (a-axis lattice parameter of 4.2 Å) to TiN underlayers (a-axis lattice parameter of 4.3 Å). Whereas films deposited on MgO exhibited significant in-plane magnetic coercivity, films deposited on TiN showed no appreciable in-plane coercivity. The film morphology and roughness values observed in this work were also similar to those found in the literature on FePt.

However, there are also important differences between  $L1_0$ -FePt and  $L1_0$ -MnAl.  $L1_0$ -MnAl, also known as the  $\tau$ -phase of MnAl, is metastable. Bulk  $\tau$ -MnAl is achieved martensitically by cooling the material from the nonmagnetic  $\varepsilon$ -phase. In thin films, on the other hand,  $\tau$ -MnAl can be stable if deposited under the appropriate conditions. Depositing MnAl thin films at a temperature below that favorable for  $L1_0$ -ordering produces amorphous films, while deposition at too high of a temperature produces the nonmagnetic  $\varepsilon$ -phase. Both amorphous and nonmagnetic  $\varepsilon$ -phase are observed in Chapter 4. In contrast,  $L1_0$ -FePt is a stable phase, meaning it can be achieved if the material is held under favorable conditions for a sufficient period of time.  $L1_0$ -FePt thin films are ordered from the face-centered-cubic phase, with a lattice structure already close to that of the  $L1_0$ -phase. The ordering process for  $L1_0$ -FePt films therefore involves swapping atoms within the existing lattice into alternating Fe and Pt layers, whereas the process for  $L1_0$ -MnAl requires both rearranging atoms to form the lattice and positioning them in alternating Mn and Al layers. The latter is a more thermodynamically complicated process, and may present challenges to applying techniques for ordering  $L1_0$ -FePt thin films directly to  $L1_0$ -MnAl thin films.

## 2.4. Magnetic Tunnel Junction (MTJs) and Tunneling Magnetoresistance (TMR)

The magnetic tunnel junction (MTJ) is a structure consisting of two magnetic layers, one magnetically fixed and the other magnetically free, separated by a thin, insulating, nonmagnetic tunnel barrier. A simplified schematic is shown in FIG. 2-3, adapted from reference [8]. Basic operation of an MTJ involves passing a current across the junction. Electrons with spins aligned with the magnetization direction of the electrode they are passing through are less likely to be scattered by the lattice than those with spins misaligned, as illustrated in FIG. 2-4, which was adapted from reference [9]. This phenomenon can also be understood through the Two Current Model, which treats the collection of electrons with aligned spins as one current, and the electrons with misaligned spins as a second current. In this model, the aligned current experiences low effective resistance across the material, while the misaligned current experiences high effective resistance. The net spin of the current at the electrode/insulator interface (after it has traveled through the first magnetized electrode) is therefore aligned with the electrode magnetization direction. The electrode therefore acts as a spin filter. The effectiveness of the spin filter, known as the polarization factor, is material dependent.

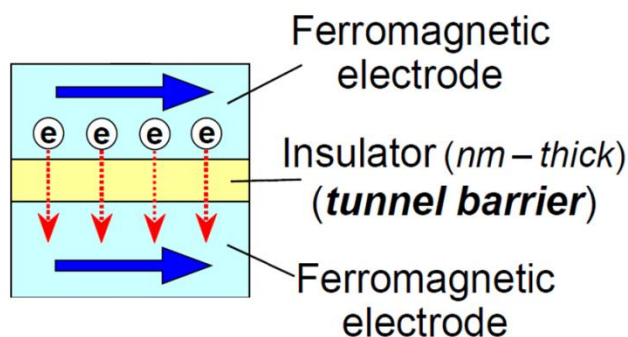


Figure 2-3 Schematic of simple MTJ structure with in-plane electrodes magnetized in parallel.

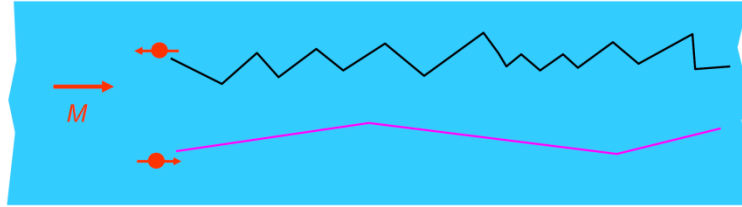


Figure 2-4 Electrons with spins aligned with the magnetized material pass through relatively unhindered, while electrons with spins misaligned encounter significant scattering.

With a thin enough barrier layer, the electrons are able to pass through due to quantum tunneling. Quantum mechanics describes the electron wavefunction during tunneling as an evanescent wave, with an exponentially decaying amplitude. In other words, the effective resistance of the tunnel barrier increases exponentially with barrier thickness. Having a sub-nanometer barrier layer is therefore paramount to reducing operating current and power consumption of MTJ-based devices.

In order for an electron to tunnel successfully across the barrier, there must be an available spin state in the second electrode that matches the spin of the electron. This is known as spin-dependent tunneling. When the two electrodes are magnetized in parallel, the majority spins have corresponding majority spin states available when tunneling to the second electrode, as depicted on the left in FIG. 2-5 [10]. On the other hand, when the two electrodes are magnetized in antiparallel, the majority spins from the first electrode must enter the minority state of the second electrode, as illustrated on the right in FIG. 2-5 [10]. Again using the Two Current Model, shown in FIG. 2-6 [10], an MTJ with parallel magnetized electrodes effectively has low resistance, and an MTJ with antiparallel magnetized electrodes effectively has high resistance. This effect is known as tunneling magnetoresistance (TMR). The magnetic state stored in the free layer can therefore be sensed completely using electrical means, acting as a read operation.

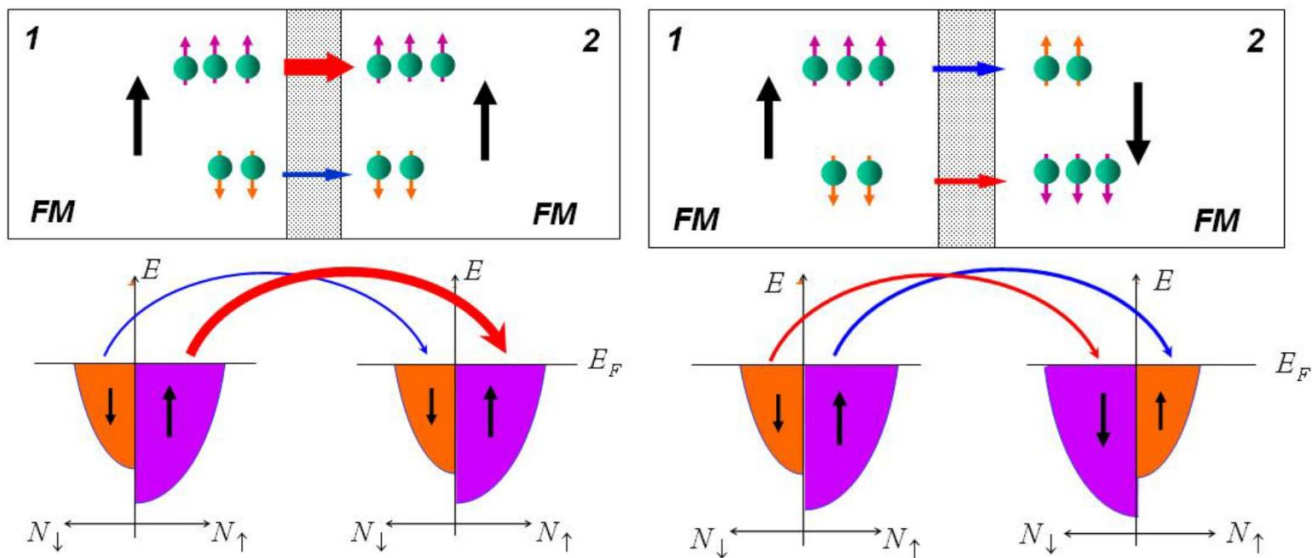


Figure 2-5 Spin-dependent tunneling of electrons from one ferromagnetic electrode (FM) to another across a tunnel barrier (gray) for parallel (left) and antiparallel (right) magnetization configurations. Density of states for each scenario are shown on the bottom.

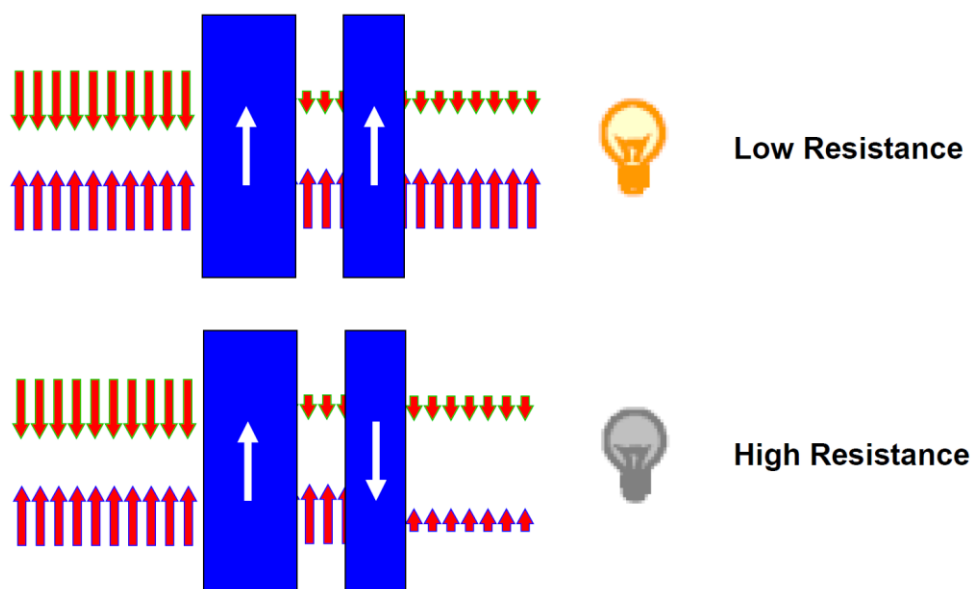


Figure 2-6 Two Current Model of TMR.

## 2.5. Spin-Transfer-Torque (STT) and Critical Switching Current

Newton's Third Law of Motion states that "for every action, there is an equal and opposite reaction". In the world of quantum mechanics, this can be translated to conservation of momentum. Since a magnetized material can scatter and flip electron spins, it therefore follows that electron spins can impart their momentum onto magnetized materials. Indeed, with a sufficient number of electrons, the magnetization direction of a ferromagnetic material can be switched. This phenomenon is known as spin-transfer-torque (STT), and enables a fully electrical method of storing a magnetic state, acting as a write operation. For a scaled MTJ, the ferromagnetic electrodes are small enough that they consist of a single magnetic domain, or macrospin, and their behavior is well characterized by the phenomenological Landau-Lifshitz-Gilbert (LLG) equation with added Slonczewski spin-torque term [11]:

$$\frac{\partial \hat{m}}{\partial t} = -\gamma \hat{m} \times \vec{H}_{\text{eff}} + \alpha \hat{m} \times \frac{\partial \hat{m}}{\partial t} + \frac{\hbar}{2e} \frac{\gamma \eta}{M_s t_F} J \hat{m} \times (\hat{m} \times \hat{m}_R)$$

Equation 2-1

where  $\hat{m}$  is the unit vector denoting the magnetization orientation of the free layer,  $\gamma$  is the gyromagnetic ratio,  $\vec{H}_{\text{eff}} = \vec{H}_a + \vec{H}_k + \vec{H}_D$  is the sum effective field of applied, crystalline anisotropy, and demagnetization fields,  $\alpha$  is the Gilbert damping parameter,  $\hbar$  is the reduced Planck's constant,  $e$  is the elementary charge,  $\eta$  is the spin-transfer efficiency factor,  $M_s$  is the saturation magnetization of the free layer,  $t_F$  is the thickness of the free layer, and  $\hat{m}_R$  denotes the magnetization orientation of the fixed reference layer.

The first term describes the Larmor precession experienced by a macrospin in the presence of an external field, indicated by the green circle in FIG. 2-7. The second term corresponds to the Gilbert damping behavior attributed to magnon-phonon interactions due to the lattice, shown as the blue arrow in FIG. 2-7. The final term is the Slonczewski STT term, indicated by the red arrow in FIG. 2-7, which either counteracts or assists the damping term, depending on the magnitude of the injected current  $J$ .

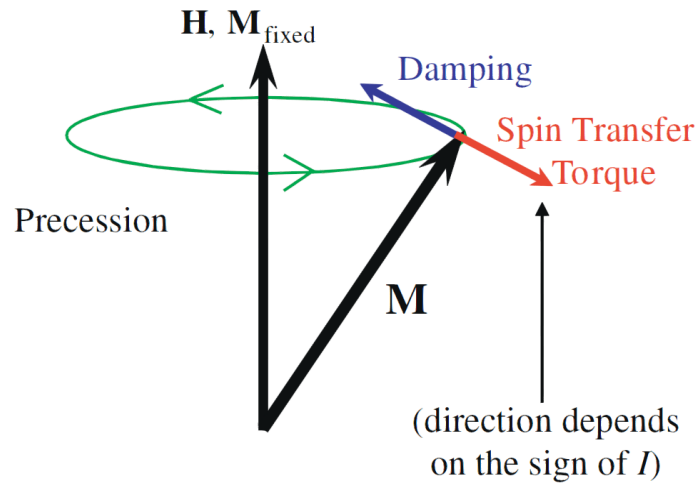


Figure 2-7 Magnetization dynamics of a macrospin  $\mathbf{M}$  in the presence of an external field  $\mathbf{H}$ .

To better understand the role of each parameter in the magnetization switching process, it is helpful to consider the scenario where the critical current density  $J_C$  is just sufficient to counteract the damping term, such that the last two terms of EQ. 2-1 cancel each other out, and the macrospin precesses indefinitely. At this instant, the magnetization is described simply by:

$$\frac{\partial \hat{m}}{\partial t} = -\gamma \hat{m} \times \vec{H}_{\text{eff}}$$

Equation 2-2

Since the last two terms cancel out, their relationship is given by:

$$\alpha \hat{m} \times \frac{\partial \hat{m}}{\partial t} + \frac{\hbar}{2e} \frac{\gamma \eta}{M_s t_F} J_c \hat{m} \times (\hat{m} \times \hat{m}_R) = 0$$

Equation 2-3

Substituting in EQ. 2-2 gives:

$$\alpha \hat{m} \times (-\gamma \hat{m} \times \vec{H}_{\text{eff}}) + \frac{\hbar}{2e} \frac{\gamma \eta}{M_s t_F} J_c \hat{m} \times (\hat{m} \times \hat{m}_R) = 0$$

Equation 2-4

If there is no externally applied magnetic field or significant pinning field (use of a pinning field is explored in Section 7.3), the effective field is parallel to the reference layer magnetization direction, giving:

$$\vec{H}_{\text{eff}} = (H_k + H_D) \hat{m}_R$$

Equation 2-5

Substituting EQ. 2-5 into EQ. 2-4 and moving the first term to the right hand side produces:

$$\alpha \gamma (H_k + H_D) \hat{m} \times (\hat{m} \times \hat{m}_R) = \frac{\hbar}{2e} \frac{\gamma \eta}{M_s t_F} J_c \hat{m} \times (\hat{m} \times \hat{m}_R)$$

Equation 2-6

As expected, the vector components are identical. Solving the scalar components for  $J_c$  results in:

$$J_c = \frac{2e\alpha}{\hbar\eta} M_s t_F (H_k + H_D)$$

Equation 2-7

The magnitude of the demagnetization field  $H_D$  depends on the easy axis direction of the electrodes. For in-plane electrodes,  $H_D = 2\pi M_s$ . For out-of-plane electrodes,  $H_D = 0$ . From this, one can see that in-plane MTJs have a higher critical switching current density, whereas perpendicular MTJs (pMTJs) exhibit a lower critical switching current density, and therefore lower operating power. One way to conceptualize this difference is to imagine the free layer macrospin precessing just before switching. Since the thickness of a thin film is its shortest dimension, the demagnetization field always pushes the macrospin to lie in the plane of the film. A precessing in-plane macrospin must overcome the demagnetization field in order to switch to the other direction. On the other hand, a precessing out-of-plane macrospin is assisted by the demagnetization field in switching to the other direction. This intrinsic advantage of out-of-plane electrodes reveals the inherent scalability of pMTJs, and has been verified in the literature [12]. For pMTJs, one therefore eliminates  $H_D$  and substitutes the equivalent expression for anisotropy field

$$H_k = \frac{2K_u}{M_s}$$

Equation 2-8

into EQ. 2-7, which gives:

$$J_c = \frac{2e}{\hbar} \frac{2\alpha}{\eta} K_u t_F$$

Equation 2-9

Lastly, multiply by the area of the MTJ to arrive at the critical switching current

$$I_c = \frac{2e}{\hbar} \frac{2\alpha}{\eta} K_u V_F$$

Equation 2-10

From this final expression, one can see that the Gilbert damping parameter  $\alpha$  directly impacts the critical switching current. Since this is a parameter intrinsic to the material system used, selected materials should have low damping. The spin-transfer efficiency factor  $\eta$  is dependent on the polarization capabilities of each electrode, as well as the filtering potential of the tunnel barrier. Well-ordered electrodes exhibiting high degree of epitaxy with a crystalline tunnel barrier such as MgO are advantageous for maximizing  $\eta$ . The last two factors,  $K_u V_F$ , are the same ones that feature in the expression for thermal stability, discussed in Section 1.2. Since thermal stability itself presents a tradeoff between scalability and retention, there are therefore clear design tradeoffs among scale, retention time, and power. For example, designing an MTJ structure with high  $K_u$  and high  $V_F$  results in a large device footprint, high retention, and high power consumption. On the other hand, an MTJ structure with low  $K_u$  and low  $V_F$  produces a small device footprint, low retention, and low power consumption. It is due to these many degrees of

design freedom that MTJs can be tailored to each application depending on performance specifications, as discussed in Section 1.3.

## 2.6. Summary

In this chapter, the theoretical foundations useful for understanding the rest of the dissertation were laid. First, crystallographic aspects of  $L1_0$ -ordering were introduced, and the challenges and techniques to achieving perpendicular magnetic anisotropy in  $L1_0$ -ordered materials were discussed (Section 2.2). A brief comparison of  $L1_0$ -FePt and  $L1_0$ -MnAl thin films was given, highlighting important differences in their respective ordering processes (2.3). Next, magnetic tunnel junctions were described and the phenomenon of tunneling magnetoresistance was discussed, illustrating the ability to perform read operations using purely electrical methods (2.4). Finally, spin-transfer-torque was presented as an electrical write operation, the expression for critical switching current was derived, the parameters impacting power consumption were highlighted, and possible design tradeoffs were weighed (2.5).

## 2.7. References

- [1] D. E. Laughlin, K. Srinivasan, M. Tanase, and L. Wang, “Crystallographic aspects of  $L1_0$  magnetic materials,” *Scr. Mater.*, vol. 53, no. 4, pp. 383–388, Aug. 2005.
- [2] K. Anand, J. J. Pulikkotil, and S. Auluck, “Study of ferromagnetic instability in  $\gamma$ -MnAl, using first-principles,” *J. Alloys Compd.*, vol. 601, pp. 234–237, Jul. 2014.
- [3] A. J. J. Koch, P. Hokkeling, M. G. v. d. Steeg, and K. J. de Vos, “New Material for Permanent Magnets on a Base of Mn and Al,” *J. Appl. Phys.*, vol. 31, no. 5, p. S75, 1960.
- [4] S. D. Granz, “Granular  $L1_0$  FePt:X (001) Thin Films for Heat Assisted Magnetic Recording,” Ph.D. Dissertation, Carnegie Mellon University, Pittsburgh, PA, 2012.
- [5] Y. F. Ding, J. S. Chen, E. Liu, C. J. Sun, and G. M. Chow, “Effect of lattice mismatch on chemical ordering of epitaxial  $L1_0$  FePt films,” *J. Appl. Phys.*, vol. 97, no. 10, p. 10H303, 2005.
- [6] C. S. Kim, “Feasibility of a Multi-bit Cell Perpendicular Magnetic Tunnel Junction Device,” Ph.D. Dissertation, Carnegie Mellon University, Pittsburgh, PA, 2013.
- [7] S. D. Granz and M. H. Kryder, “Intergranular Exchange Coupling in FePt:X:FePt (X=B, C, SiO<sub>x</sub>, Cr and TaO<sub>x</sub>) Thin Films for Heat Assisted Magnetic Recording,” *IEEE Trans. Magn.*, vol. 48, no. 11, pp. 2746–2748, Nov. 2012.
- [8] S. Yuasa, “Magnetoresistance and spin-transfer torque in magnetic tunnel junctions,” presented at the IEEE Distinguished Lecturer Series, 2012.
- [9] J.-G. Zhu, “Giant Magneto-Resistance,” presented at the 18-716 Course Lecture, 2012.
- [10] J.-G. Zhu, “Tunneling Magneto-Resistance (TMR),” presented at the 18-716 Course Lecture, 2012.
- [11] J. C. Slonczewski, “Current-driven excitation of magnetic multilayers,” *J. Magn. Magn. Mater.*, vol. 159, p. L1, 1996.
- [12] T. Kishi, H. Yoda, T. Kai, T. Nagase, E. Kitagawa, M. Yoshikawa, K. Nishiyama, T. Daibou, M. Nagamine, M. Amano, and others, “Lower-current and fast switching of a perpendicular TMR for high speed and high density spin-transfer-torque MRAM,” in *Electron Devices Meeting, 2008. IEDM 2008. IEEE International*, 2008, pp. 1–4.

# Chapter 3

## Experimental Methods and Equipment

### 3.1. Introduction

In this chapter, the fabrication and characterization techniques used in the rest of the dissertation are discussed. A brief overview of operating theory is presented, followed by a synopsis of the equipment and capabilities used in thin film deposition (Section 3.2), annealing (3.3), magnetic characterization (3.4), and microstructural and physical characterization (3.5).

### 3.2. Thin Film Deposition

The thin films studied throughout this dissertation were all deposited via sputtering, a technique whereby particles from the material of interest (the target) are ejected by bombardment from plasma ions (typically Ar). The ejected particles tend to deposit on all surfaces in the chamber, including the substrate, which is positioned facing the target on the opposite side of the chamber. Depending on the conductivity of the target, one of two sputtering modes are used: direct current (DC) or radio frequency (RF). If the target is conducting, a simple DC circuit can be set up, with the target as the cathode and the substrate assembly as the anode. DC sputter deposition rates are typically high and well controlled. An optional magnetron setup can be installed to establish a local magnetic field ring near the target. This magnetic field traps plasma ions and further increases the deposition rate. If the target is insulating, however, a simple DC circuit cannot be used. Since the target is insulating, positive plasma ions will accumulate on the

face of the insulating target over time, eventually eliminating the voltage differential across the plasma and thereby shutting it off. Instead, an RF setup must be employed, with the role of cathode and anode periodically cycled between the target and substrate. This allows accumulated positive ions on the target to be sputtered off, sustaining the plasma. However, due to the back-and-forth nature of RF sputtering, deposition rates are much lower than those of DC sputtering, and the need to monitor and adjust a matching RF network introduces complications that may increase variability.

### 3.2.1 Leybold-Heraeus Z-400 Sputtering System #2

The Leybold-Heraeus Z-400 Sputtering System #2, shown in FIG. 3-1, is a sputtering system that houses four 75 mm targets. Each target can be independently set up for DC or RF sputtering, with targets and shutter controlled manually. The system can accommodate wafers up to 2" in diameter. The low-vacuum pump serves as both the roughing pump to the deposition chamber and as the backing pump to the high-vacuum turbo pump, regulated by a set of valves. The chamber can reach base pressures of below  $3 \times 10^{-7}$  Torr if pumped overnight. The installed power supplies deliver a maximum of 500 W DC power or 600 W RF power. The substrate assembly incorporates a heater, with a maximum dial temperature of 850 °C. Calibration data indicates this corresponds to a substrate surface temperature of 570 °C. Substrates take 30 minutes to reach the desired temperature and 3 hours to cool to down to room temperature.



Figure 3-1 Leybold-Heraeus Z-400 Sputtering System #2.

### 3.2.2 Custom 5-Target Sputtering System #2

The Custom 5-Target Sputtering System #2, shown in FIG. 3-2, is a sputtering system that houses five 5" or 75 mm targets. Each target can be independently set up for DC or RF sputtering, with substrate position and shutter controlled through a programmable panel. The system can accommodate wafers up to 1" in diameter. The low-vacuum pump serves as the roughing pump to the deposition chamber, with a cryo pump acting as the high-vacuum pump. The chamber can reach base pressures of below  $3 \times 10^{-7}$  Torr. The installed power supplies deliver a maximum of 500 W DC power or 600 W RF power. The substrate assembly incorporates a heater, with a maximum dial temperature of 800 °C. Substrates take 30 minutes to reach the desired temperature and 3 hours to cool to down to room temperature.



Figure 3-2 Custom 5-Target Sputtering System #2.

### **3.3. Annealing**

Apart from increasing *in situ* temperature during deposition, thermal energy can be imparted to the films post-deposition via a number of annealing methods. For the samples in this dissertation, the purpose of annealing is to achieve the proper texture or ordering in the films. The thermal energy allows atoms within the film to diffuse through the material in three dimensions. With the proper film composition, temperature, and template, desired textures and ordering can be achieved.

#### **3.3.1 Micro Magnetics SpinTherm-1000 Magnetic Annealing System**

The Micro Magnetics SpinTherm-1000 Magnetic Annealing System is a thermal annealing system with a fixed field of 4 kOe applied laterally across the chamber. Two types of holders allow samples to be mounted vertically or horizontally, resulting in the field being applied either perpendicular or parallel to the film plane, respectively. A scroll pump acts as the low-vacuum pump, and a turbo pump serves as the high-vacuum pump. The system can reach base pressures of below  $2 \times 10^{-7}$  Torr. The maximum temperature achieved by the system is 450 °C. The system typically takes 30-45 minutes to reach the target temperature, and is allowed to cool overnight.

#### **3.3.2 AG Associates Heat Pulse Rapid Thermal Annealing System**

The AG Associates Heat Pulse Rapid Thermal (RTA) Annealing System, shown in FIG. 3-3 is an RTA system that uses a high intensity lamp to transfer thermal energy to the sample surface. Samples sit on a carrier Si wafer inside the chamber, with the lamp assembly at the top of the chamber projecting downwards. The system is not vacuum pumped. Instead, a choice of

gas is flowed through the chamber. Common gases are Oxygen, Nitrogen, Argon, and Forming Gas (95% Ar, 5% H). Recipes are programmable and automated through a console, with gas flow rate, annealing temperature, annealing time, and temperature ramp rate as frequently adjusted parameters. The maximum temperature of the system is 850 °C.



Figure 3-3 AG Associates Heat Pulse Rapid Thermal Annealing System.

### 3.3.3 Tube Annealing Furnace

The Tube Annealing Furnace, shown in FIG. 3-4, is a conventional tube furnace annealer. Samples are loaded onto a quartz boat, then positioned inside the 2”-diameter quartz tube. The system is not vacuum pumped. Instead, a choice of gas is flowed through the chamber. Common gases are Oxygen, Nitrogen, Argon, and Forming Gas (95% Ar, 5% H). The maximum temperature of the system is 950 °C. The system typically takes 2 hours to reach the set temperature, and is allowed to cool overnight.



Figure 3-4 Tube Annealing Furnace.

### **3.4. Magnetic Characterization**

Magnetic properties were extracted from magnetic hysteresis loops as measured by a magnetometer. For both the vibrating sample magnetometer (VSM) and alternating gradient force magnetometer (AGFM) discussed below, the sample is placed inside an applied magnetic field. The resulting magnetic moment is sensed by a pickup coil positioned around the sample, and the contribution of the sample to the moment is calculated. Depending on the holder, samples can be oriented such that the applied field, and therefore measured moment, are perpendicular to or along the film plane. Resulting measurements are referred to as out-of-plane and in-plane magnetic hysteresis loops, respectively. While the AGFM used in this dissertation produces measurements with lower noise and at a higher rate, the VSM allows for high- and low-temperature measurements, and has a much higher maximum applied field.

#### **3.4.1 Quantum Design Vibrating Sample Magnetometer (VSM)**

The Quantum Design Vibrating Sample Magnetometer (VSM) is an option installed on the Quantum Design Physical Property Measurement System (PPMS). The sample is mounted at the end of a long rod that is lowered into the measurement chamber. A magnetic field is applied by the superconducting magnet, and the VSM motor oscillates the sample rod vertically. The movement of the sample through the applied field produces a change in magnetic flux which, according to Faraday's law of electromagnetic induction, induces an electric current in the pickup coils. This reading is amplified and compared to a reference signal provided by the oscillator. A lock-in amplifier amplifies the reading and multiplies it by the reference signal. The output signal is then passed through a filter to remove AC components. The resulting output is a DC signal proportional to the measured moment of the sample. Sweeping the magnetic field

through positive and negative saturating fields produces the desired magnetic hysteresis loop. The Quantum Design VSM is capable of ultra low temperature measurements as well as high temperature measurements with the appropriate heater assembly installed. Maximum applied field is 90 kOe.

### **3.4.2 Princeton Measurement Corp. Micromag 2900 Alternating Gradient Force Magnetometer (AGFM)**

The Princeton Measurement Corp. Micromag 2900 Alternating Gradient Field Magnetometer (AGFM) applies an alternating gradient field to the sample, which is secured to the end of a piezoelectric sample holder cantilever. The alternating gradient field exerts an oscillatory force on the sample, which produces bending on the cantilever proportional to the magnetic moment of the sample. This bending force is sensed and the moment corresponding to the measured sample is calculated. The Princeton Measurement Corp. AGFM has an advanced electromagnet power supply that enables a high sweep rate. However, the size of the electromagnet limits the maximum applied field to 13 kOe.

## **3.5. Microstructural and Physical Characterization**

Aside from magnetic properties, the texture, ordering, and morphology of materials are very important in the study of thin films and particularly so for the  $L1_0$ -ordered films discussed herein. For films above approximately 20 nm in thickness, X-ray diffraction (XRD) is a reliable method of investigating the texture and ordering. Surface contours and longer-range film morphology can be characterized using atomic force microscopy (AFM). For atom-level

resolution and investigation of ultra thin films (under 10 nm), transmission electron microscopy (TEM) is necessary.

### 3.5.1 Philips X'Pert Pro X-Ray Diffractometer (XRD)

The Philips X'Pert Pro X-Ray Diffractometer (XRD) uses diffraction to determine the crystalline structure of a material. The diffraction patterns obtained by scanning a sample across a range of angles can be used to infer the crystalline phase, texture,  $d$ -spacing, and lattice constants of the material. Constructive interference occurs under the Bragg condition

$$2d_{hkl} \sin \theta = \lambda$$

Equation 3-1

where  $d_{hkl}$  is the spacing between diffracting planes,  $\theta$  is the incident angle of the X-ray beam, and  $\lambda$  is the wavelength of the X-ray source. The constructive interference is seen as a peak in the diffraction pattern, with the incident angle corresponding to a particular lattice spacing. Comparing peaks to known diffraction patterns of the bulk material can help identify the presence of crystalline phases and textures. The intensity and width of the peak can be used to infer the prevalence and uniformity of the particular lattice spacing within the sample. The Philips X'Pert Pro XRD uses a Cu source that produces  $\text{CuK}_\alpha$  radiation with a wavelength of  $\lambda = 1.5405 \text{ \AA}$ . The X-ray source is operated at 40 keV and 40 mA, with scan angles typically between  $15^\circ$  and  $65^\circ$ .

### **3.5.2 NT-MDT Solver Next Atomic Force Microscope (AFM)**

The NT-MDT Solver Next Atomic Force Microscope (AFM) uses a cantilever probe to profile the surface of the sample. A sharp probe, also called the tip, is mounted on a cantilever. Depending on the measurement mode, the tip is brought near or onto the surface of the sample, where various forces produce a deflection in the cantilever as described by Hooke's Law. The deflection is detected by a laser directed at the top of the cantilever. AFM measurements performed in this dissertation were done using tapping mode, which relies on van der Waals, dipole-dipole, and electrostatic forces to deflect the cantilever probe. In this mode, the cantilever is oscillated with the probe very near, but not touching, the sample surface. The oscillation is perturbed by the various forces, and the resulting deflection can be used to profile the sample surface. The NT-MDT Solver Next AFM allows automated focusing and positioning. Depending on the probe tip used, image resolution can be on the nanometer scale. The tips used in measurements were Si tips coated with diamond-like carbon and had a resonant frequency between 200 and 400 kHz.

### **3.5.3 NT-MDT NTegra Prima AFM**

The NT-MDT NTegra Prima AFM operates using the same principles as the NT-MDT Solver Next AFM, but can also accommodate a high-resolution stage. Measurements were done using tapping mode, relying on van der Waals, dipole-dipole, and electrostatic forces to deflect the cantilever probe. Focusing and positioning can be automated, though manual operation is often more efficient. Depending on the probe tip used, image resolution can be on the nanometer scale. The tips used in measurements were Si tips coated with diamond-like carbon and had a resonant frequency between 200 and 400 kHz.

### **3.5.4 JEOL 2000EX Transmission Electron Microscope (TEM)**

The JEOL 2000EX Transmission Electron Microscope (TEM) passes a high-energy electron beam through an ultra-thin sample. The electron beam is focused through an objective lens onto the thinned, electron-transparent sample. The electrons are diffracted or transmitted, depending on the materials and crystal planes in the beam area, which are then detected by a CCD camera. Diffracted electrons produce a diffraction pattern on the back focal plane of the objective lens, and transmitted electrons produce an image on the image plane. An aperture on the back focal plane of the objective lens allows selection of transmitted or diffracted beams, resulting in bright field or dark field images, respectively. Since electrons have a very small de Broglie wavelength, TEM is useful for imaging features smaller than the wavelength of visible light. With good specimen preparation and TEM operating technique, lattice fringes and atomic scale features can be imaged. TEM specimens were prepared by hand polishing, dimpling, and ion milling.

### **3.5.5 Philips Tecnai F20 Field Emission TEM**

For higher resolution imaging and characterization of atomic sites, the Philips Tecnai F20 Field Emission TEM was used. The Philips Tecnai F20 Field Emission TEM uses the same operating principles as the JEOL 2000EX. TEM specimens were prepared by hand polishing, dimpling, and ion milling.

### **3.6. Summary**

In this chapter, the fabrication and characterization techniques used throughout the rest of this dissertation were described. Equipment capabilities and basic underlying theory were discussed. In the next chapter, the development of MnAl thin films with high perpendicular magnetic anisotropy (PMA) on Si substrates for spin-transfer-torque magnetoresistive random access memory (STT-MRAM) applications will be discussed.

# Chapter 4

## ***L1<sub>0</sub>*-Ordered MnAl Thin Films on MgO Underlayers**

### **4.1. Introduction**

While *L1<sub>0</sub>*-ordered magnetic materials generally have high PMA [1], the need for low damping and moderate  $M_s$  to reduce critical switching current density imposes constraints on the pool of viable materials for STT-MRAM applications. The well-studied FePt, for example, can be reliably deposited as a thin film with  $K_u > 5 \times 10^7$  erg/cm<sup>3</sup>, but demonstrates high Gilbert damping parameter of  $\alpha = 0.2$  and high  $M_s > 1000$  emu/cm<sup>3</sup> [2]–[4]. On the other hand, *L1<sub>0</sub>*-ordered  $\tau$ -phase MnAl thin films have been shown to exhibit high perpendicular magnetic anisotropy ( $K_u > 10^7$  ergs/cm<sup>3</sup>), moderate saturation magnetization ( $M_s < 600$  emu/cm<sup>3</sup>), and low Gilbert damping parameter ( $\alpha = 0.006$ ) [5]–[7].  $\tau$ -MnAl is also rare earth- and precious metal-free, providing economic advantages over other candidate materials such as FePt. As a result, *L1<sub>0</sub>*-ordered  $\tau$ -phase MnAl has rightfully attracted much attention over the years [5]–[15]. However, achieving the necessary *L1<sub>0</sub>*-ordering for perpendicular anisotropy in MnAl thin films has proven challenging and highly sensitive to deposition conditions and underlayers used [1]. Nevertheless, the DSSC had done significant prior work on *L1<sub>0</sub>*-FePt [2], [3], and given the structural similarities between *L1<sub>0</sub>*-FePt and *L1<sub>0</sub>*-MnAl, many of the developed processes and recipes were potentially applicable to the fabrication of *L1<sub>0</sub>*-MnAl films.

Bulk  $\tau$ -MnAl has the *L1<sub>0</sub>*-ordered CuAu-type structure with alternating Mn and Al monolayers in the *c*-axis direction and is formed martensitically as a metastable phase [16], [17];

however, in thin films  $\tau$ -MnAl is stable at ambient temperature. The formation of  $\tau$ -MnAl in thin films is highly sensitive to deposition conditions and composition, with Hosoda et al. reporting an optimal target composition of  $\text{Mn}_{48}\text{Al}_{52}$  [5]. Nevertheless, while there has been considerable work developing  $\tau$ -MnAl films on substrates such as GaAs (001) [6], [8]–[11], MgO (001) [5], [7], [12], and glass [13], [14], there have previously been no reports of high-PMA  $\tau$ -MnAl films on Si substrates [1]. The use of Si substrates is critical for CMOS-compatibility, and development of high-PMA films on Si substrates is a prerequisite for practical application in STT-MRAM devices. MgO (002) is well known as a useful underlayer for promoting  $L1_0$ -ordering in subsequent FePt films [2]. Given the existing body of knowledge on using MgO underlayers to grow well-ordered  $L1_0$ -FePt films, MgO was selected as the underlayer of choice for initial work in developing  $L1_0$ -MnAl thin films.

In this chapter,  $L1_0$ -ordered  $\tau$ -phase MnAl thin films with high PMA on Si substrates are fabricated and characterized using insulating MgO underlayers. It should be noted that much of the work discussed in this chapter was previously published in reference [18].

## 4.2. Experimental Details

The substrates used in this study were natively oxidized 1” (100) Si wafers. All films were deposited in the Leybold-Heraeus Z-400 Sputtering System #2 at base pressures below  $3 \times 10^{-7}$  Torr. Film stacks followed the structure Si substrate/MgO (20 nm)/MnAl (10-50 nm)/Ta (5 nm). First, a 20 nm MgO seed layer was RF sputtered (0.015 nm/s film growth rate, 10 mTorr Ar gas pressure) onto a Si substrate at room temperature. The substrate was then heated *in situ* to various temperatures (23-570 °C), which helped enhance the MgO (001) texture. Next, a 10-50 nm MnAl film was DC magnetron sputtered from a vacuum hot-pressed  $\text{Mn}_{48}\text{Al}_{52}$  target onto the

MgO at a deposition rate of 0.31-0.78 nm/s with an Ar gas pressure of 4 mTorr. The substrate was subsequently allowed to cool to room temperature, and a 5 nm Ta capping layer was DC magnetron sputtered at a deposition rate of 0.083 nm/s using Ar gas pressure of 4mTorr. Lastly, the sample was annealed in the Micro Magnetics SpinTherm-1000 magnetic thermal annealing system with a base pressure under  $5 \times 10^{-7}$  Torr and a fixed 4 kOe field perpendicular to the film plane at various temperatures (250-350 °C). Calibrations for *in situ* substrate temperatures were performed using a Type K chromel–alumel thermocouple. Texture, microstructure, and magnetic properties of the film stacks were investigated using XRD, TEM, AGFM, and PPMS. Thickness-dependent order parameters  $S$  were calculated for the MnAl films from the integrated peak intensity ratios  $I_{001}/I_{002}$  extracted from out-of-plane  $\theta/2\theta$  XRD patterns [19]–[21]. Magnetic anisotropy constants were determined according to  $K_u = H_k M_s / 2$ , where  $H_k = H_s + 4\pi M_s$  is the anisotropy field,  $H_s$  is the hard-axis (in-plane) saturation field, and  $M_s$  is the saturation magnetization.

### 4.3. Results and Discussion

The effects of *in situ* sputtering temperature ( $T_s$ ) on formation of  $\tau$ -MnAl can be seen from the  $\theta/2\theta$  XRD patterns shown in FIG. 4-1. The 30 nm MnAl films were sputtered using DC power of 40 W and annealed at  $T_a = 350$  °C. The MnAl (001) and (002) peaks were measured to be at  $24.8^\circ$  and  $50.9^\circ$ , respectively. The peaks at  $33.0^\circ$ ,  $38.2^\circ$ , and  $61.7^\circ$  belong to the Si substrate, due to alignment of samples during the scan. At sputtering temperatures below 350 °C, no significant  $\tau$ -MnAl was observed in films. As  $T_s$  increased above 350 °C,  $\tau$ -MnAl began to form, reaching a maximum order parameter  $S$  of 0.98 at  $T_s = 410$  °C. This high degree of ordering ( $S > 0.94$ , rocking curve FWHM angle  $\sim 5^\circ$ ) was maintained for  $T_s$  up to 530 °C, when rapid degradation of the  $\tau$ -phase began to occur, with  $T_s = 570$  °C resulting in very little  $\tau$ -MnAl. Instead, the nonmagnetic  $\varepsilon$ -phase became dominant. The  $c$ -axis lattice constants were calculated from the out-of-plane  $2\theta \sim 24.8^\circ$   $\tau$ -MnAl (001) peaks as 3.58-3.59 Å for all films with significant  $\tau$ -MnAl. In-plane XRD scans revealed  $a$ -axis lattice constants of 3.92-3.95 Å for  $\tau$ -MnAl and 4.19-4.21 Å for MgO. Unlike previous studies [5], [6], which found smaller  $c$ -axis and larger  $a$ -axis MnAl lattice constants in thin films compared to bulk MnAl, these values are very close to the reported value of  $c = 3.57$  Å and  $a = 3.92$  Å for bulk  $\tau$ -MnAl [16]. The epitaxial growth relationship between MgO and  $\tau$ -MnAl is shown in FIG. 4-2: MgO [100] (001) // MnAl [100] (001).

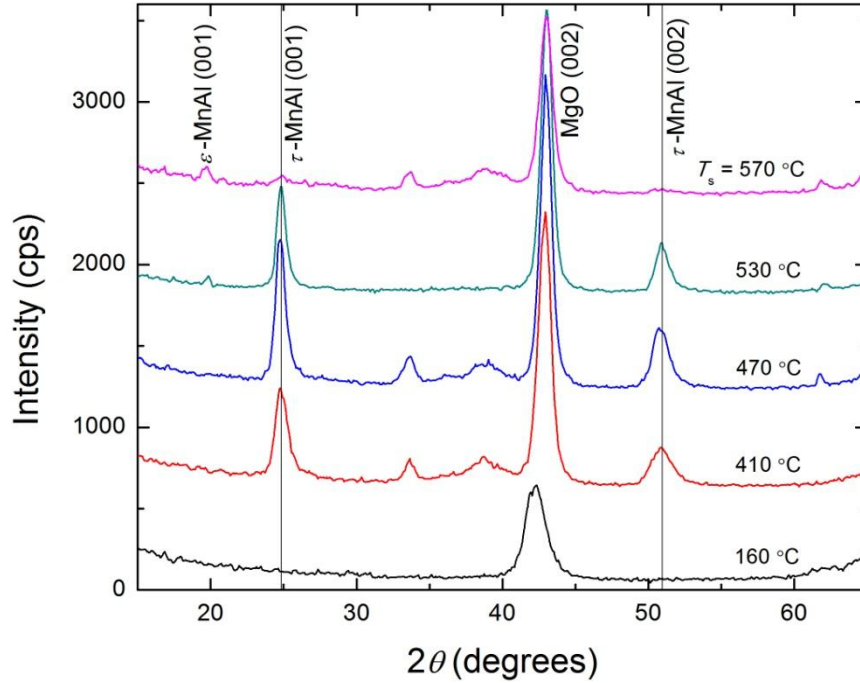


Figure 4-1 Out-of-plane  $\theta/2\theta$  XRD patterns of 30 nm MnAl films deposited at various *in situ* substrate temperatures, 40 W DC power, and  $T_a = 350$  °C.

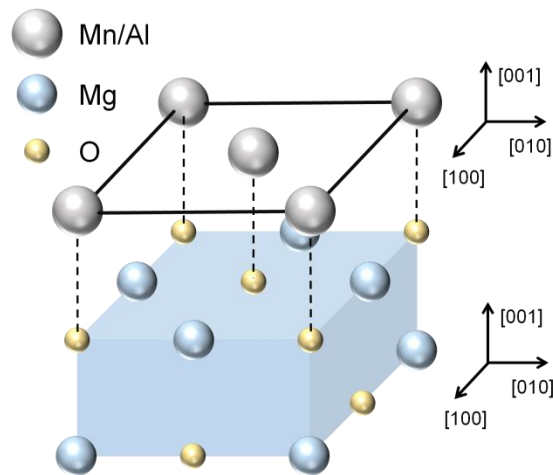


Figure 4-2 Schematic of epitaxial growth relationship at MgO/ $\tau$ -MnAl interface.

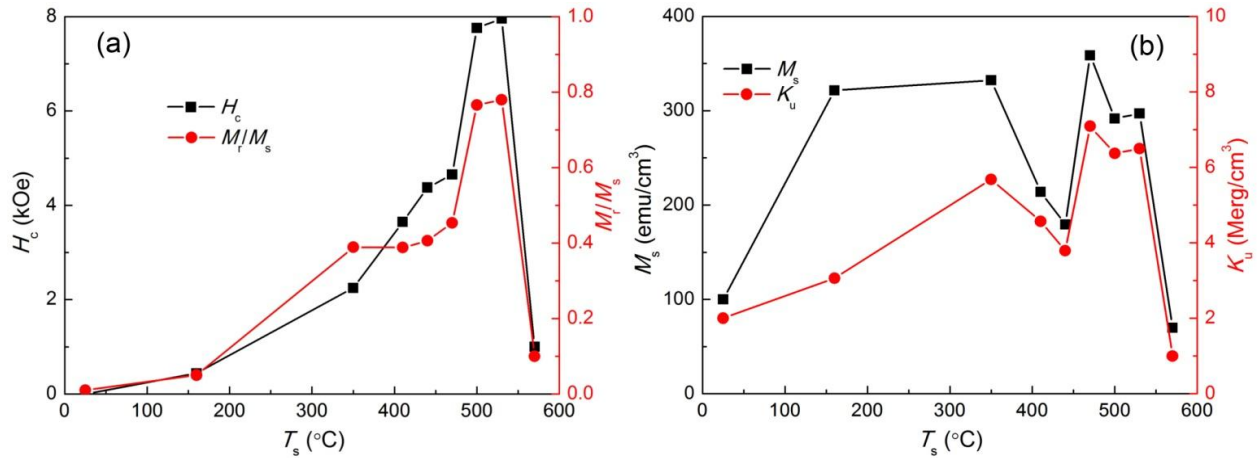


Figure 4-3 Sputtering temperature dependence of (a) out-of-plane coercivity  $H_c$  and squareness  $M_r/M_s$  and (b) saturation magnetization  $M_s$  and anisotropy constant  $K_u$  of 30 nm MnAl films deposited using 40 W DC power and annealed at  $T_a = 350$  °C.

The dependence of coercivity ( $H_c$ ), squareness ( $M_r/M_s$ , where  $M_r$  is the out-of-plane remanent magnetization with no applied field), saturation magnetization ( $M_s$ ), and anisotropy constant ( $K_u$ ) on  $T_s$  were measured and are shown in FIG. 4-3. The 30 nm MnAl films were sputtered using DC power of 40 W and annealed at  $T_a = 350$  °C. From these data,  $T_s = 530$  °C appeared to produce MnAl films with the highest PMA. This substrate temperature was therefore used for further studies.

The thickness dependence of the magnetic properties and microstructure of MnAl films was also examined. From the out-of-plane  $\theta/2\theta$  XRD patterns shown in FIG. 4-4, one can see that films under 10 nm produced poor  $L1_0$ -ordering, and increasing film thickness to 50 nm produced more nonmagnetic  $\varepsilon$ -phase rather than  $\tau$ -phase. The film thickness was consequently selected to be 30 nm.

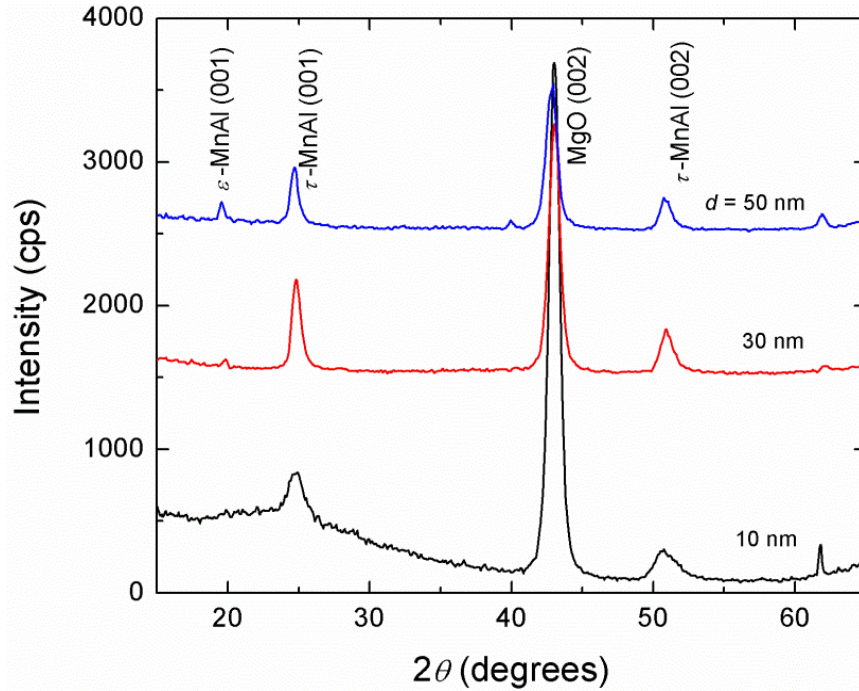


Figure 4-4 Out-of-plane  $\theta/2\theta$  XRD patterns of MnAl films with various thicknesses deposited using 40 W DC power,  $T_s = 530$  °C, and  $T_a = 350$  °C.

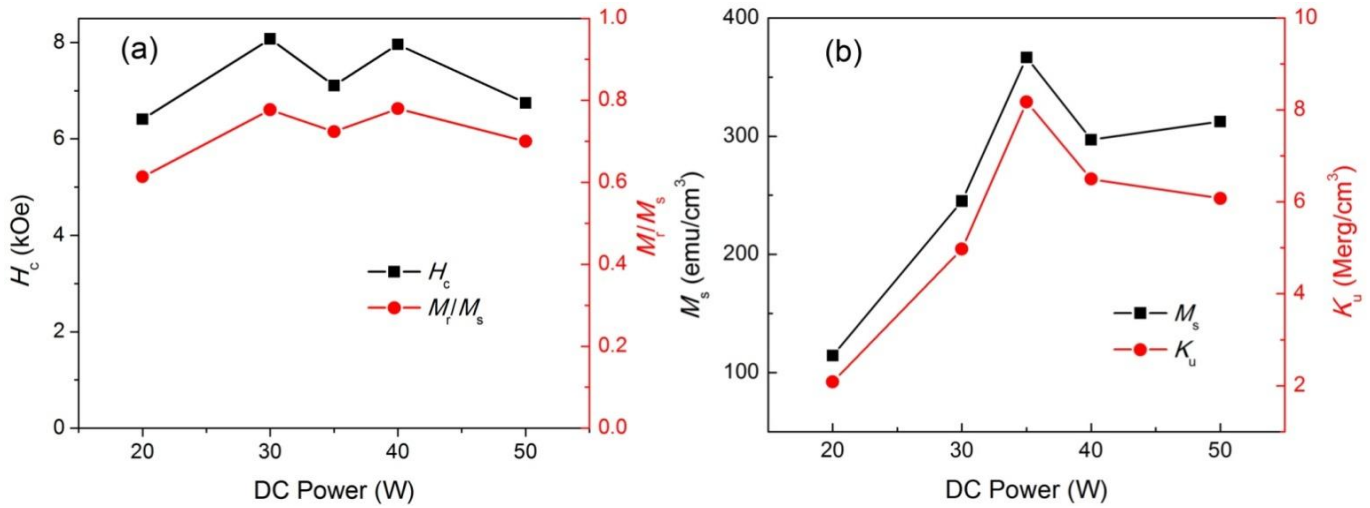


Figure 4-5 DC sputtering power dependence of (a) out-of-plane coercivity  $H_c$  and squareness  $M_r/M_s$  and (b) saturation magnetization  $M_s$  and anisotropy constant  $K_u$  of 30 nm MnAl films deposited at  $T_s = 530$  °C, and  $T_a = 350$  °C.

The effects of DC sputtering power on magnetic properties were studied and are shown in FIG. 4-4. Films produced using DC sputtering power of 30 to 40 W demonstrated the highest perpendicular coercivity and squareness. Additionally, films deposited with DC power less than 30 W contained significant  $\varepsilon$ -phase, suggesting that low sputtering powers do not impart sufficient energy upon the Mn and Al atoms for them to order properly. Ultimately, 40 W, which deposited MnAl film at a rate of 0.63 nm/s, was chosen for further study as it produced MnAl films with high  $H_c$  and moderately high  $M_s$ .

The impact of magnetic annealing temperature ( $T_a$ ) was investigated and the results are plotted in FIG. 4-6. Error bars reflect possible range of values adjusting for the thickness of an interdiffusion layer between MnAl and Ta cap (maximum of 5 nm measured for  $T_a = 350$  °C, shown in TEM image below). Out-of-plane magnetic properties were improved with increasing  $T_a$ , although  $M_s$  decreased as  $T_a$  was increased to 300 °C. Saturation magnetization  $M_s$  was partially recovered at  $T_a = 350$  °C, which was selected as the final annealing temperature.

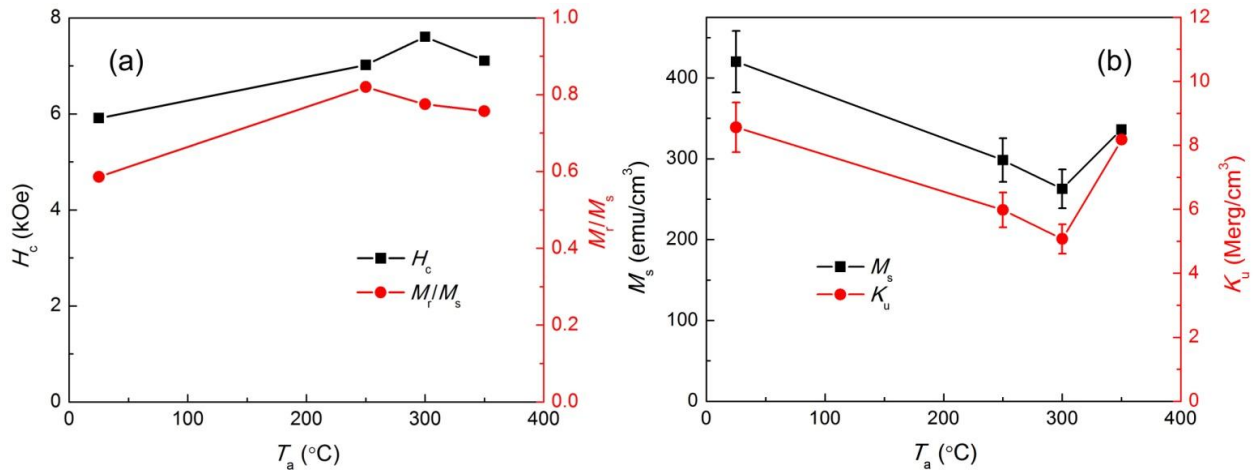


Figure 4-6 Magnetic annealing temperature dependence of (a) out-of-plane coercivity  $H_c$  and squareness  $M_r/M_s$  and (b) saturation magnetization  $M_s$  and anisotropy constant  $K_u$  (error bars indicate possible range of values adjusting for thickness of MnAl/Ta interdiffusion layer). 10 nm MnAl films were deposited using 40 W DC power and  $T_s = 530$  °C.

The final set of deposition conditions was thus determined to be 40 W DC sputtering power (which produced a deposition rate of 0.63 nm/s), 30 nm MnAl film thickness, *in situ* sputtering temperature of  $T_s = 530$  °C, and magnetic annealing temperature of  $T_a = 350$  °C. Using these parameters, a MnAl film was fabricated and characterized. As plotted in FIG. 4-7(a), the film demonstrated high PMA with  $H_c$  of 8 kOe,  $K_u$  of  $6.5 \times 10^6$  erg/cm<sup>3</sup>,  $M_s$  of 300 emu/cm<sup>3</sup>, and out-of-plane squareness  $M_r/M_s$  of 0.8, with a measured film composition of Mn<sub>54.0</sub>Al<sub>46.0</sub> and order parameter of  $S = 0.94$ . The TEM cross-sectional image in FIG. 4-7(b) shows significant clumping of MnAl above the MgO (001) seed layer, suggesting the need for underlayers with reduced lattice mismatch and higher surface binding energy to improve wetting of the deposition surface [22]. The TEM image also indicates a 5 nm region of diffusion between the MnAl and Ta cap, supporting the idea of a magnetically “dead” layer as proposed by Cui et al [7]. This 5 nm region was subtracted from the effective film thickness when calculating the order parameter, saturation magnetization, and anisotropy constant.

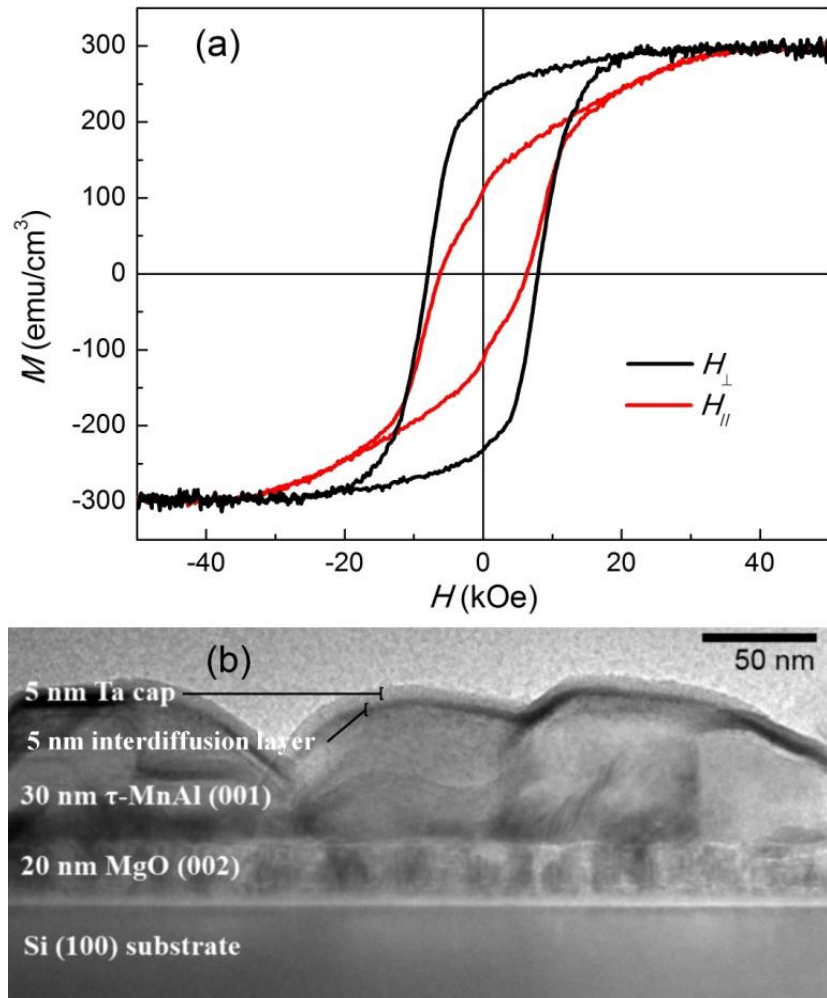


Figure 4-7 (a) Out-of-plane/in-plane magnetic hysteresis loops and (b) 50,000 magnification TEM cross-sectional image of the Si substrate/MgO (20 nm)/MnAl (30)/Ta (5) film stack deposited using 40 W DC power,  $T_s = 530$  °C, and  $T_a = 350$  °C.

It was observed throughout the investigation that improvements in out-of-plane coercivity and squareness were invariably accompanied by similar increases in in-plane coercivity and squareness. Unlike Cui's work on GaAs (001) substrates [11], no XRD peak was ever observed near  $2\theta = 47^\circ$ , which was proposed as corresponding to a partially in-plane MnAl (110) orientation. Instead, interface or diffusion effects at higher temperatures are believed to be the main contributors to in-plane magnetic behavior in these films.

This study showed that there are narrow regions of deposition conditions for producing  $\tau$ -MnAl films with high PMA, and this fact is qualitatively in agreement with recent studies done by other groups: the successful formation of  $\tau$ -MnAl thin films is highly sensitive to deposition and post-annealing conditions. However, whereas Hosoda et al. [5] and Nie et al. [6] found the optimized sputtering temperatures to be  $T_s = 200$  °C and 350 °C on MgO (001) and GaAs (001) substrates, respectively, no  $\tau$ -phase MnAl was observed in films deposited at those temperatures on Si (100) substrates. Instead, much higher temperatures were required, which contributed to the high film roughness. Therefore, further work is necessary to develop underlayers with increased surface binding energy that would improve wetting by the MnAl, thereby enabling the use of lower deposition temperatures and promoting smooth, continuous growth of  $L1_0$ -ordered  $\tau$ -MnAl thin films with improved PMA on Si substrates. Alternatively, an appropriate capping layer may also help order MnAl thin films while keeping them smooth and continuous.  $FeO_x$  capping layers have been used in such a way to produce smooth, highly ordered FePt thin films [23], and this approach may be adapted for MnAl thin films.

#### 4.4. Summary

In this chapter,  $L1_0$ -ordered  $\tau$ -phase MnAl thin films with high PMA were developed using MgO underlayers on Si substrates. Leveraging the existing body of knowledge on producing well-ordered  $L1_0$ -FePt on MgO, the structural and magnetic properties of Si substrate/MgO/MnAl sputtered film stacks were investigated by systematically varying MnAl film thickness, DC sputtering power, *in situ* substrate temperature, and post-annealing temperature. The optimized film stack of Si substrate/MgO (20 nm)/MnAl (30)/Ta (5) film stack deposited using 40 W DC power,  $T_s = 530$  °C, and  $T_a = 350$  °C exhibited a high degree of

ordering ( $S = 0.94$ ) and large PMA with out-of-plane  $H_c$  of 8 kOe,  $K_u$  of  $6.5 \times 10^6$  erg/cm<sup>3</sup>,  $M_s$  of 300 emu/cm<sup>3</sup>, and  $M_r/M_s$  of 0.8. High film roughness was observed, and methods of reducing MnAl film roughness will be studied in Chapter 6.

Despite excellent magnetic properties, the use of an insulating underlayer in STT-MRAM devices is undesirable for two major reasons: RF-sputter requirements result in low deposition rates and re-sputtering, and an insulating underlayer impedes the use of MnAl film stacks as the bottom electrode in an MTJ. In the next chapter, MnAl thin films with high PMA are developed using conductive underlayers for CMOS compatibility.

## 4.5. References

- [1] L. J. Zhu, S. H. Nie, and J. H. Zhao, “Recent progress in perpendicularly magnetized Mn-based binary alloy films,” *Chin. Phys. B*, vol. 22, p. 118505, 2013.
- [2] S. D. Granz, “Granular  $L1_0$  FePt:X (001) Thin Films for Heat Assisted Magnetic Recording,” Ph.D. Dissertation, Carnegie Mellon University, Pittsburgh, PA, 2012.
- [3] C. S. Kim, “Feasibility of a Multi-bit Cell Perpendicular Magnetic Tunnel Junction Device,” Ph.D. Dissertation, Carnegie Mellon University, Pittsburgh, PA, 2013.
- [4] K.-D. Lee, H.-S. Song, J.-W. Kim, H. S. Ko, J.-W. Sohn, B.-G. Park, and S.-C. Shin, “Gilbert damping and critical real-space trajectory of  $L1_0$  -ordered FePt films investigated by magnetic-field-induction and all-optical methods,” *Appl. Phys. Express*, vol. 7, no. 11, p. 113004, Nov. 2014.
- [5] M. Hosoda, M. Oogane, M. Kubota, T. Kubota, H. Saruyama, S. Iihama, H. Naganuma, and Y. Ando, “Fabrication of  $L1_0$ -MnAl perpendicularly magnetized thin films for perpendicular magnetic tunnel junctions,” *J. Appl. Phys.*, vol. 111, no. 7, p. 07A324, 2012.
- [6] S. H. Nie, L. J. Zhu, J. Lu, D. Pan, H. L. Wang, X. Z. Yu, J. X. Xiao, and J. H. Zhao, “Perpendicularly magnetized  $\tau$ -MnAl (001) thin films epitaxied on GaAs,” *Appl. Phys. Lett.*, vol. 102, no. 15, p. 152405, 2013.
- [7] Y. Cui, W. Yin, W. Chen, J. Lu, and S. A. Wolf, “Epitaxial  $\tau$  phase MnAl thin films on MgO (001) with thickness-dependent magnetic anisotropy,” *J. Appl. Phys.*, vol. 110, no. 10, p. 103909, 2011.
- [8] W. Van Roy, H. Bender, C. Bruynseraede, J. De Boeck, and G. Borghs, “Degree of order and magnetic properties of  $\tau$ -MnAl films,” *J. Magn. Magn. Mater.*, vol. 148, no. 1, pp. 97–98, 1995.
- [9] T. Sands, J. P. Harbison, M. L. Leadbeater, S. J. Allen, G. W. Hull, R. Ramesh, and V. G. Keramidas, “Epitaxial ferromagnetic  $\tau$ -MnAl films on GaAs,” *Appl. Phys. Lett.*, vol. 57, no. 24, p. 2609, 1990.
- [10] T. M. Rosier, Y. W. He, and N. A. El-Masry, “Ferromagnetic T-MnAl epitaxially grown on (100) GaAs substrates by pulsed laser deposition,” *Mater. Lett.*, vol. 26, p. 227, Mar. 1996.
- [11] Y. Cui, “Material Exploration for Spin Transfer Torque-Magnetic Random Access Memory,” Ph.D. Dissertation, University of Virginia, 2013.
- [12] H. Saruyama, M. Oogane, Y. Kurimoto, H. Naganuma, and Y. Ando, “Fabrication of  $L1_0$  -Ordered MnAl Films for Observation of Tunnel Magnetoresistance Effect,” *Jpn. J. Appl. Phys.*, vol. 52, no. 6R, p. 63003, Jun. 2013.
- [13] C. Y. Duan, X. P. Qiu, B. Ma, Z. Z. Zhang, and Q. Y. Jin, “The structural and magnetic properties of  $\tau$ -MnAl films prepared by Mn/Al multilayers deposition plus annealing,” *Mater. Sci. Eng. B*, vol. 162, no. 3, pp. 185–188, Jun. 2009.
- [14] M. A. Angadi and V. Thanigaimani, “Thickness dependence of the Curie temperature of MnAl films,” *J. Mater. Sci. Lett.*, vol. 11, no. 18, pp. 1213–1216, 1992.
- [15] G. A. Fischer and M. L. Rudee, “Effect of magnetic annealing on the  $\tau$ -phase of MnAl thin films,” *J. Magn. Magn. Mater.*, vol. 213, no. 3, pp. 335–339, 2000.
- [16] A. J. J. Koch, P. Hokkeling, M. G. v. d. Steeg, and K. J. de Vos, “New Material for Permanent Magnets on a Base of Mn and Al,” *J. Appl. Phys.*, vol. 31, no. 5, p. S75, 1960.
- [17] A. J. McAlister and J. L. Murray, “The (Al- Mn) Aluminum-Manganese system,” *J. Phase Equilibria*, vol. 8, no. 5, pp. 438–447, 1987.

- [18] E. Y. Huang and M. H. Kryder, "Fabrication of MnAl thin films with perpendicular anisotropy on Si substrates," *Accept. J Appl Phys Part Proc. 59th Annu. Magn. Magn. Mater. Conf. Honol. Novemb. 2014*.
- [19] A. Cebollada, D. Weller, J. Sticht, G. R. Harp, R. F. C. Farrow, R. F. Marks, R. Savoy, and J. C. Scott, "Enhanced magneto-optical Kerr effect in spontaneously ordered FePt alloys: Quantitative agreement between theory and experiment," *Phys. Rev. B*, vol. 50, no. 5, p. 3419, 1994.
- [20] S. D. Granz and M. H. Kryder, "Granular  $L1_0$  FePt (001) thin films for Heat Assisted Magnetic Recording," *J. Magn. Magn. Mater.*, vol. 324, no. 3, pp. 287–294, Feb. 2012.
- [21] B. D. Cullity, *Elements of X-Ray Diffraction*. Massachusetts: Addison-Wesley, 1956.
- [22] J. Venables, *Introduction to surface and thin film processes*. Cambridge, UK; New York: Cambridge University Press, 2000.
- [23] J.-W. Liao, K.-F. Huang, L.-W. Wang, W.-C. Tsai, W.-C. Wen, C.-C. Chiang, H.-J. Lin, F.-H. Chang, and C.-H. Lai, "Highly (001)-oriented thin continuous  $L1_0$  FePt film by introducing an  $\text{FeO}_x$  cap layer," *Appl. Phys. Lett.*, vol. 102, no. 6, p. 62420, 2013.

# Chapter 5

## *L1<sub>0</sub>*-Ordered MnAl Thin Films on Conductive Underlayers

### 5.1. Introduction

Using MgO underlayers, MnAl thin films with high PMA on Si substrates were demonstrated for the first time in Chapter 4 [1]. However, MgO is an insulator, which presents two major challenges. First, MgO must be RF-sputtered, which results in low deposition rates and re-sputtering. Second, since it is an insulator, MgO impedes the use of MnAl film stacks as the bottom electrode in an MTJ for spintronic applications.

On the other hand, TiN is electrically conductive, can be DC-sputtered for increased deposition rates, is thermally and mechanically robust, and readily forms the (001) texture on Si substrates that promotes strong *L1<sub>0</sub>*-ordering of subsequent films [2]. This could, for example, allow MnAl-based MTJs to be electrically connected to a switching element in an STT-MRAM architecture. The prevalent use of TiN as an electrode in the modern semiconductor industry indicates good deposition control and high TiN conductivity, and would help to keep the resistance-area (RA) product of an MTJ low for reduced operating currents. Furthermore, a TiN/MnAl film stack structure would be CMOS-compatible and easily integrated into state-of-the-art fabrication processes.

Another underlayer of interest is conductive (Mg<sub>0.2</sub>Ti<sub>0.8</sub>)O, which has been used as a replacement for MgO in promoting subsequent *L1<sub>0</sub>*-FePt growth [3]. FePt deposited on Cr/MgTiO underlayers was shown to wet the surface differently than that deposited on MgO

underlayers, with the former demonstrating higher film uniformity and smaller grain size, leading to lower film roughness, while still producing high degree of  $L1_0$ -ordering.

In this chapter, the fabrication and characterization of sputter-deposited  $\tau$ -MnAl thin films with high PMA using conductive TiN and MgTiO underlayers on Si substrates are investigated. Deposition parameters (*in situ* sputtering temperature, MnAl film thickness, Ar gas pressure) are systematically varied, and the structural and magnetic properties of produced films are examined. *In situ* deposition temperature is known to be a particularly critical parameter for obtaining well-ordered  $\tau$ -MnAl thin films, with the range of favorable deposition temperatures highly dependent on the substrate and underlayers used. The work in Chapter 4 showed significant nonmagnetic  $\epsilon$ -phase of MnAl in films above 50 nm, so the effects of MnAl film thickness are also studied in this chapter. Lastly, Ar gas pressure is investigated as a potential factor for altering film growth rate, film composition, and ordering. It should be noted that much of the work discussed in this chapter was previously published in reference [4].

## 5.2. Experimental Details

In this study, 1" Si (100) wafers were used as substrates. Wafers were dipped in buffered hydrofluoric acid for 20 seconds prior to loading into the sputtering chamber to strip the native oxide and promote textured growth of TiN (001). Films were sputter-deposited in the Leybold-Heraeus Z-400 Sputtering System #2 at base pressures below  $3 \times 10^{-7}$  Torr. Film stacks had the structure Si substrate/TiN (10 nm)/MgTiO (0-20)/MnAl (10-130)/Ta (5). First, the substrate was heated *in situ* to various temperatures (23 to 500 °C), which helped promote the subsequent TiN (001) texture. A 10 nm TiN seed layer was then RF sputtered (0.038 nm/s film growth rate, 5 mTorr Ar gas pressure) onto the Si substrate. Next, a 0-20 nm MgTiO film was DC magnetron

sputtered from a (Mg<sub>0.2</sub>Ti<sub>0.8</sub>)O target. A 10-130 nm MnAl film was then DC magnetron sputtered from a vacuum hot-pressed Mn<sub>48</sub>Al<sub>52</sub> target while the substrate was held at the same temperature at a deposition rate of 0.630 nm/s with an Ar gas pressure of 1-4 mTorr. The substrate was subsequently allowed to cool to room temperature, and a 5 nm Ta capping layer was DC magnetron sputtered at a deposition rate of 0.083 nm/s using Ar gas pressure of 1 mTorr. Lastly, the sample was annealed in the Micro Magnetics SpinTherm-1000 magnetic thermal annealing system with a base pressure under  $5 \times 10^{-7}$  Torr and a fixed 4 kOe field perpendicular to the film plane at 350 °C. Texture, microstructure, and magnetic properties of the film stacks were investigated using X-ray diffraction (XRD), transmission electron microscopy (TEM), alternating gradient force magnetometer (AGFM), and physical property measurement system (PPMS). Intrinsic magnetic anisotropy constants were determined according to  $K_u = H_k M_s / 2$ , where  $H_k = H_s + 4\pi M_s$  is the calculated intrinsic anisotropy field,  $H_s$  is the measured hard-axis (in-plane) saturation field,  $4\pi M_s$  is the demagnetization field contribution, and  $M_s$  is the saturation magnetization.

### 5.3. Results and Discussion

The dependences of out-of-plane coercivity ( $H_c$ ), squareness ( $M_r/M_s$ , where  $M_r$  is the remanent magnetization with no applied field), saturation magnetization ( $M_s$ ), and anisotropy constant ( $K_u$ ) on *in situ* sputtering temperature  $T_s$  were studied and the data are shown in FIG. 5-1. The 30 nm MnAl films were deposited using DC sputtering power of 40 W and annealed at  $T_a = 350$  °C. From these data,  $T_s = 400$  °C appeared to produce MnAl films with the highest PMA. This substrate temperature was therefore selected for further studies.

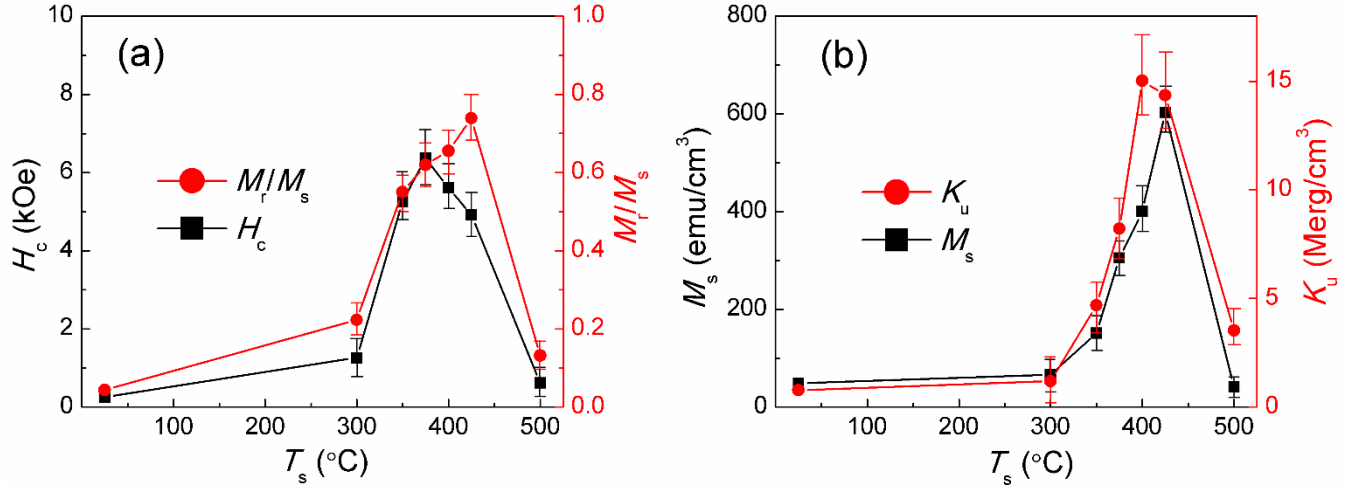


Figure 5-1 Sputtering temperature dependence of (a) out-of-plane coercivity  $H_c$  and squareness  $M_r/M_s$  and (b) saturation magnetization  $M_s$  and anisotropy constant  $K_u$  of 30 nm MnAl films deposited using 40 W DC power, 4 mTorr Ar gas pressure, and annealed at  $T_a = 350$  °C.

The thickness dependence of the magnetic properties of MnAl films was examined and is shown in FIG. 5-2. From the data,  $K_u$  and  $M_s$  appeared to be independent of film thickness, with 50 nm films demonstrating both high  $H_c$  and  $M_r/M_s$ . A brief study indicated the previously optimized *in situ* sputtering temperature of 400 °C remained favorable for 50 nm films.  $\epsilon$ -MnAl (001) peaks were observed in the  $\theta/2\theta$  XRD patterns for films 70 nm and thicker, but no significant  $\epsilon$ -MnAl (001) peaks for film thicknesses of 50 nm and below. This phenomenon was also seen in Chapter 4 using MgO underlayers, indicating the  $\tau$ -phase to be favorable up to only a certain critical film thickness. Furthermore, the critical film thickness of 50 nm corresponds well with the sharp drop in out-of-plane squareness shown in FIG. 5-2(a), suggesting the presence of  $\epsilon$ -phase MnAl greatly degrades the magnetic properties of the film.

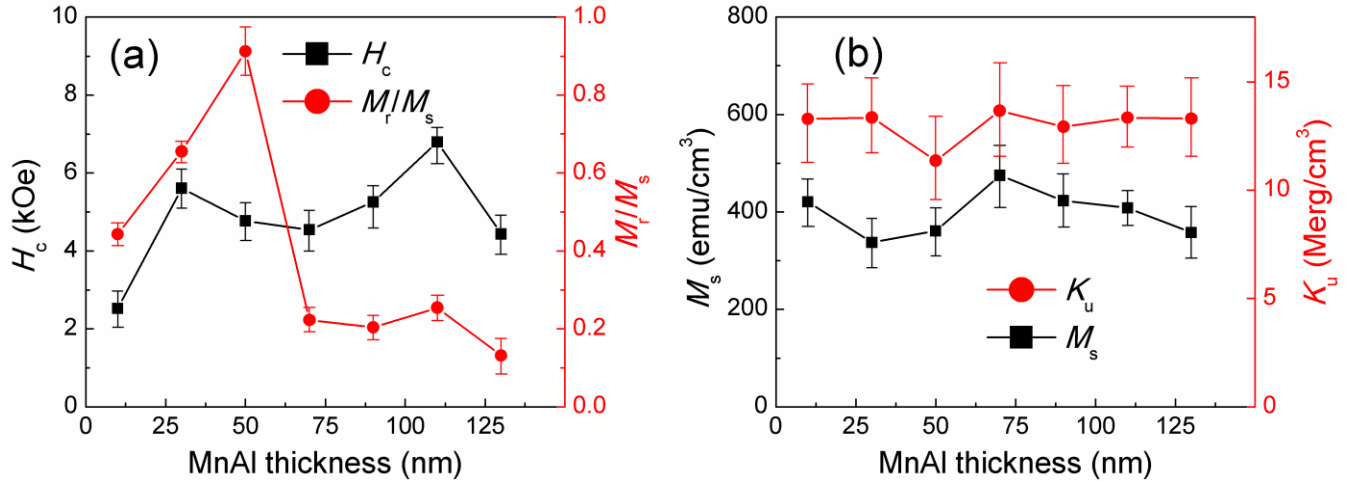


Figure 5-2 Film thickness dependence of (a) out-of-plane coercivity  $H_c$  and squareness  $M_r/M_s$  and (b) saturation magnetization  $M_s$  and anisotropy constant  $K_u$  of MnAl films deposited at  $T_s = 400$  °C using 40 W DC power and annealed at  $T_a = 350$  °C.

The effects of Ar sputtering gas pressure on magnetic properties were studied and are shown in FIG. 5-3. MnAl film composition, growth rate,  $K_u$ , and  $M_s$  were not found to differ significantly across the studied Ar gas pressure range of 1-4 mTorr. An Ar gas pressure of 1 mTorr was found to produce films with the highest  $H_c$  and  $M_r/M_s$  and was selected as the final Ar sputtering gas pressure.

Due to limitations of the SpinTherm-1000 magnetic thermal annealing system, post-annealing in the presence of a 4 kOe magnetic field applied perpendicular to the film plane was limited to a maximum of 350 °C. Samples were annealed for 30 minutes, with extended annealing times having no significant impact on the ordering and magnetic properties of the film. *In situ* post-annealing in the absence of a magnetic field was observed to have no effect on films up to annealing temperature of 570 °C.

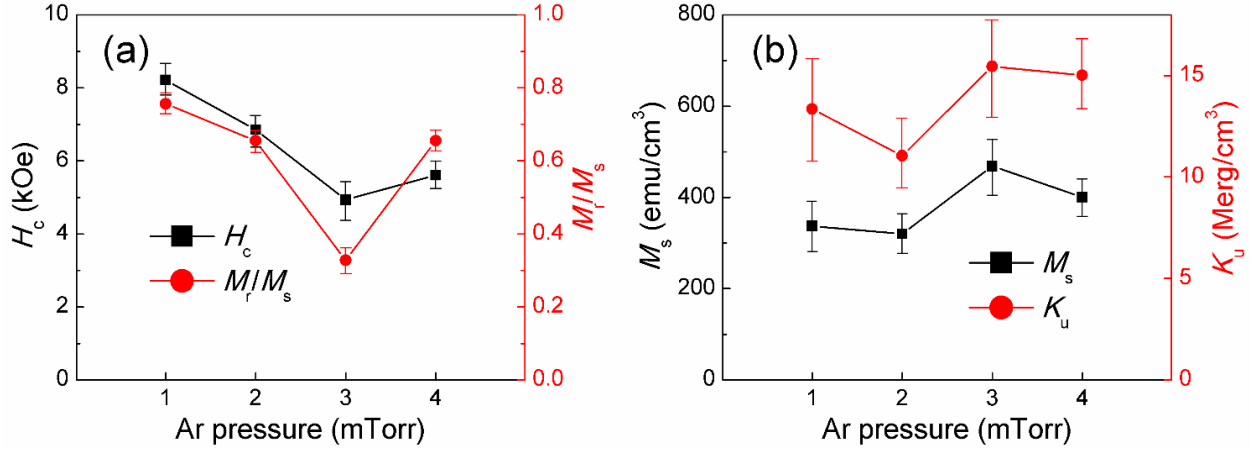


Figure 5-3 Ar gas pressure dependence of (a) out-of-plane coercivity  $H_c$  and squareness  $M_r/M_s$  and (b) saturation magnetization  $M_s$  and anisotropy constant  $K_u$  of 30 nm MnAl films deposited at  $T_s = 400$  °C using 40 W DC power and annealed at  $T_a = 350$  °C.

Ultimately, the set of deposition conditions was determined to be 50 nm of MnAl at  $T_s = 400$  °C, with Ar gas pressure of 1 mTorr, deposition rate of 0.630 nm/s, and annealing at  $T_a = 350$  °C. A film stack was fabricated using these parameters and characterized. Results are plotted in FIG. 5-4. Strong ordering of the MnAl film can be seen from the  $\theta/2\theta$  XRD pattern in FIG. 5-4(a), with the MnAl (001) and (002) peaks being measured at  $24.78^\circ$  and  $51.05^\circ$ , respectively. The rocking curve FWHM angle was found to be  $2.38^\circ$ . As shown in FIG. 5-4 (b), the film exhibited high PMA with out-of-plane  $H_c$  of 12 kOe,  $K_u$  of  $1.0 \times 10^7$  erg/cm<sup>3</sup>,  $M_s$  of 250 emu/cm<sup>3</sup>, and squareness  $M_r/M_s$  of 0.9.

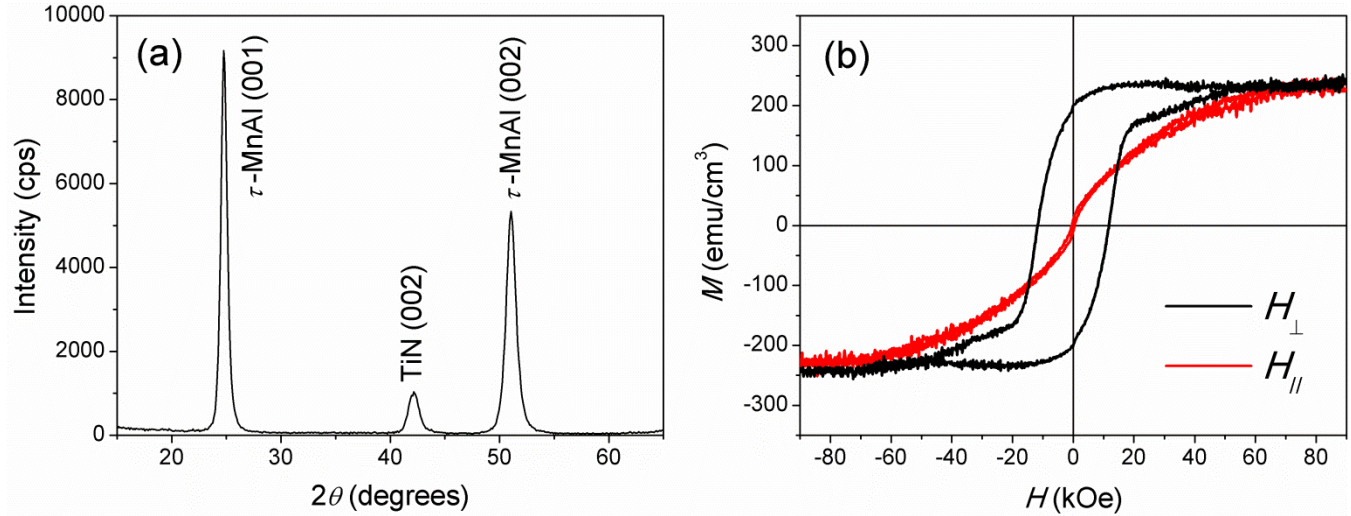


Figure 5-4 (a) Out-of-plane  $\theta/2\theta$  XRD pattern and (b) out-of-plane/in-plane magnetic hysteresis loops of the Si substrate/TiN (10 nm)/MnAl (50)/Ta (5) film stack deposited using 1 mTorr Ar gas pressure,  $T_s = 400$  °C, and  $T_a = 350$  °C.

The favorable deposition temperature range around  $T_s = 400$  °C seen in this investigation corroborates the sensitivity of  $\tau$ -MnAl formation observed in other studies [5]–[10]. Nevertheless, similar to the findings in previous work, where the optimal deposition temperature on MgO underlayer was found to be  $T_s = 530$  °C [1], the preferred deposition temperature appears to be highly dependent on the underlayer used. Additionally, using identical XRD scan parameters on MnAl films of similar thicknesses, it was found that the films deposited on TiN underlayers demonstrated order-of-magnitude stronger MnAl (001) and MnAl (002) peaks compared with those deposited on MgO underlayers. The greatly improved ordering is attributed to 1) epitaxial growth of TiN on Si substrates and 2) the slightly increased  $a$ -axis lattice parameter of TiN of 4.3 Å as compared to the MgO  $a$ -axis lattice parameter of 4.2 Å, which is expected to increase strain in the subsequent MnAl film. This strain has been proposed as a useful mechanism for promoting  $L1_0$ -ordering in FePt thin films [11], and may play a similar role

in the present work. This suggests TiN is significantly better at promoting growth of  $\tau$ -MnAl, further supported by the low rocking curve FWHM angle of  $2.38^\circ$ .

Deposited MnAl films demonstrated large grain sizes and high film roughness, which can be seen in the TEM cross-sectional image shown in FIG. 5-5. Clear lattice fringes can be seen in the MnAl film, and are consistent within each grain. This points to strong ordering that results in the high PMA observed through magnetic measurements. The diagonal patterns correspond well with the angle of grain edges, indicating the slanted interface of film growth as new material is deposited.

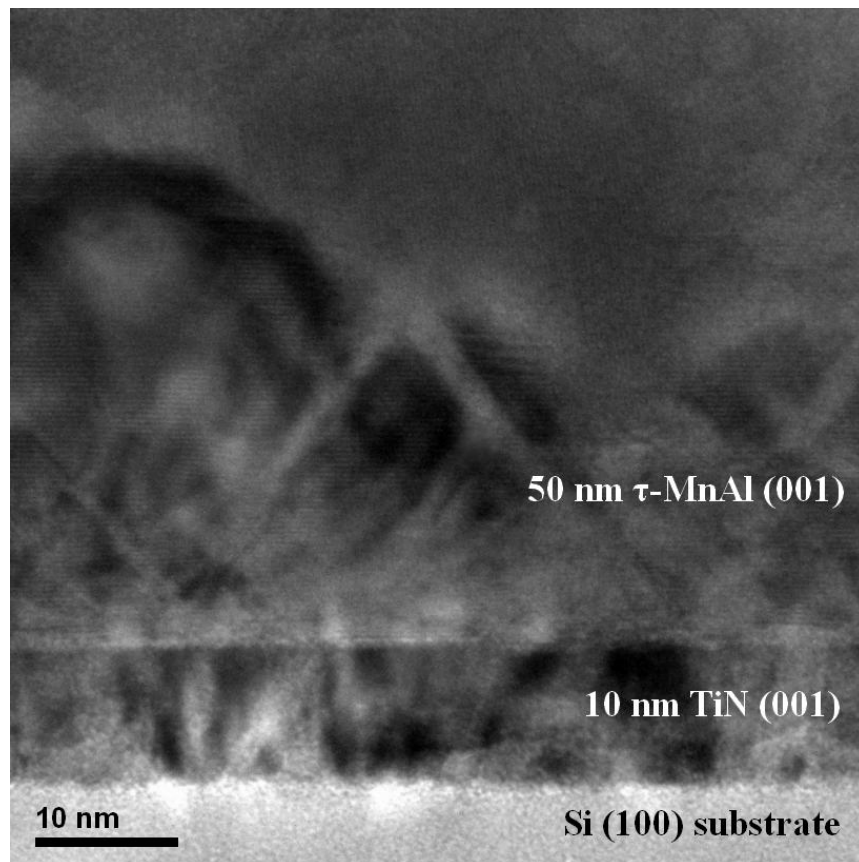


Figure 5-5 TEM cross-sectional image of the Si substrate/TiN (10 nm)/MnAl (30)/Ta (5) film stack deposited using 1 mTorr Ar gas pressure,  $T_s = 400^\circ\text{C}$ , and  $T_a = 350^\circ\text{C}$ .

Film roughness was further investigated via AFM, with root mean square (rms) surface roughness used as the representative metric. To identify which material(s) were contributing the most to the overall film stack roughness, measurements were taken after each layer in the stack. As shown in FIG. 5-6, both the HF-cleaned Si substrate and the TiN underlayer exhibited atomic-level smoothness, with the MnAl film itself dominating the overall surface roughness. Across the various deposition parameters, it was found that the overall film stack roughness was primarily determined by two factors: *in situ* temperature during MnAl deposition and MnAl film thickness. Surface roughness increased with increasing deposition temperature, up to  $T_s = 200$  °C, beyond which the roughness reached a plateau. However, as previously shown in FIG. 5-1, no significant ferromagnetic behavior was observed at deposition temperatures below 300 °C, presenting difficulties in manipulating deposition temperatures to reduce surface roughness.

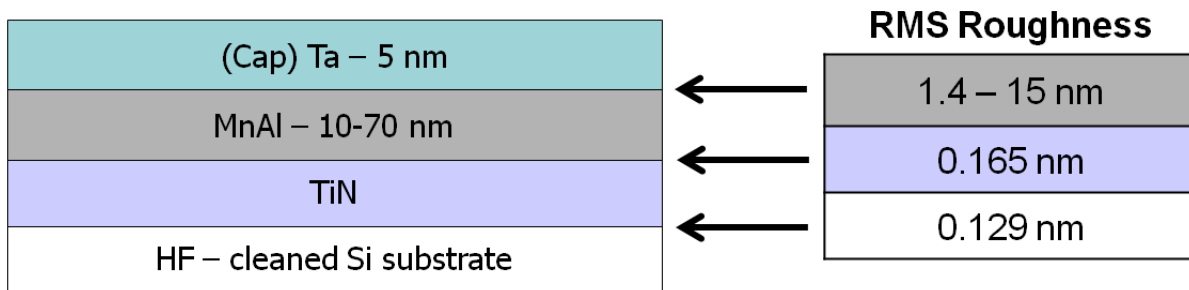


Figure 5-6 RMS roughness values after each film layer from AFM measurements.

The impact of MnAl film thickness on surface roughness was also studied, with the data plotted in FIG. 5-7. As MnAl film thickness increases up to 50 nm, so too does the film roughness. Coupled with the TEM images, this suggests the growth of MnAl films under 50 nm consists mainly of island growth, with existing grains growing along the slanted grain edges, and few new nucleation sites created. In this way, existing grains expand both laterally and vertically, increasing the film roughness. Starting at around 50 nm MnAl film thickness, the grains begin to

coalesce, and film growth becomes much more uniform, which preserves the existing film roughness. For STT-MRAM applications, the free layer is projected to be no more than 5 nm thick to keep critical switching current low. Designing an MTJ with the thin free layer as the bottom electrode should therefore mitigate roughness issues caused by film thickness.

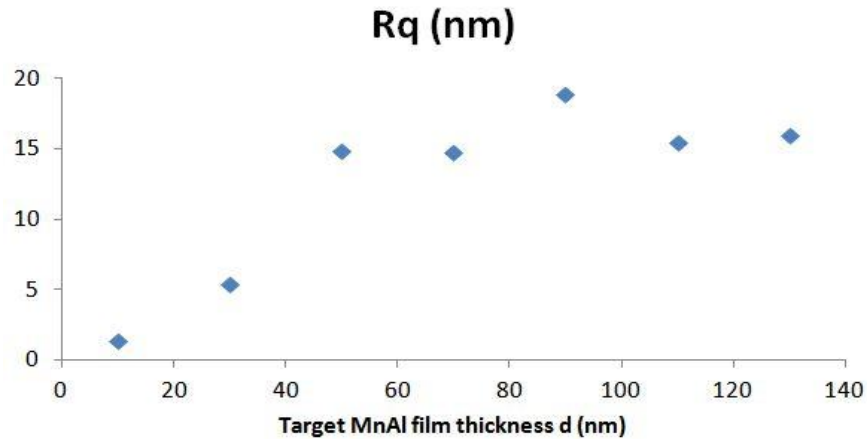


Figure 5-7 Root-mean-square surface roughness of films with varying MnAl film thicknesses.

Next, conductive ( $\text{Mg}_{0.2}\text{Ti}_{0.8}\text{O}$ ) was explored as an underlayer for promoting  $L1_0$ -MnAl growth. Just as Varaprasad et al. required 10 nm of Cr seed layer to achieve MgTiO (001) texture [3], the MgTiO in these films required a TiN seed layer to achieve the appropriate texture. Film stacks with the structure Si substrate/MgTiO/MnAl showed no MgTiO (001) texture and no significant PMA. On the other hand, films stacks of Si substrate/TiN/MgTiO/MnAl demonstrated high PMA. As seen in FIG. 5-8, an MgTiO underlayer thickness of 10 nm produced film stacks with the best magnetic properties, resulting in behavior similar to that of film stacks without the MgTiO layer. The TEM cross-sectional image, shown in FIG. 5-9, reveals no significant difference in growth morphology and surface roughness between film stacks with and without the MgTiO underlayer. Unlike previously reported in FePt film stacks

[3], the investigation revealed no significant impact of MgTiO underlayers on the wetting of MnAl films.

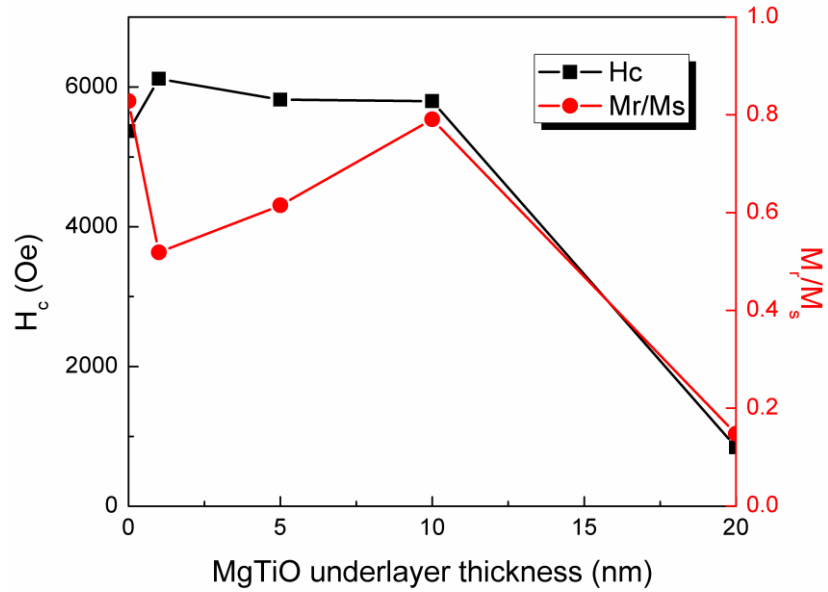


Figure 5-8 MgTiO underlayer thickness dependence of out-of-plane coercivity  $H_c$  and squareness  $M_r/M_s$  of Si substrate/TiN (10 nm)/MgTiO (0-20)/MnAl (10) film stacks deposited at  $T_s = 400$  °C and annealed at  $T_a = 350$  °C.

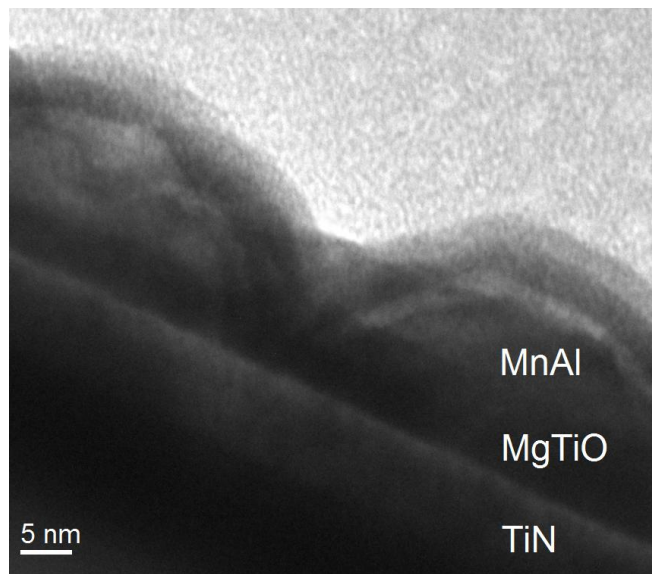


Figure 5-9 TEM cross-sectional image of the Si substrate/TiN (10 nm)/MgTiO (10)/MnAl (10) film stack deposited at  $T_s = 400$  °C and annealed at  $T_a = 350$  °C.

## 5.4. Summary

In this chapter, the use of conductive TiN and MgTiO underlayers for developing  $L1_0$ -ordered  $\tau$ -phase MnAl thin films with high PMA on Si substrates was explored. Such a CMOS-compatible stack structure would enable electrical connection to the bottom electrode. It was found that TiN (001) texture readily formed when deposited on buffer HF-cleaned Si substrates, promoting excellent  $L1_0$ -ordering in subsequent MnAl films. The 50 nm MnAl film fabricated with *in situ* sputtering temperature  $T_s = 400$  °C, Ar gas pressure of 1 mTorr, deposition rate of 0.630 nm/s, and annealing temperature  $T_a = 350$  °C showed high PMA, with out-of-plane  $H_c$  of 12 kOe,  $K_u$  of  $1.0 \times 10^7$  erg/cm<sup>3</sup>,  $M_s$  of 250 emu/cm<sup>3</sup>, and squareness  $M_r/M_s$  of 0.9.

The studies discussed here and in Chapter 4 showed that there are narrow regions of deposition conditions for producing  $\tau$ -MnAl films with high PMA, and this fact is in good agreement with existing studies: the successful formation of  $\tau$ -MnAl thin films is highly sensitive to both deposition conditions and underlayers used. In this work, the optimal deposition temperature was found to be  $T_s = 530$  °C using MgO underlayers and  $T_s = 400$  °C using TiN and MgTiO underlayers. The required ordering temperatures contributed to the high film roughness. While replacing MgO with TiN significantly decreased the necessary *in situ* deposition temperature, the film roughness remained too high for using  $L1_0$ -MnAl as the bottom electrode in an MTJ film stack. The results also indicated that keeping the MnAl films below 10 nm help greatly in keeping the surface roughness low. Contrary to existing work on FePt [3], MgTiO underlayers were not found to significantly alter the growth morphology of MnAl films, with optimized deposition parameters producing similar film roughness and magnetic hysteresis behavior with or without the MgTiO underlayer.

Overall, attractive magnetic properties were achieved with moderate temperatures compatible with CMOS BEOL processes. For STT-MRAM applications, the low Gilbert damping and moderate  $M_s$  of  $L1_0$ -MnAl would reduce the critical switching current density and allow for efficient operation of the MTJ storage cell, while the high  $K_u$  would maintain thermal stability and enable scalability. Furthermore, MnAl thin films can be DC-sputtered and are rare earth- and precious metal-free, making them both producible and economical on an industrial scale. Therefore, it is believed that Si substrates, conductive TiN underlayers, and sputter-deposition method hold great promise for the use of MnAl thin films in MTJ film stacks. Nevertheless, the high surface roughness observed in the films remains a significant challenge, and methods of addressing this issue will be investigated in Chapter 6.

## 5.5. References

- [1] E. Y. Huang and M. H. Kryder, "Fabrication of MnAl thin films with perpendicular anisotropy on Si substrates," *Accept. J Appl Phys Part Proc. 59th Annu. Magn. Magn. Mater. Conf. Honol. Novemb. 2014*.
- [2] E. Yang, S. Ratanaphan, J.-G. Zhu, and D. E. Laughlin, "Structure and magnetic properties of  $L1_0$ -FePt thin films on TiN/RuAl underlayers," *J. Appl. Phys.*, vol. 109, no. 7, p. 07B770, 2011.
- [3] B. S. D. C. S. Varaprasad, Y. K. Takahashi, A. Ajan, and K. Hono, "Electrically conductive ( $Mg_{0.2}Ti_{0.8}$ )O underlayer to grow FePt-based perpendicular recording media on glass substrates," *J. Appl. Phys.*, vol. 113, no. 20, p. 203907, 2013.
- [4] E. Y. Huang and M. H. Kryder, " $L1_0$ -Ordered MnAl Thin Films With High Perpendicular Magnetic Anisotropy Using TiN Underlayers on Si Substrates," *IEEE Trans. Magn.*, vol. 51, no. 11, pp. 1–4, Nov. 2015.
- [5] H. Saruyama, M. Oogane, Y. Kurimoto, H. Naganuma, and Y. Ando, "Fabrication of  $L1_0$  - Ordered MnAl Films for Observation of Tunnel Magnetoresistance Effect," *Jpn. J. Appl. Phys.*, vol. 52, no. 6R, p. 63003, Jun. 2013.
- [6] T. Sands, J. P. Harbison, M. L. Leadbeater, S. J. Allen, G. W. Hull, R. Ramesh, and V. G. Keramidas, "Epitaxial ferromagnetic  $\tau$ -MnAl films on GaAs," *Appl. Phys. Lett.*, vol. 57, no. 24, p. 2609, 1990.
- [7] M. Hosoda, M. Oogane, M. Kubota, T. Kubota, H. Saruyama, S. Iihama, H. Naganuma, and Y. Ando, "Fabrication of  $L1_0$ -MnAl perpendicularly magnetized thin films for perpendicular magnetic tunnel junctions," *J. Appl. Phys.*, vol. 111, no. 7, p. 07A324, 2012.
- [8] L. J. Zhu, S. H. Nie, and J. H. Zhao, "Recent progress in perpendicularly magnetized Mn-based binary alloy films," *Chin. Phys. B*, vol. 22, p. 118505, 2013.
- [9] S. H. Nie, L. J. Zhu, J. Lu, D. Pan, H. L. Wang, X. Z. Yu, J. X. Xiao, and J. H. Zhao, "Perpendicularly magnetized  $\tau$ -MnAl (001) thin films epitaxied on GaAs," *Appl. Phys. Lett.*, vol. 102, no. 15, p. 152405, 2013.
- [10] Y. Cui, W. Yin, W. Chen, J. Lu, and S. A. Wolf, "Epitaxial  $\tau$  phase MnAl thin films on MgO (001) with thickness-dependent magnetic anisotropy," *J. Appl. Phys.*, vol. 110, no. 10, p. 103909, 2011.
- [11] Y. F. Ding, J. S. Chen, E. Liu, C. J. Sun, and G. M. Chow, "Effect of lattice mismatch on chemical ordering of epitaxial  $L1_0$  FePt films," *J. Appl. Phys.*, vol. 97, no. 10, p. 10H303, 2005.

# Chapter 6

## Addressing MnAl Film Roughness

### 6.1. Introduction

In Chapters 4 and 5,  $L1_0$ -MnAl thin films with high PMA were developed on Si substrates. However, the observed high MnAl film roughness is a significant barrier to the use of  $L1_0$ -MnAl in MTJ film stacks for STT-MRAM applications, since scaled tunnel barriers must be less than 1 nm thick and continuous. The film roughness was primarily attributed to two factors: MnAl film thickness and  $L1_0$ -ordering temperature. As previously discussed, the contribution of MnAl film thickness to film roughness can be mitigated through careful design of the MTJ film stack by designating the bottom film as the thin free layer (< 5 nm). The main challenge to achieving smooth MnAl films is therefore the high *in situ* deposition temperature required to achieve good  $L1_0$ -ordering.

In this chapter, three approaches to reducing  $L1_0$ -MnAl ordering temperature and film roughness are investigated: adding other materials to the MnAl film (Section 6.2), using various underlayers in conjunction with additions to MnAl (6.2), and utilizing alternative post-annealing methods (6.3).

### 6.2. Additions to MnAl Film

Considerable work has been done by others on introducing additional elements into bulk MnAl and thick MnAl films in an attempt to stabilize the structure. Dopants such as carbon [1]–

[4], boron [3], nickel [5], zinc [6], and others have been studied as possible candidates, with some showing promise in stabilizing MnAl. However, the difficulty in growing MnAl thin films with high PMA has resulted in no thorough examination of these dopants in thin films. In this section, the effects of introducing Ni (6.2.1), C (6.2.2), and SiO<sub>x</sub> (6.2.3) to MnAl thin films are investigated in an effort to reduce the ordering temperature and thereby reduce the MnAl film roughness.

### **6.2.1 MnAl:Ni**

Matsumoto et al. [5] previously investigated the effects of introducing Ni into 700 nm thick films of MnAl, sputtered at  $T_s = 150$  °C. They found that a Ni content of 3 atomic percent resulted in maximum PMA, with saturation magnetization increasing from approximately 110 emu/cm<sup>3</sup> at 0% Ni to 240 emu/cm<sup>3</sup> at 3% Ni, and out-of-plane coercivity increasing from 1.8 kOe at 0% Ni to 2.9 kOe at 3% Ni. They proposed that the dopant atom displaces Mn atoms which would otherwise occupy Al sites. Since adjacent Mn atoms in the lattice give rise to antiferromagnetic coupling and degrade the overall ferromagnetic properties of the material, the introduction of dopant atoms to replace excess Mn atoms in the lattice could help to stabilize the structure, reduce the ordering temperature, and enhance the ferromagnetic properties. Based on these results, 3% Ni was selected for study in MnAl thin films.

## **Experimental Details**

In this study, 1” Si (100) wafers were used as substrates. Wafers were dipped in buffered hydrofluoric acid for 20 seconds prior to loading into the sputtering chamber to strip the native oxide and promote textured growth of the underlayer. Films were sputter-deposited in the

Leybold-Heraeus Z-400 Sputtering System #2 at base pressures below  $3 \times 10^{-7}$  Torr. Film stacks had the structure Si substrate/underlayer/MnAlNi (5-100 nm). First, the substrate was heated *in situ* to various temperatures (23 to 500 °C), which helped promote the necessary underlayer texture. The underlayer was then sputtered onto the substrate. Next, a 5-100 nm MnAl film was then DC magnetron sputtered from a vacuum hot-pressed  $\text{Mn}_{45.33}\text{Al}_{52.00}\text{Ni}_{2.67}$  target while the substrate was held at the same temperature with an Ar gas pressure of 1 mTorr. Texture, microstructure, and magnetic properties of the film stacks were investigated using TEM, AFM, and PPMS.

## Results and Discussion

The effects of *in situ* sputtering temperature  $T_s$  on PMA (represented by out-of-plane coercivity  $H_c$ ) and film roughness (represented by root-mean-square surface roughness  $R_q$ ) were studied and the data are plotted in FIG. 6-1. The film stacks had the structure Si substrate/TiN (15 nm)/MnAlNi (5 nm). Similar to the previous work on MnAl films in Chapter 5,  $T_s = 400$  °C appeared to produce MnAlNi films with the highest PMA. However, the data also show the RMS roughness increases to  $R_q = 0.7$  nm at  $T_s = 300$  °C, while  $T_s = 350$  °C is necessary for significant PMA in the MnAlNi thin films. A surface contour plot measured by AFM of the MnAlNi film deposited at  $T_s = 500$  °C is shown in FIG. 6-2. The large peak-to-peak height of approximately 7 nm presents significant difficulties in attempting to deposit a thin, continuous tunnel barrier on top.

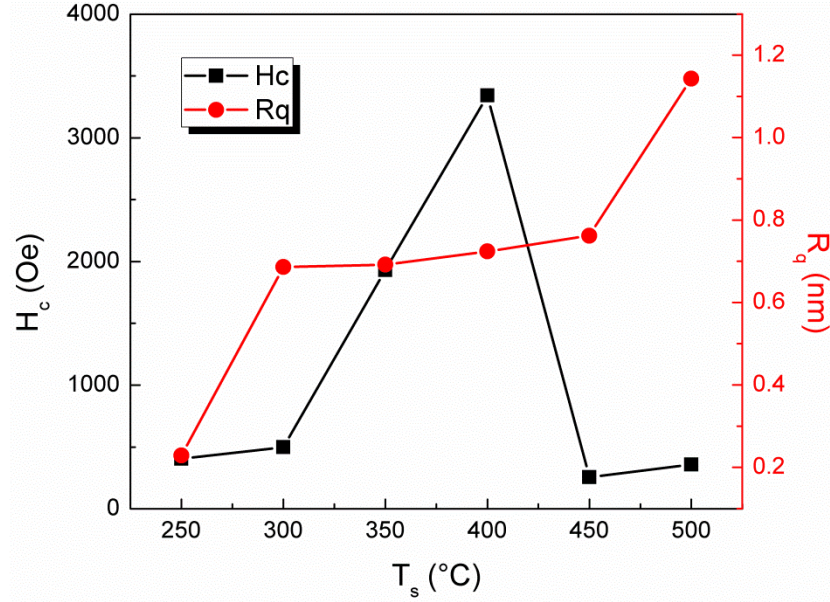


Figure 6-1 Sputtering temperature dependence of out-of-plane coercivity  $H_c$  and root-mean-square surface roughness  $R_q$  of 5 nm MnAlNi films.

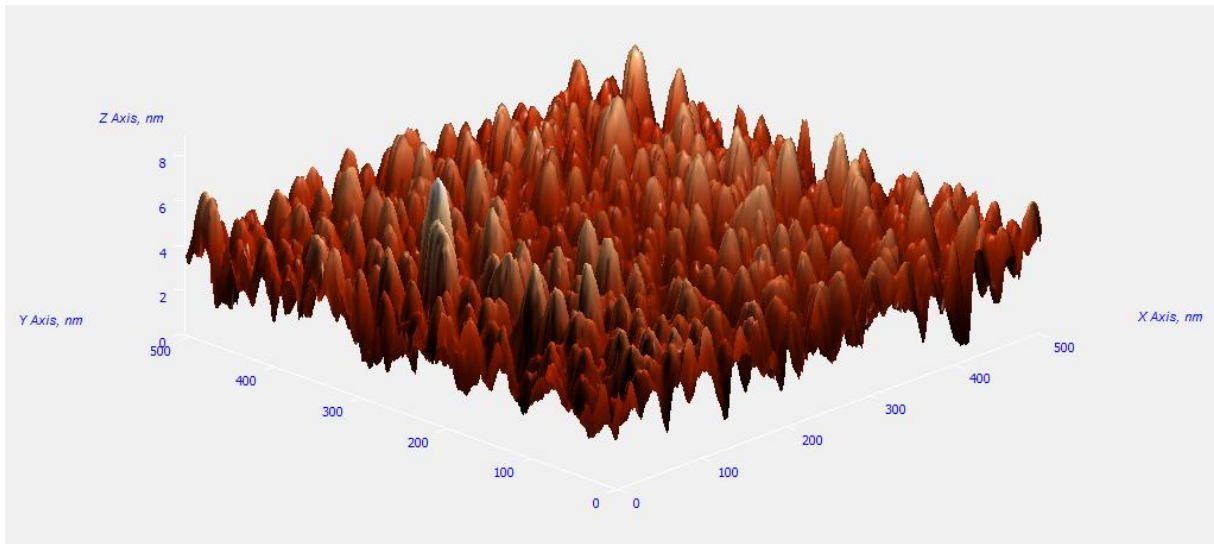


Figure 6-2 AFM surface contour plot of 5 nm MnAlNi film deposited at  $T_s = 500$  °C.

As was observed in Chapters 4 and 5, different underlayer materials can drastically affect the ordering of MnAl-based thin films. Following this reasoning, the effects of various underlayers on MnAlNi thin films were investigated. FIG. 6-3 shows the effect of  $Mg_{0.2}Ti_{0.8}O$

(also examined in Chapter 5) on buffer HF-cleaned Si substrate/TiN (15 nm)/MgTiO (0.9)/MnAlNi (10-100) film stacks. In similar fashion to MnAl films, MnAlNi films increase rapidly in surface roughness up to a film thickness of 50 nm. As PMA is degraded with increasing MnAlNi thickness, keeping the MnAlNi films under 10 nm is advantageous for both high PMA and reduced surface roughness.

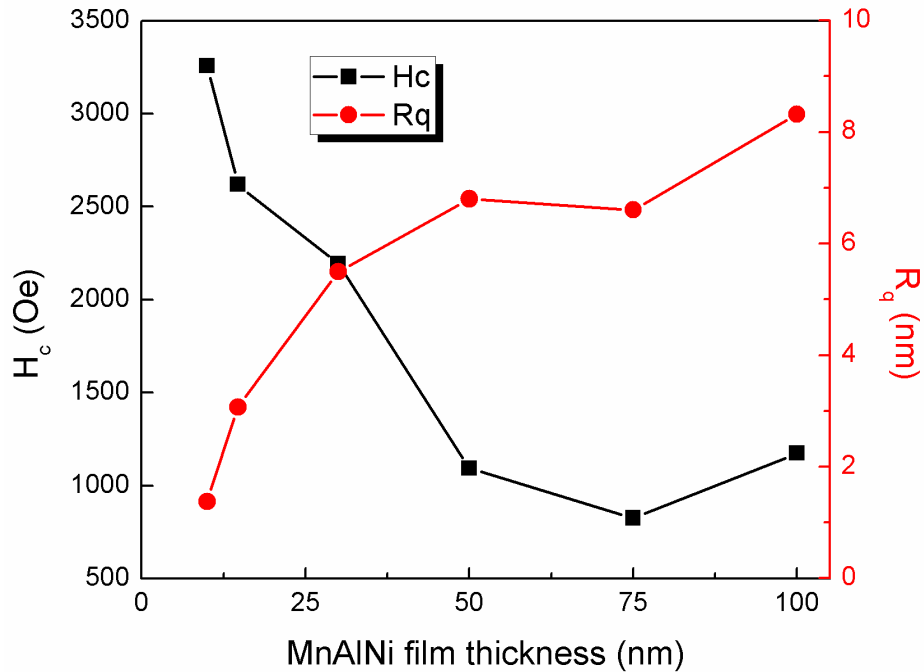


Figure 6-3 MnAlNi film thickness dependence of out-of-plane coercivity  $H_c$  and root-mean-square surface roughness  $R_q$  of Si substrate/TiN (15 nm)/MgTiO (0.9 nm)/MnAlNi (10-100 nm) film stacks deposited at  $T_s = 400$  °C.

The impact of MgTiO thickness on out-of-plane coercivity ( $H_c$ ) and saturation magnetization ( $M_s$ ) was also examined, with results shown in FIG. 6-4. PMA was observed to decrease with increasing MgTiO thickness. Just as in Chapter 5, MgTiO was not found to have a positive effect on the subsequent MnAl-based film. In fact, the MgTiO itself quickly lost the necessary texture to promote  $L1_0$ -ordering in the subsequent film as the MgTiO layer increased

in thickness. Film stacks without the initial TiN seed layer did not exhibit significant PMA. The TEM cross-sectional image of a Si substrate/TiN (15 nm)/MgTiO (2)/MnAlNi (5) film stack, shown in FIG. 6-5, shows clear and consistent lattice fringes throughout each film layer, but reveals large MnAlNi grain size and angled grain edge similar to those of the MnAl films studied in Chapters 4 and 5.

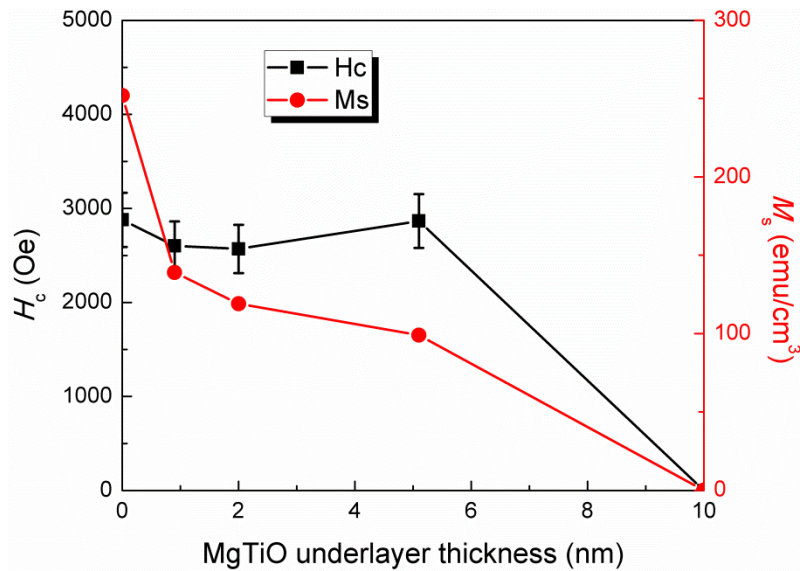


Figure 6-4 MgTiO underlayer thickness dependence of out-of-plane coercivity  $H_c$  and saturation magnetization  $M_s$  of Si Substrate/TiN (15 nm)/MgTiO (0-10)/MnAlNi (5) film stacks.

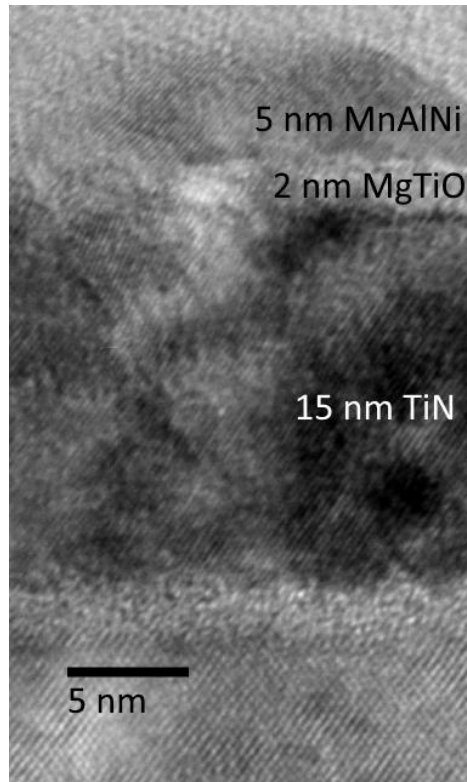


Figure 6-5 TEM cross-sectional image of the Si/TiN (15 nm)/MgTiO (2)/MnAlNi (5) film stack.

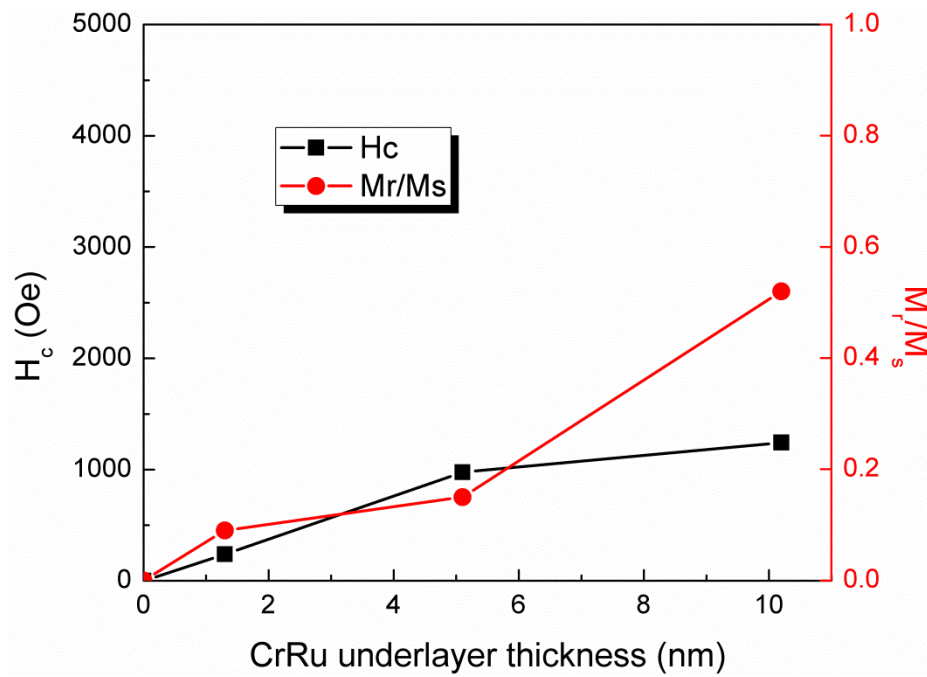


Figure 6-6 CrRu underlayer thickness dependence of out-of-plane coercivity  $H_c$  and squareness  $M_r/M_s$  of Si substrate/CrRu (0-10 nm)/MnAlNi (5) film stacks.

Prior studies done by Kim et al. [7] had indicated CrRu as a useful underlayer for promoting  $L1_0$ -ordering in FePt thin films. The use of CrRu as an underlayer for MnAlNi thin films was therefore investigated. Film stacks of buffer HF-cleaned Si substrate/CrRu (0-10 nm)/MnAlNi (5) were fabricated and characterized, with out-of-plane coercivity  $H_c$  and squareness  $M_r/M_s$  shown in FIG. 6-6. Although the PMA of the films was observed to increase gradually with increasing CrRu underlayer thickness, the values remain much smaller than those of MnAlNi films deposited on TiN or TiN/MgTiO underlayers. Given the effectiveness of TiN at promoting  $L1_0$ -ordering in MnAl films and its crucial role in seeding MgTiO underlayers, film stacks of buffer HF-cleaned Si substrate/TiN (15 nm)/CrRu (0-10)/MnAlNi (5) were studied, and the data are plotted in FIG. 6-7. The results indicate adding a TiN seed layer beneath CrRu does not improve the magnetic properties of the subsequent MnAlNi film. Instead, any thickness of CrRu on top of TiN only degraded the PMA of the film stack.

Overall, introducing a fixed 3% Ni by volume degraded PMA of MnAl-based thin films and did not noticeably reduce the surface roughness.

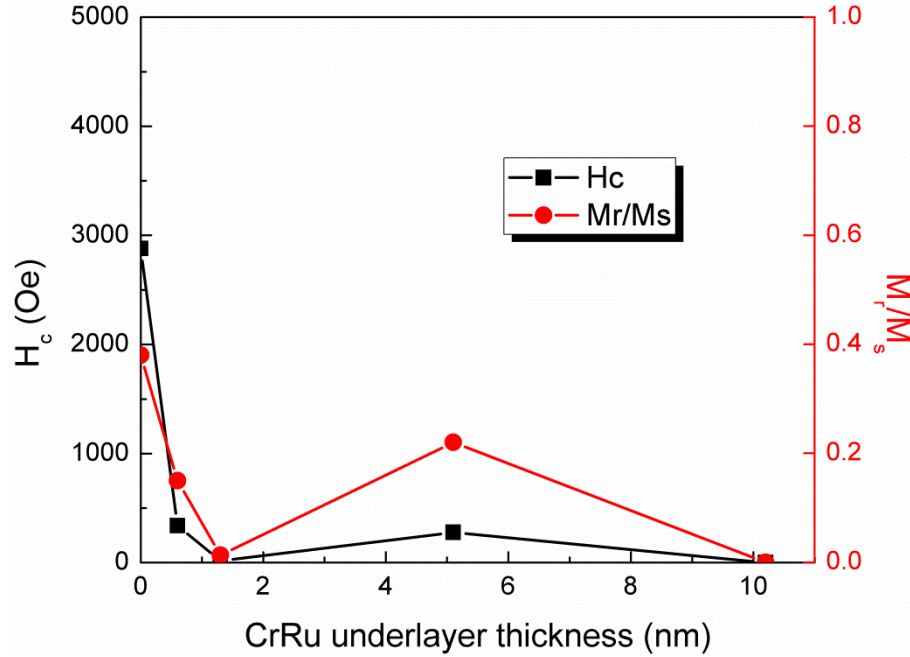


Figure 6-7 CrRu underlayer thickness dependence of out-of-plane coercivity  $H_c$  and squareness  $M_r/M_s$  of Si substrate/TiN (15 nm)/CrRu (0-10)/MnAlNi (5) film stacks.

## 5.2.2 MnAl:C

Several prior studies [1]–[4] have investigated the effects of introducing carbon into MnAl. The same mechanism of substituting for excess Mn atoms in Al lattice sites was proposed. Furthermore, since carbon has a much smaller atomic radius than nickel, the dopant is less likely to distort the lattice. Nevertheless, results have been varied. For example, Pareti et al. found that the PMA of bulk samples decreased with increasing carbon content [1]. On the other hand, Zeng et al. found 3% carbon resulted in powders with the maximum coercivity of 5.2 kOe [2], while Liu et al. concluded 1.7% carbon produced alloy ingots with the maximum coercivity of 1.5 kOe [3]. In this section, the effect of C dopants on MnAl thin films is examined.

## Experimental Details

The substrates used in this study were 1” (100) Si wafers. Wafers were dipped in buffered hydrofluoric acid for 20 seconds prior to loading into the sputtering chamber to strip the native oxide and promote textured growth of TiN (001). All films were deposited in the Custom 5-Target Sputtering System #2 at base pressures below  $3 \times 10^{-7}$  Torr. As there was no access to a sputtering system with co-sputtering capabilities, MnAl and C were alternately deposited with thicknesses corresponding to carbon volume percentages ranging from 1-9%. Film stacks followed the structure Si substrate/TiN (15 nm)/[MnAl/C]<sub>x</sub>. First, the substrate was heated *in situ* to 400 °C, which helped promote the subsequent TiN (001) texture. Next, a 15 nm TiN seed layer was then RF sputtered onto the Si substrate. MnAl film was then DC magnetron sputtered from a vacuum hot-pressed Mn<sub>48</sub>Al<sub>52</sub> target, alternating with C film that was RF sputtered. Total nominal film thickness of the MnAl/C multilayers was 10 nm. Texture, microstructure, and magnetic properties of the film stacks were investigated using TEM, AFM, and PPMS.

## Results and Discussion

The effects of carbon volume percentage on PMA and surface roughness were studied, with one set of samples having the MnAl deposited first, and the other with C deposited first. Results are plotted in FIG. 6-8 and FIG. 6-9, respectively. Though both sets of samples demonstrated similar properties with carbon volumes 3% and higher, MnAl-first samples showed severe degradation of PMA at 1%C, while C-first samples exhibited an increase in PMA at 1%C. To explain this phenomenon, the samples were examined with TEM, with a cross-sectional image of a C-first, 1%C sample shown in FIG. 6-10. The darker MnAl:C grains appear to be encapsulated in a lighter contrast material. The TEM image of the TiN/MnAl:C interface shown

in FIG. 6-11 reveals excellent epitaxy between the TiN underlayer and the darker MnAl:C material, with clear and consistent lattice fringes indicating good texture. However, there are also lattice fringes evident in the lighter encapsulating material, with spacing identical to those inside the darker grains. In fact, some of the fringes continue from the darker material into the lighter, which can also be seen in FIG. 6-12. This suggests that the partly crystalline, lighter material is some mixture of MnAl and C. The darker region is believed to have lower carbon content than the lighter region, with some of the carbon diffusing out to the grain edges during the high-temperature deposition, discussed below.

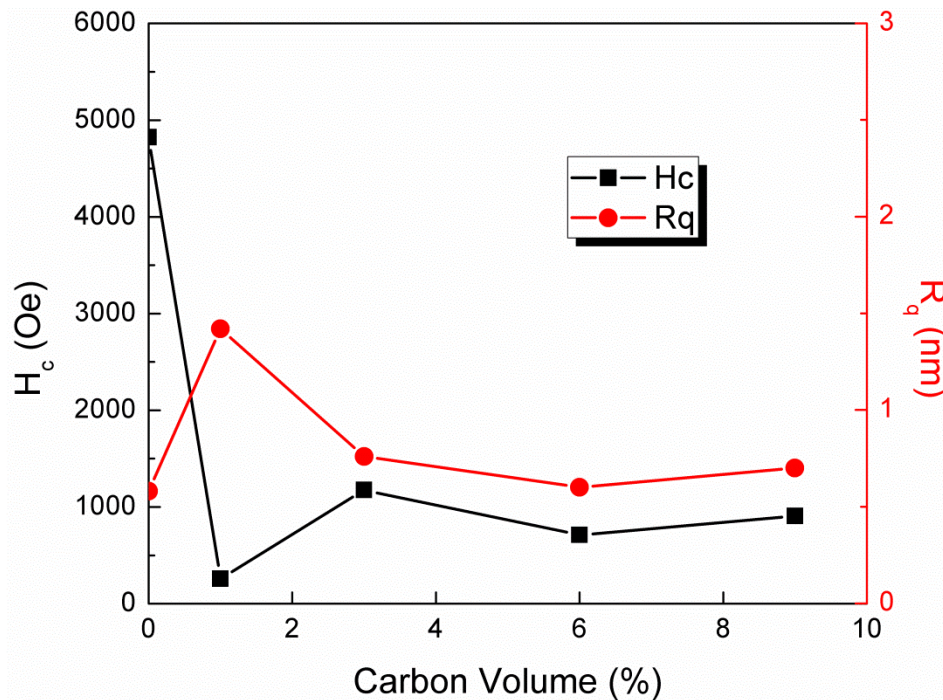


Figure 6-8 Carbon volume percentage dependence of out-of-plane coercivity  $H_c$  and root-mean-square surface roughness  $R_q$  of 10 nm MnAl:C films with MnAl deposited first.

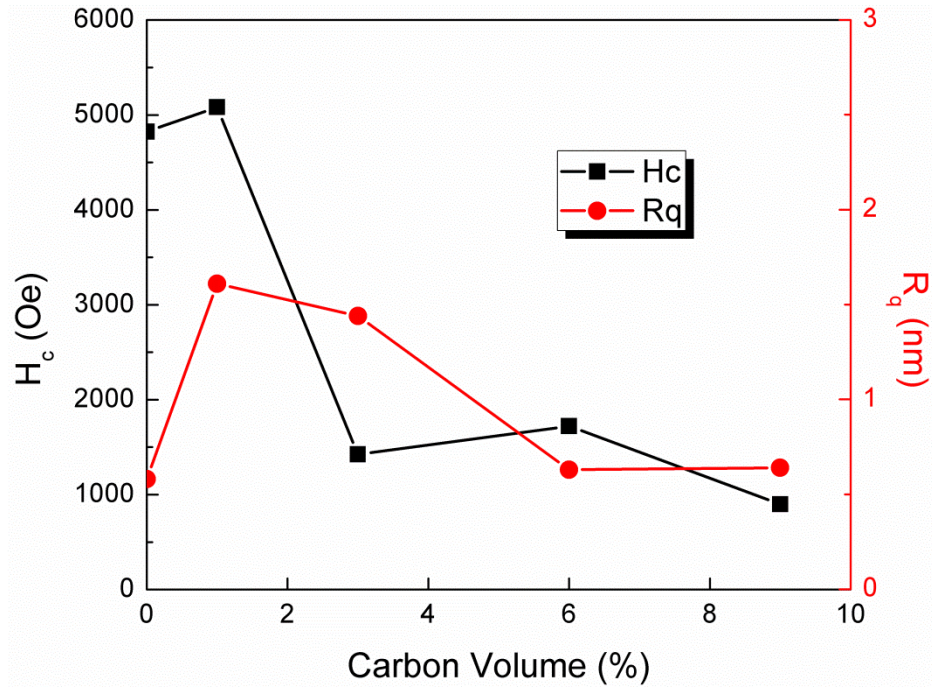


Figure 6-9 Carbon volume percentage dependence of out-of-plane coercivity  $H_c$  and root-mean-square surface roughness  $R_q$  of 10 nm MnAl:C films with C deposited first.

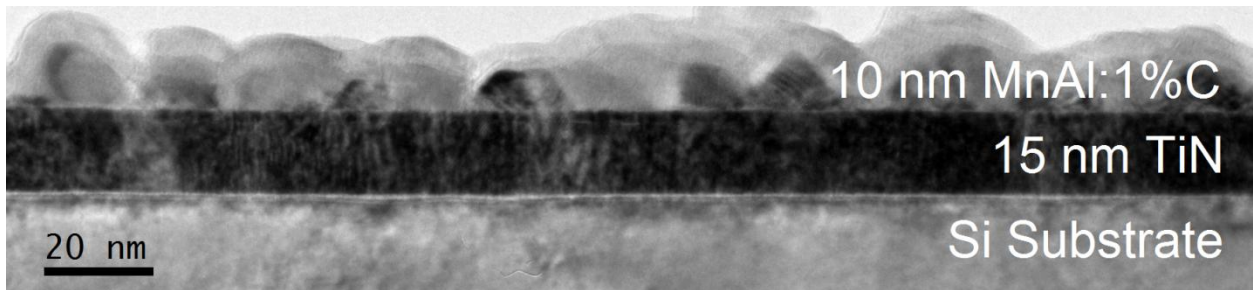


Figure 6-10 TEM cross-sectional image of a 10 nm MnAl:1%C film with C deposited first.

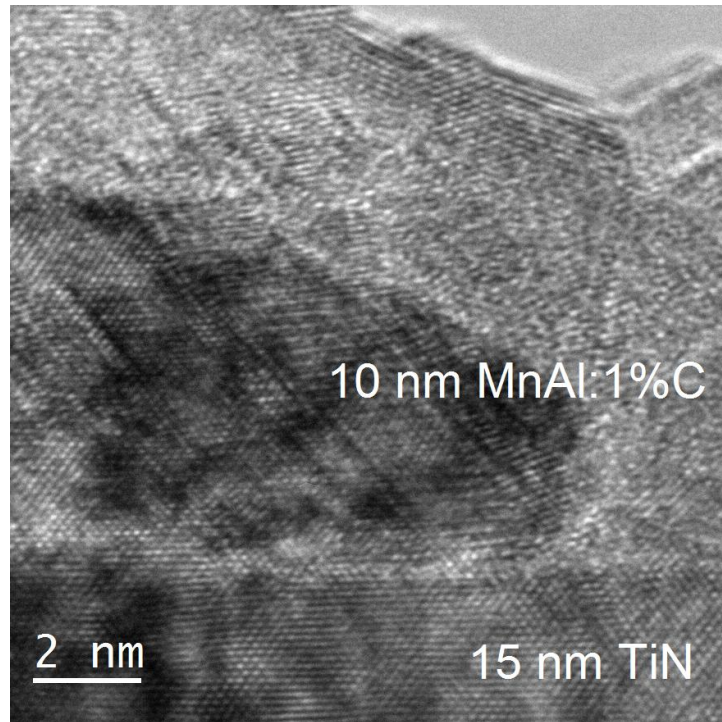


Figure 6-11 TEM cross-sectional image at TiN/MnAl:1%C interface of a 10 nm MnAl:1%C film with C deposited first.

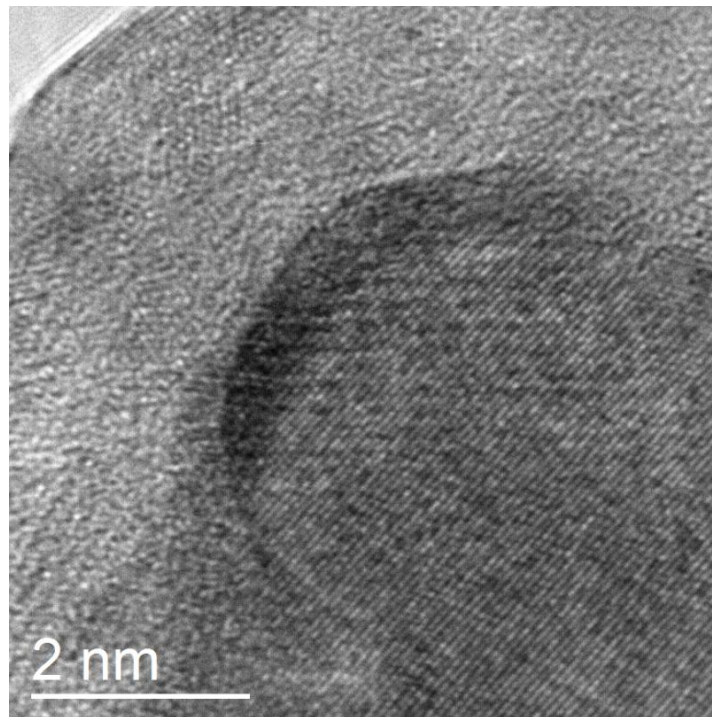


Figure 6-12 TEM cross-sectional image at dark/light boundary of a 10 nm MnAl:1%C film with C deposited first.

Existing work [6] has indicated 1.7 atomic %C to be the solubility limit for carbon in MnAl alloys, with higher amounts of carbon expected to diffuse to grain boundaries and degrade the overall magnetic properties. Given the imprecise nature of sputtering alternating layers of such thin films and density variations, it is difficult to accurately translate the volume %C in this work to atomic %C. Nevertheless, considering the atomic radius of C is approximately half that of Mn and Al, and C content is much lower than that of either Mn or Al, volume %C can be multiplied by 4 to arrive at a simple equivalent in atomic %C. Using this method, 1%C by volume is approximately 4 atomic %C. This is greater than the solubility limit of 1.7 atomic %C, which supports the idea that excess carbon is diffusing to the grain boundaries and explains the contrast difference seen in the TEM images. The difference between MnAl-first and C-first samples is also attributed to this diffusion mechanism. When MnAl is deposited first, purely MnAl grains are initially formed. As the C is deposited on top, it diffuses to the grain boundaries without a significant portion going through the MnAl grains. On the other hand, when C is deposited first, followed by MnAl, the existing C diffuses through the MnAl as the MnAl grains are forming. A portion of the C atoms are thereby embedded within the MnAl lattice, producing the PMA enhancement predicted by the theory. The excess C atoms still diffuse to the grain boundaries, as evidenced in the TEM images discussed previously. Regardless of which is deposited first, however, having a C content much higher than the solubility limit means the sheer amount of C cannot be confined to the grain boundaries. Instead, there is so much C that not enough exposed MnAl area is available for subsequent  $L1_0$ -MnAl to continue growing. A similar effect has been seen in FePt:C films, with excess C atoms “capping off” existing grains, interfering with further ordered growth [8]. Given the deposition method of alternating sub-nanometer material layers, 1 volume %C was the lower limit of this study.

Overall, adding 1 volume %C was found to increase PMA, with coercivity increasing from 4.8 kOe to 5.1 kOe, though this increase was also accompanied by an increase in film roughness from 0.6 nm to 1.6 nm RMS roughness.

### 6.2.3 MnAl:SiO<sub>x</sub>

SiO<sub>x</sub> has been used as a segregant in FePt HAMR media [9], and its effect on MnAl films was examined. The same methodology of alternating MnAl/SiO<sub>x</sub> layers used in Section 6.2.2 was applied. Unlike the MnAl:C study, no significant difference was found between MnAl-first and SiO<sub>x</sub>-first samples, with any amount of SiO<sub>x</sub> severely degrading PMA and increasing the film roughness, as shown in FIG. 6-13.

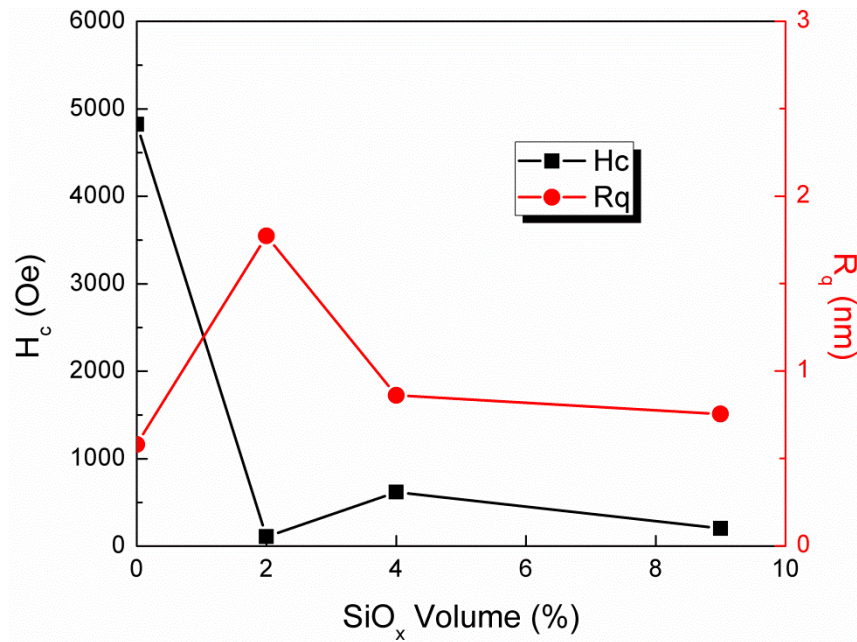


Figure 6-13 SiO<sub>x</sub> volume percentage dependence of out-of-plane coercivity  $H_c$  and root-mean-square surface roughness  $R_q$  of 10 nm MnAl:SiO<sub>x</sub> films deposited on buffer HF-cleaned Si substrate/TiN (15 nm).

### 6.3. Post-Annealing Methods

Aside from elevated *in situ* deposition temperature,  $L1_0$ -ordering can also be achieved through a variety of post-annealing techniques. However, whereas high-temperature deposition involves incident atoms moving primarily along the surface of the substrate, annealing requires atoms diffusing through a volume. This shift from a predominantly 2-dimensional problem to an inherently 3-dimensional process demands a significant increase in thermal energy. For example, if annealing is the sole method of ordering the film, one would expect a much higher temperature  $T_a$  than the optimal deposition temperature of  $T_s = 400$  °C observed in MnAl thin films deposited on TiN underlayers. Indeed, the small impact of annealing seen in Chapters 4 and 5 is consistent with this concept, since the Micro Magnetics SpinTherm-1000 magnetic thermal annealing system used had a maximum annealing temperature of  $T_a = 350$  °C. Using post-annealing methods with higher temperatures may allow ordering of the films purely through the annealing process. Furthermore, since MnAl films deposited at low temperature show reduced surface roughness, relying solely on annealing to order the films may ultimately result in smoother film stacks. In this section, the effects of post-annealing MnAl thin films with a tube annealing furnace and rapid thermal annealing are described.

#### 6.3.1 Experimental Details

The substrates used in this study were 1” (100) Si wafers. Some sample sets were dipped in buffered hydrofluoric acid for 20 seconds prior to loading into the sputtering chamber to strip the native oxide. The rest retained the native oxide. Films were deposited in the Custom 5-Target Sputtering System #2 or the Leybold-Heraeus Z-400 Sputtering System #2 at base pressures

below  $3 \times 10^{-7}$  Torr. The substrate was held at *in situ* temperature  $T_s = \text{RT}-300$  °C. An underlayer, if present, consisted of 10 nm TiN deposited via RF sputtering, or 10 nm of MgTiO deposited via DC magnetron sputtering. A 5-15 nm MnAl film was then DC magnetron sputtered. Finally, samples were annealed either in the Tube Annealing Furnace for 2 hours at various temperatures ( $T_a = 600-900$  °C) or in the AG Associates Heat Pulse Rapid Thermal Annealing System for 20 minutes at various temperatures ( $T_a = 550-850$  °C). For annealing in RTA, since the majority of annealing effects are attributed to the target annealing temperature rather than the ramp rate [10]–[11], the ramp rate was fixed at 40 °C/s. Texture, microstructure, and magnetic properties of the film stacks were investigated using TEM and PPMS.

### 6.3.2 Results and Discussion

First, samples with the simple structure of natively oxidized Si substrate/MnAl (5-15 nm, deposited at room temperature) were fabricated, annealed and characterized, with results plotted in FIG. 6-15 and FIG. 6-16 for 5 nm and 15 nm MnAl films, respectively. The samples annealed with RTA exhibited significant PMA at lower temperatures than those annealed with the tube furnace, though the maximum achieved PMA was also lower in RTA-annealed samples than in furnace-annealed samples. Comparing FIG. 6-15 and FIG. 6-16 reveals the 5 nm films show better PMA at every temperature for both annealing methods. Since thermal energy is applied from a surface (the substrate side in tube annealing and the top side in RTA), and must travel through the volume of the film, thicker films are indeed expected to be less affected by annealing. Further evidence for this can be seen in the TEM image of a RTA-annealed sample shown in FIG. 6-14. The lattice fringes in the MnAl layer are primarily near the film surface, extending down through the film, rather than growing up from the Si/MnAl interface. Film

roughness also appears much lower than that of samples examined in Chapter 4, Chapter 5, and Section 6.2. Nonetheless, none of the samples studied in this section showed coercivity above 1.5 kOe, whereas films optimized in previous chapters exhibited coercivity from 8-12 kOe.

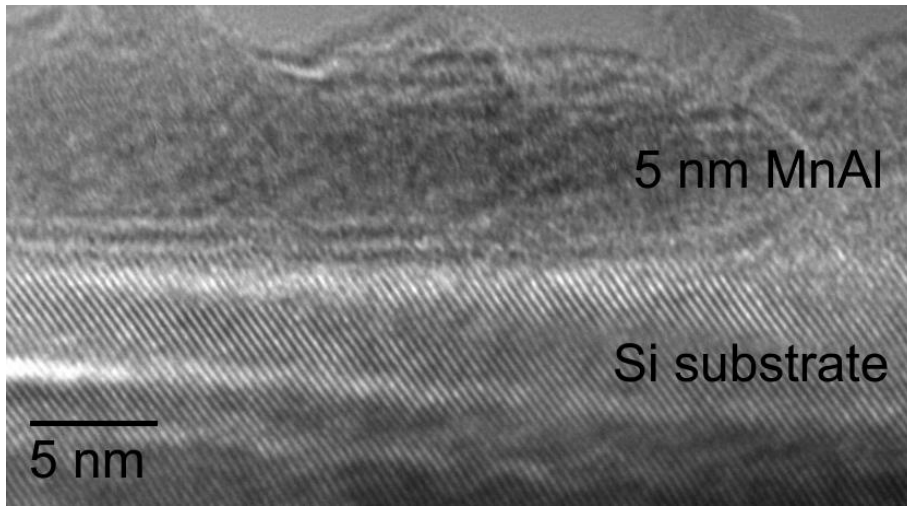


Figure 6-14 TEM cross-sectional image of the natively oxidized Si/MnAl (5 nm) film deposited at room temperature and annealed with RTA at  $T_a = 650$  °C.

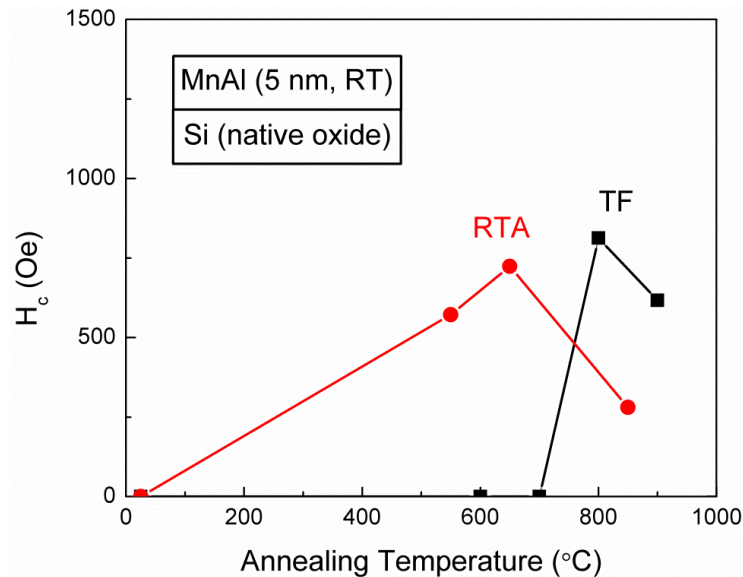


Figure 6-15 Annealing temperature dependence of out-of-plane coercivity  $H_c$  of natively oxidized Si/MnAl (5 nm) films deposited at room temperature and annealed with rapid thermal annealing (RTA) or tube furnace (TF).

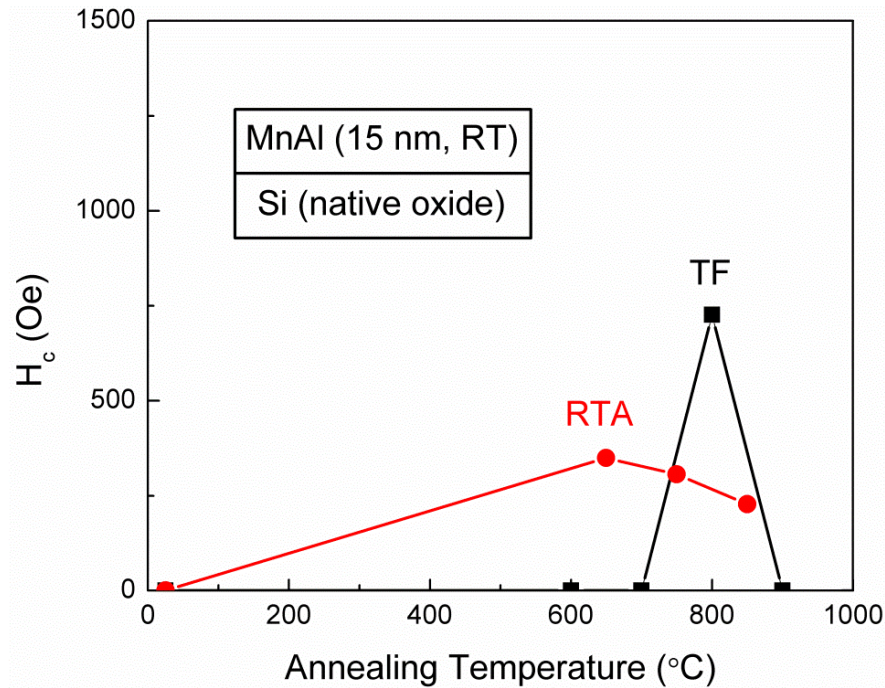


Figure 6-16 Annealing temperature dependence of out-of-plane coercivity  $H_c$  of natively oxidized Si/MnAl (15 nm) films deposited at room temperature and annealed with rapid thermal annealing (RTA) or tube furnace (TF).

Next, the effect of removing the native oxide by dipping samples in buffered HF was investigated, and the data are shown in FIG. 6-17. Both RTA and TF-annealed samples reached a higher maximum PMA than samples untreated with buffered HF, though the optimal annealing temperature was also increased. This is believed to be due to the nucleation mechanism for ordering within the film. Whereas in the non-HF cleaned samples the ordering could nucleate in local regions with atomic configurations already favorable for ordering, nucleation in HF cleaned samples is more likely to occur at the Si/MnAl interface. Higher temperatures are therefore necessary to propagate the ordering throughout the film, but ultimately result in higher overall PMA due to more coherent grains all growing off the same single crystal Si template.

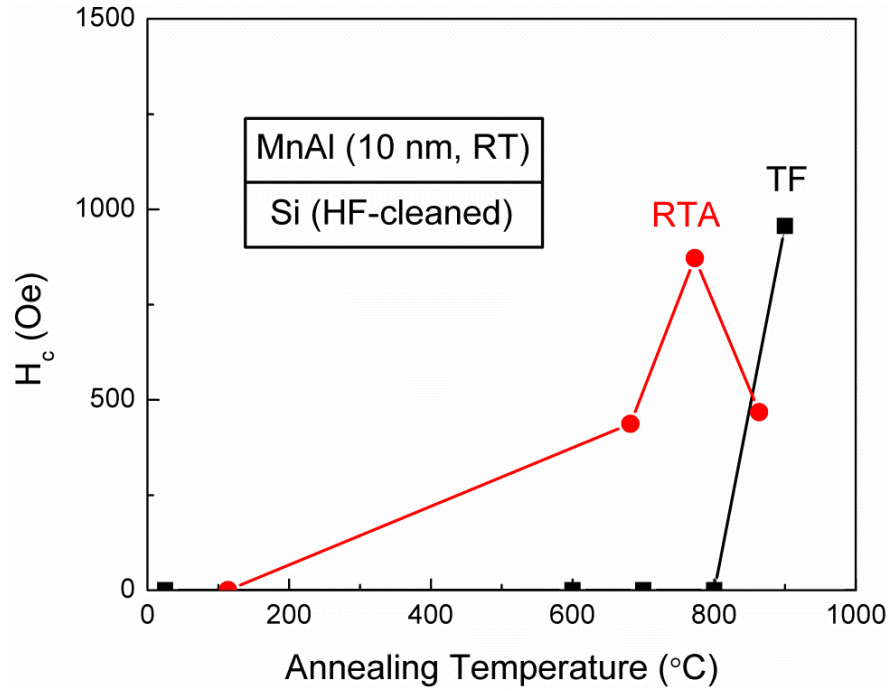


Figure 6-17 Annealing temperature dependence of out-of-plane coercivity  $H_c$  of buffer HF-cleaned Si/MnAl (10 nm) films deposited at room temperature and annealed with rapid thermal annealing (RTA) or tube furnace (TF).

TiN, which was used as an effective seed layer in Chapter 4, was inserted into the film stack. Samples of natively oxidized Si/TiN (10 nm)/MnAl (5) deposited at room temperature and  $T_s = 200$  °C were annealed with RTA and tube furnace, with the results displayed in FIG. 6-18 and FIG. 6-19, respectively. Samples deposited at  $T_s = 200$  °C showed significant PMA at lower temperatures than those deposited at room temperature, but also reached a lower maximum PMA. Here, too, the nucleation model provides a reasonable explanation. High deposition temperatures creates random local regions throughout the MnAl film favorable for ordering. With the small amount of thermal energy provided by moderate annealing temperatures, the phase transition is driven to order the films. Nevertheless, since the initial deposition was not templated to a textured underlayer, the favorable nucleation sites are numerous and randomly positioned, and the resulting overall PMA is low. On the other hand, films deposited at lower temperature have fewer, if any, favorable nucleation sites. A higher temperature is therefore required to nucleate ordering at the TiN/MnAl interface and propagate the phase transition through the material. However, the nucleation sites are fewer in number and more uniform in position, resulting in higher overall PMA of the films. This theory is supported by the TEM cross-sectional image shown in FIG. 6-20, where one can see the TiN textured regions formed around the TiN/MnAl interface rather than the Si/TiN interface. A closeup, displayed in FIG. 6-21, shows coherent lattice fringes extending from the MnAl into the TiN (upper left of the image), and none between the Si and TiN (lower right of the image). Once again, films appear smoother than those studied in Chapter 4, Chapter 5, and Section 6.2 but unfortunately demonstrate significantly reduced PMA.

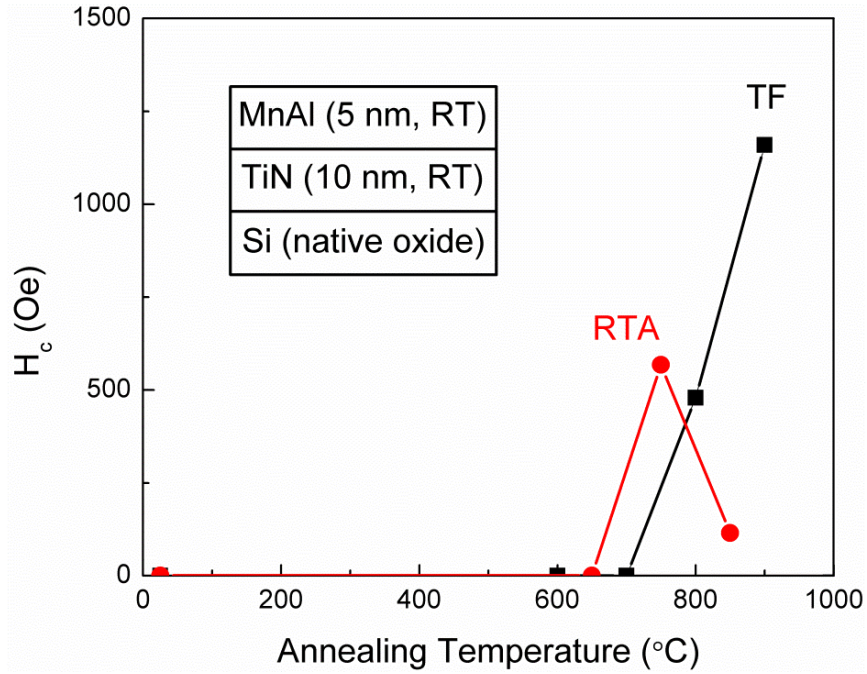


Figure 6-18 Annealing temperature dependence of out-of-plane coercivity  $H_c$  of natively oxidized Si/TiN (10 nm)/MnAl (5) films deposited at room temperature and annealed with rapid thermal annealing (RTA) or tube furnace (TF).

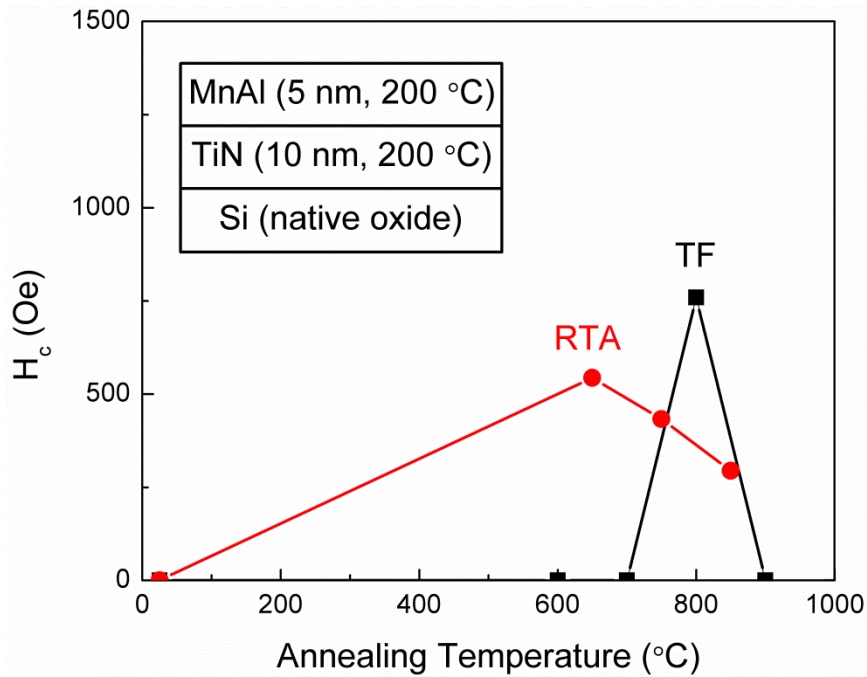


Figure 6-19 Annealing temperature dependence of out-of-plane coercivity  $H_c$  of natively oxidized Si/TiN (10 nm)/MnAl (5) films deposited at  $T_s = 200$  °C and annealed with rapid thermal annealing (RTA) or tube furnace (TF).

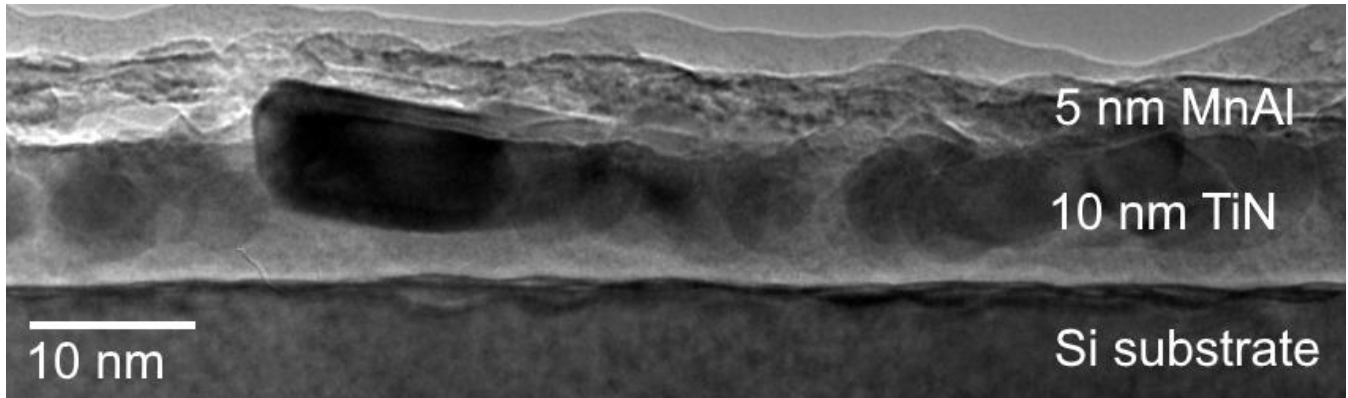


Figure 6-20 TEM cross-sectional image of the natively oxidized Si/TiN (10 nm)/MnAl (5) film stack deposited at room temperature and annealed with tube furnace at  $T_a = 900$  °C.

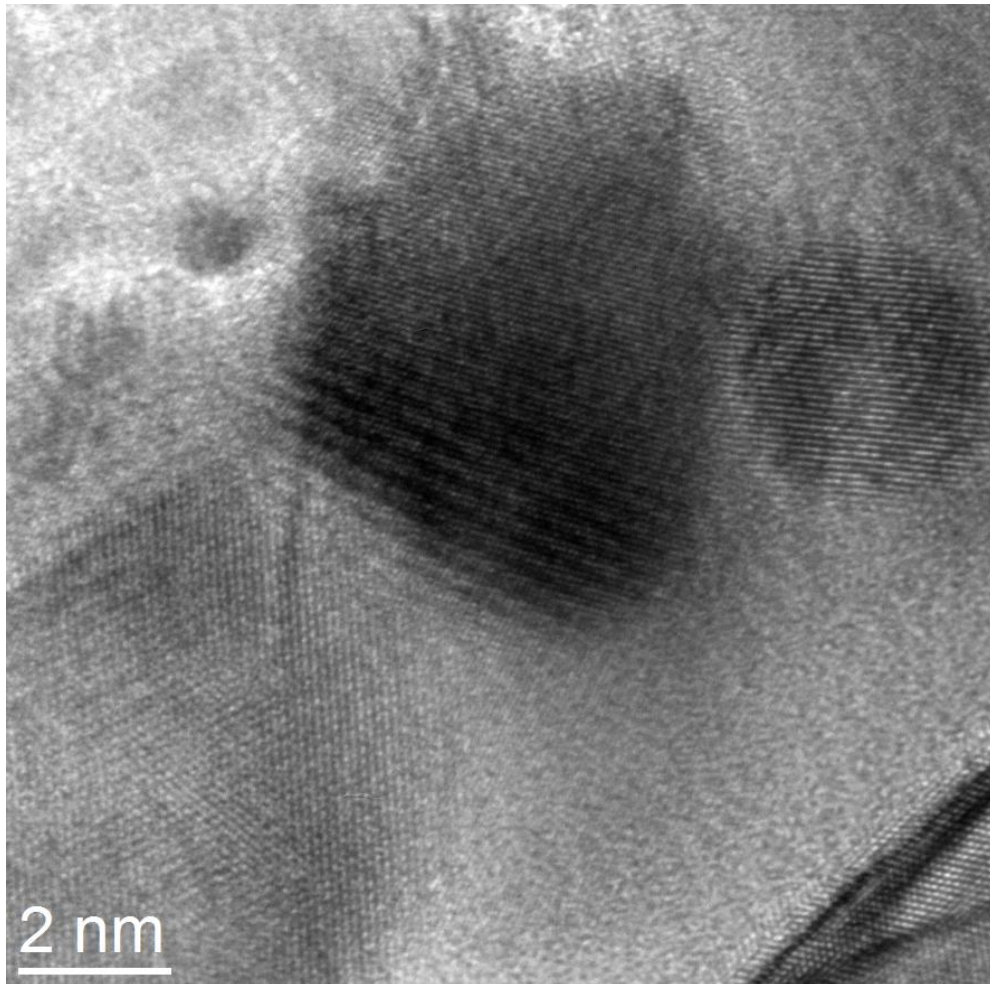


Figure 6-21 TEM cross-sectional image of TiN in natively oxidized Si/TiN (10 nm)/MnAl (5) film stack deposited at room temperature and annealed with tube furnace at  $T_a = 900$  °C.

A similar effect is seen even with the removal of native oxide. The data for buffer HF-cleaned Si/TiN (10 nm)/MnAl (10) samples deposited at  $T_s = 200$  °C are shown in FIG. 6-22, and the data for the same film stacks deposited at  $T_s = 300$  °C are shown in FIG. 6-23. As before, the samples deposited at higher *in situ* temperature showed significant PMA at lower annealing temperatures, but reached lower maximum PMA than those deposited at lower temperature.

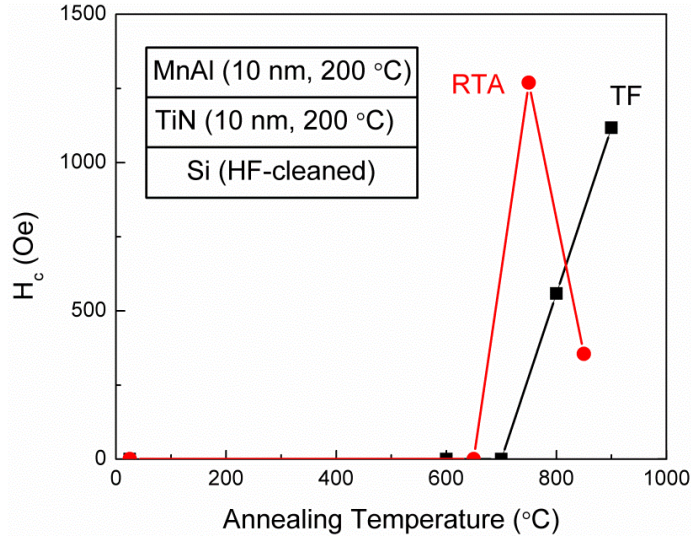


Figure 6-22 Annealing temperature dependence of  $H_c$  of buffer HF-cleaned Si/TiN (10 nm)/MnAl (10) films deposited at  $T_s = 200$  °C and annealed with RTA or tube furnace (TF).

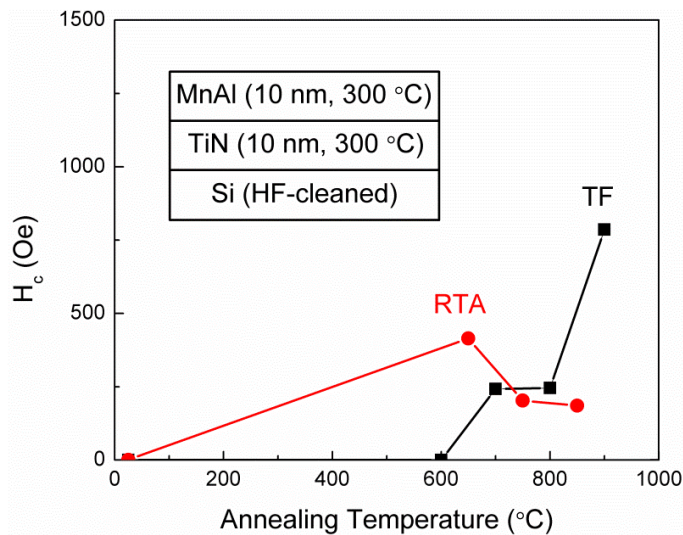


Figure 6-23 Annealing temperature dependence of  $H_c$  of buffer HF-cleaned Si/TiN (10 nm)/MnAl (10) films deposited at  $T_s = 300$  °C and annealed with RTA or tube furnace (TF).

Finally, the values of maximum  $H_c$  were collected and plotted in FIG. 6-24. In general, rapid thermal annealing was able to produce PMA in films at lower temperatures, but tube furnace annealing produced films with higher maximum PMA. This can also be explained by the nucleation model discussed previously. Since tube furnace annealing heats the substrate from the bottom, thermal energy travels upward from the underlayers into the MnAl film. The ordered regions are therefore nucleated at the underlayer/MnAl interface and produce higher PMA as a result of this shared templating. Meanwhile, RTA involves heat traveling from the film surface downwards. In this case, nucleation sites are more likely to have differing orientations, resulting in less coherent ordered regions and reduced overall PMA. The notable outlier is the RTA-annealed buffer HF-cleaned Si/TiN (10 nm)/MnAl (10) film deposited at  $T_s = 200$  °C, which exhibited the highest PMA of all samples in the study. The stack structure is remarkably similar to the optimized buffer HF-cleaned Si substrate/TiN (10 nm)/MnAl (30)/Ta (5) sample examined in Chapter 5, though the previous sample was deposited at  $T_s = 400$  °C. It is possible that this stack structure deposited at  $T_s = 200$  °C results in just enough nucleation sites near the TiN/MnAl interface for templated ordering, but not so many throughout the film that the nucleation sites differ significantly in orientation.

Overall, samples annealed by RTA and tube furnace annealing were seen to have different optimal annealing temperatures and resulted in smoother films. However, the PMA of all annealed samples was much smaller (coercivity  $< 1.5$  kOe) than that of previously studied samples deposited with high *in situ* deposition temperature (8-12 kOe).

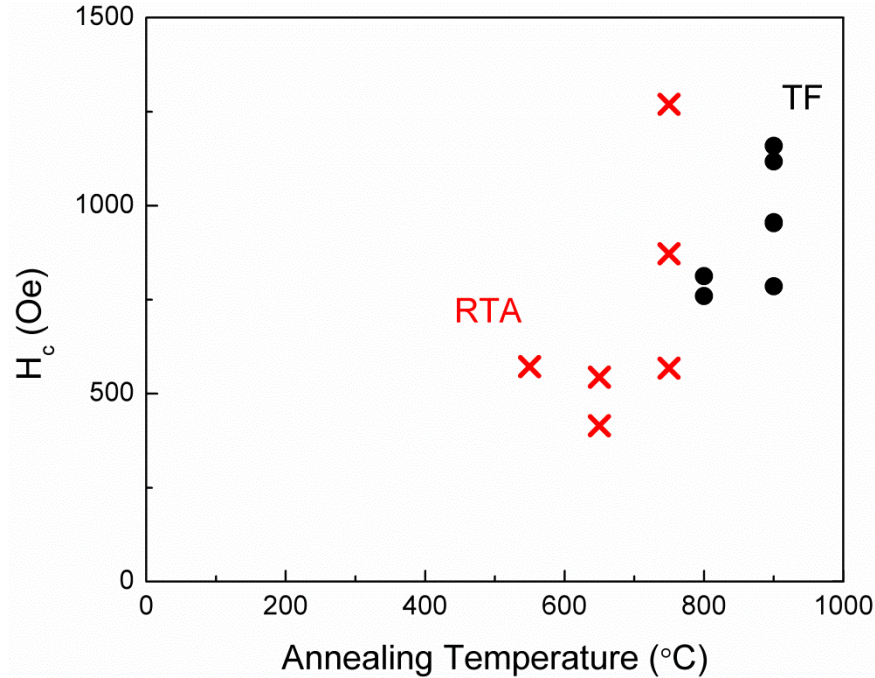


Figure 6-24 Maximum values of out-of-plane coercivity  $H_c$  for MnAl film stacks annealed at various temperatures with RTA (red crosses) and tube furnace (TF, black circles).

## 6.4. Summary

In this chapter, three main approaches to reducing the ordering temperature and surface roughness of  $L1_0$ -MnAl thin films were investigated: adding other materials to the MnAl film, using various underlayers in conjunction with these additions, and utilizing alternative post-annealing methods. Inspired by existing work on bulk, powder, and thick films of MnAl, the effects of introducing Ni, C, and  $\text{SiO}_x$  into MnAl thin films (Section 6.2) were investigated. MnAl:Ni films with 3 volume% Ni content deposited on TiN underlayers revealed that surface roughness increased dramatically below the ordering temperature. The results also confirmed the findings in Chapter 5 that surface roughness of MnAl-based films increases rapidly with thickness, and that keeping the MnAl free layer thin is advantageous for an MnAl-based MTJ structure. Using  $(\text{Mg}_{0.2}\text{Ti}_{0.8})\text{O}$  and CrRu underlayers did not improve either PMA or film

roughness. Introducing varying amounts of C into MnAl films resulted in more pronounced effects, with 1 volume% C showing increased PMA when the C was deposited first, which agreed well with existing studies [3]. The C in excess of the solubility limit (1.7 atomic%) appeared to diffuse to the grain edges, and an increase in C content beyond that limit degraded PMA. Adding any amount of SiO<sub>x</sub> to MnAl films severely reduced PMA.

Next, rapid thermal annealing (RTA) and tube furnace annealing were examined as post-annealing methods for achieving  $L1_0$ -ordering in MnAl thin films (Section 6.3). RTA was found to produce PMA in films at lower annealing temperatures than tube furnace annealing, but tube furnace annealing produced films with higher maximum PMA than RTA. This trend, as well as the observation that higher deposition temperatures actually resulted in lower maximum PMA, was attributed to nucleation theory of ordering. Lattice fringes and texture patterns seen in TEM images further supported the theory. The film stack with highest PMA produced in the study had a stack structure of buffer HF-cleaned Si/TiN (10 nm)/MnAl (10), remarkably similar to the film stack optimized in Chapter 5. Though the PMA values across all annealed samples were significantly lower than those of samples relying on high *in situ* deposition temperatures to achieve  $L1_0$ -ordering, the film roughness appeared to be lower as well. In this way, there is a clear tradeoff between high PMA and low surface roughness.

Overall, the studies discussed in this chapter showed that reducing the high surface roughness of MnAl-based films for MTJ development is a challenging task. None of the methods examined were able to reduce the ordering temperature without sacrificing PMA. Nevertheless, the results presented in this chapter reveal interesting tradeoffs between PMA and surface roughness and the theories presented may serve as a guide for future studies.

Thus far, the discussion has only entailed using the same single material for both the free and reference electrodes, and the material additions, underlayer systems, and annealing techniques studied in this chapter either did not reduce film roughness or resulted in reduced PMA of thin films. In the next chapter, MTJ stack structures employing heterogeneous material systems for top and bottom electrodes are studied, because it was thought they may have certain advantages. For example, it was thought that using an  $L1_0$ -MnAl-based material as the top free electrode and an alternative material as the bottom reference electrode may mitigate the roughness issues.

## 6.5. References

- [1] L. Pareti, F. Bolzoni, F. Leccabue, and A. E. Ermakov, "Magnetic anisotropy of MnAl and MnAlC permanent magnet materials," *J. Appl. Phys.*, vol. 59, no. 11, p. 3824, 1986.
- [2] Q. Zeng, I. Baker, J. B. Cui, and Z. C. Yan, "Structural and magnetic properties of nanostructured Mn–Al–C magnetic materials," *J. Magn. Magn. Mater.*, vol. 308, no. 2, pp. 214–226, Jan. 2007.
- [3] Z. W. Liu, C. Chen, Z. G. Zheng, B. H. Tan, and R. V. Ramanujan, "Phase transitions and hard magnetic properties for rapidly solidified MnAl alloys doped with C, B, and rare earth elements," *J. Mater. Sci.*, vol. 47, no. 5, pp. 2333–2338, Mar. 2012.
- [4] J. Z. Wei, Z. G. Song, Y. B. Yang, S. Q. Liu, H. L. Du, J. Z. Han, D. Zhou, C. S. Wang, Y. C. Yang, A. Franz, D. Többens, and J. B. Yang, " $\tau$ -MnAl with high coercivity and saturation magnetization," *AIP Adv.*, vol. 4, no. 12, p. 127113, Dec. 2014.
- [5] M. Matsumoto, A. Morisako, and N. Kohshiro, "Crystal Structure and Magnetic Properties of Mn-Al-Ni Ferromagnetic Films," *Magn. Jpn. IEEE Transl. J. On*, vol. 6, no. 2, pp. 134–140, 1991.
- [6] H. X. Wang, P. Z. Si, W. Jiang, J. G. Lee, C. J. Choi, J. J. Liu, Q. Wu, M. Zhong, and H. L. Ge, "Structural Stabilizing Effect of Zn Substitution on MnAl and Its Magnetic Properties," *Open J. Microphys.*, vol. 1, no. 2, pp. 19–22, 2011.
- [7] C. S. Kim, D. Choi, S. Chung, A. Wise, Y. Y. Dang, and M. H. Kryder, "Surface roughness and magnetic properties of  $L1_0$  FePt films on MgO/CrRu/TiN," *J. Appl. Phys.*, vol. 112, no. 2, p. 23907, 2012.
- [8] S. D. Granz, "Granular  $L1_0$  FePt:X (001) Thin Films for Heat Assisted Magnetic Recording," Ph.D. Dissertation, Carnegie Mellon University, Pittsburgh, PA, 2012.
- [9] S. D. Granz and M. H. Kryder, "Intergranular Exchange Coupling in FePt:X:FePt (X=B, C, SiO<sub>x</sub>, Cr and TaO<sub>x</sub>) Thin Films for Heat Assisted Magnetic Recording," *IEEE Trans. Magn.*, vol. 48, no. 11, pp. 2746–2748, Nov. 2012.
- [10] K. Yano, V. Nandwana, N. Poudyal, C.-B. Rong, and J. P. Liu, "Rapid thermal annealing of FePt nanoparticles," *J. Appl. Phys.*, vol. 104, no. 1, p. 13918, 2008.
- [11] K. Aimuta, K. Nishimura, S. Hashi, and M. Inoue, "Fabrication of  $L1_0$ -FePt thin films by rapid thermal annealing," *IEEE Trans. Magn.*, vol. 41, no. 10, pp. 3898–3900, Oct. 2005.
- [12] J.-W. Liao, K.-F. Huang, L.-W. Wang, W.-C. Tsai, W.-C. Wen, C.-C. Chiang, H.-J. Lin, F.-H. Chang, and C.-H. Lai, "Highly (001)-oriented thin continuous  $L1_0$  FePt film by introducing an FeO<sub>x</sub> cap layer," *Appl. Phys. Lett.*, vol. 102, no. 6, p. 62420, 2013.

# Chapter 7

## Exchange Coupled $L1_0$ -Ordered Magnetic Thin Films

### 7.1. Introduction

In Chapters 4, 5, and 6 the use of  $L1_0$ -MnAl-based thin films as both electrodes in MTJs was investigated. However, heterogeneous stack structures may confer benefits for MTJs. For example, an electrode consisting of two exchange coupled magnetic film layers, one with relatively high PMA and high damping and the other with relatively low PMA and low damping, could demonstrate both overall high effective PMA and low effective damping. Or, using a high anisotropy material as the reference layer and a low anisotropy material as the free layer could result in an MTJ with both high thermal stability and low critical switching current.

In this chapter, exchange coupled  $L1_0$ -FePt/MnAl heterogeneous structures (Section 7.2) and high- and low-anisotropy thin films separated by a thin barrier (7.3) are studied.

### 7.2. $L1_0$ -FePt/MnAl Heterogeneous Structures

As discussed in Section 2.5, the critical switching current of an MTJ varies directly with the Gilbert damping parameter  $\alpha$ . This observation motivated the development of high-PMA, low-damping  $L1_0$ -MnAl-based thin films discussed in Chapters 4, 5, and 6. However, some research suggests that, since electrons crossing the tunnel barrier into a magnetic layer impart their angular momentum within 1-2 nm of entering the magnetic layer, STT is essentially a surface process [1]. If so, using exchange-coupled heterogeneous structures of two different

materials, one with relatively high PMA and high damping and the other with relatively low PMA and low damping, could demonstrate both overall high effective PMA and low effective damping. In this section, this concept is pursued by investigating  $L1_0$ -FePt/MnAl heterogeneous structures.

### 7.2.1 Experimental Details

The substrates used in this study were 1” (100) Si wafers with native oxide. Films were deposited in the Custom 5-Target Sputtering System #2 at base pressures below  $2 \times 10^{-7}$  Torr. Film stacks had the structure Si substrate/MgO (20 nm)/FePt (10)/MnAl (5-50). First, the substrate was heated *in situ* to 425 °C, which helped enhance the MgO (001) texture and promote  $L1_0$ -ordered growth of the subsequent FePt. A 20 nm MgO seed layer was then RF sputtered. Next, 10 nm of FePt was RF sputtered, holding the substrate at 425 °C. Finally, the substrate was held at or cooled to the MnAl deposition temperature (300-425 °C), at which point a 5-50 nm MnAl film was DC magnetron sputtered from a vacuum hot-pressed  $Mn_{48}Al_{52}$  target. Magnetic properties of the structures were investigated using PPMS.

### 7.2.2 Results and Discussion

A film stack of Si substrate/MgO (20 nm)/FePt (10), without MnAl, was first fabricated and characterized as a baseline comparison against heterogeneous film stacks. The corresponding magnetic hysteresis loops are shown in FIG. 7-1. The results show high PMA, with coercivity of nearly 20 kOe and saturation magnetization around 1000 emu/cm<sup>3</sup>. The closed in-plane loop indicates good out-of-plane ordering, with very little in-plane component.

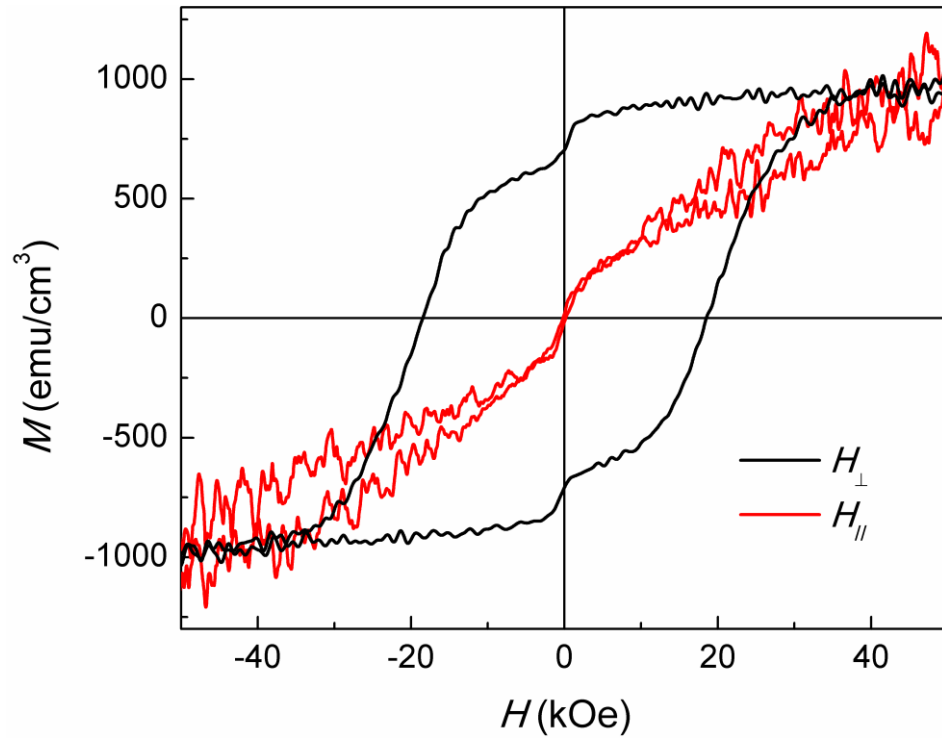


Figure 7-1 Out-of-plane/in-plane magnetic hysteresis loops of the baseline Si substrate/MgO (20 nm)/FePt (10) film stack.

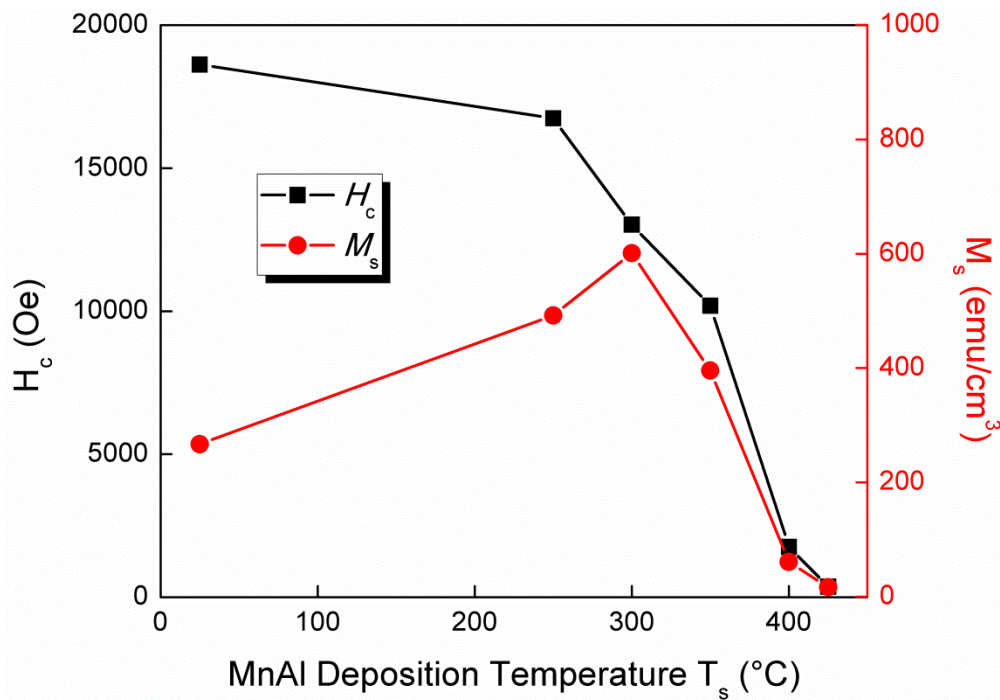


Figure 7-2 MnAl sputtering temperature dependence of out-of-plane coercivity  $H_c$  and saturation magnetization  $M_s$  of Si Substrate/MgO (20 nm)/FePt (10)/MnAl (30) film stacks.

The effects of *in situ* sputtering temperature  $T_s$  of MnAl on out-of-plane coercivity  $H_c$  and saturation magnetization  $M_s$  of Si Substrate/MgO (20 nm)/FePt (10)/MnAl (30) film stacks were studied and the data are plotted in FIG. 7-2. When MnAl is deposited at room temperature, the coercivity of the film stack is similar to that of the baseline FePt film, and the effective saturation magnetization of around  $270 \text{ emu/cm}^3$  is approximately one quarter that of the baseline FePt film. Considering the FePt thickness of 10 nm represents one quarter of the total FePt/MnAl film volume, these numbers strongly suggest the measured magnetic behavior can be entirely attributed to the FePt film. Indeed, given the previous results from Chapters 4 and 5, no significant  $L1_0$ -ordering is expected in MnAl when deposited at room temperature. As the MnAl deposition temperature is increased,  $H_c$  decreases and  $M_s$  increases. The increase in  $M_s$  can be explained by the presence of  $L1_0$ -MnAl, while the reduction in  $H_c$  is due to exchange coupling between the lower-PMA MnAl film and the higher-PMA FePt film. Above  $300 \text{ }^\circ\text{C}$ ,  $M_s$  decreases dramatically. This may be due to interdiffusion between the FePt and MnAl layers, which also contributes to  $H_c$  vanishing. Further evidence of interdiffusion can be seen from Si Substrate/MgO (20 nm)/FePt (10)/MnAl (0-50) film stacks, whose data are shown in FIG. 7-3.

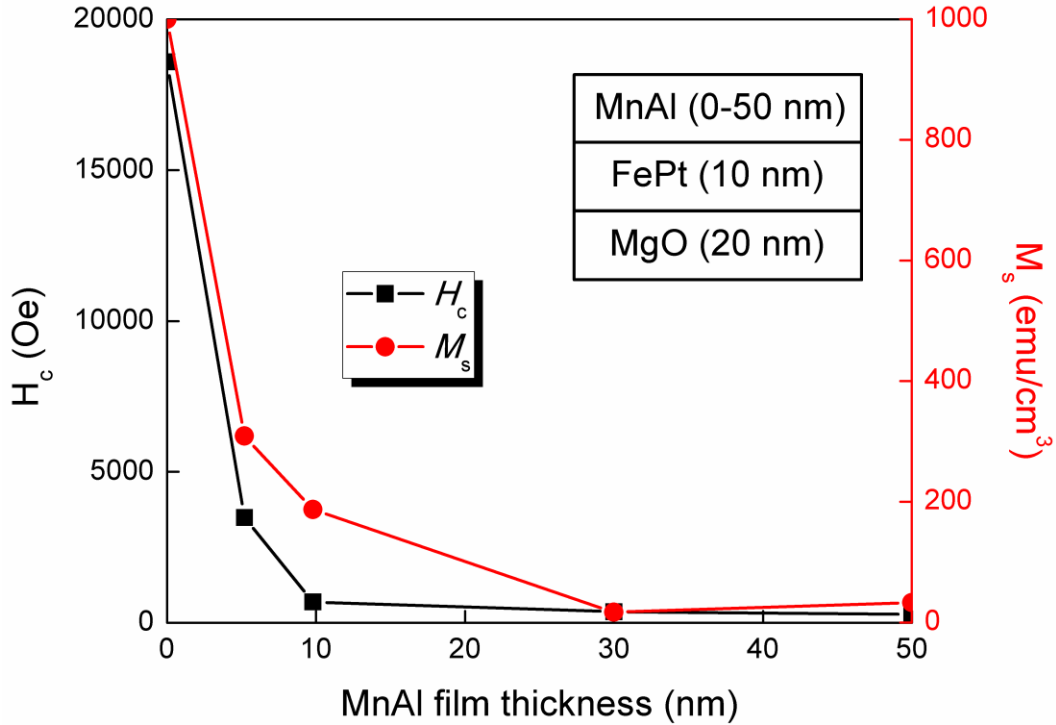


Figure 7-3 MnAl thickness dependence of out-of-plane coercivity  $H_c$  and saturation magnetization  $M_s$  of Si Substrate/MgO (20 nm)/FePt (10 nm)/MnAl (0-50 nm) film stacks deposited at 425 °C.

In this study, all films were deposited at 425 °C. Only the MnAl film thickness was varied. The results indicate a marked dropoff in both  $H_c$  and  $M_s$ , which is best explained by interdiffusion between FePt and MnAl. The decrease in both  $H_c$  and  $M_s$  beyond  $T_s = 300$  °C seen in FIG. 7-2 are therefore attributed primarily to interdiffusion. While the results from Chapters 4, 5, and 6 indicated an optimal MnAl deposition temperature of 400-500 °C for maximum PMA, the interdiffusion seen here limits MnAl deposition to 300 °C. This poses significant constraints on the development of FePt/MnAl exchange coupled film stacks.

### 7.3. High- and Low-Anisotropy Thin Films Separated by a Thin Barrier

Another potential method of producing MTJs with both high thermal stability and low critical switching current is by taking advantage of interlayer exchange coupling across a tunnel barrier. With appropriate cross-barrier exchange coupling, a low-damping, low anisotropy free layer can be somewhat magnetically pinned to increase thermal stability. This is the equivalent of an externally applied field as discussed in Section 2.5. However, the exchange coupling behavior between the reference and free layer is not well understood. Prior work on interlayer exchange coupling between thin films [2], [3] revealed some dependency of exchange coupling energy on the material and thickness of the barrier layer. Granz also noted that temperature may have a significant impact on exchange coupling [4]. Characterizing these dependencies is useful not only for understanding MTJ behavior at elevated operating temperatures, but also has applications in accurately modeling intergranular exchange in heat-assisted-magnetic-recording (HAMR) media, as illustrated in FIG. 7-4.

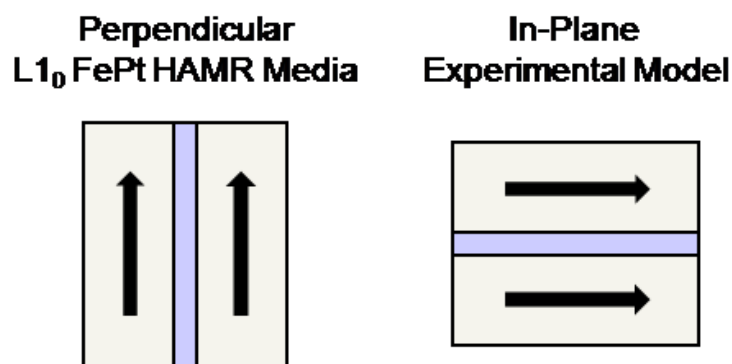


Figure 7-4 Experimental model for intergranular region of perpendicular HAMR media using in-plane film stack structure.

In this section, the effects of interlayer exchange coupling between high- and low-anisotropy  $L1_0$ -ordered magnetic thin films were experimentally investigated via FePt:X:FePt (X=TaO<sub>x</sub>, SiO<sub>x</sub>, Cr) sputtered thin film stacks. FePt was selected given the existing techniques for depositing both hard (high in-plane anisotropy) and soft (low in-plane anisotropy) FePt with low surface roughness to ensure a continuous barrier layer. TaO<sub>x</sub> was chosen for its effectiveness in decoupling exchange, TaO<sub>x</sub> and SiO<sub>x</sub> for their ability to promote columnar growth of FePt in perpendicular recording media, and Cr for its ability to promote  $L1_0$ -ordering, as a comparison to conducting barrier materials. Film stacks were deposited on 20 nm of MgO, which promotes  $L1_0$ -ordering in the subsequent FePt films, and a Ta capping layer was sputtered on top of the film stack to stabilize the structure against corrosion at high temperatures. Magnetic hysteresis was measured for varying barrier layer thicknesses (0.5 nm-1.5 nm) at varying temperatures (300 K-700 K). Exchange coupling energies were calculated using the reversal field, saturation magnetization, and coercivity. The work discussed in this section has been previously published in reference [5].

### 7.3.1 Experimental Details

The substrates used in this study were 1" (100) Si wafers with native oxide. All films were deposited in the Custom 5-Target Sputtering System #2 at base pressures below  $2 \times 10^{-7}$  Torr and Ar gas pressure of 25 mTorr. Film stacks followed the structure: Si substrate/MgO (20 nm)/hard FePt (10)/barrier material (0.5-1.5)/soft FePt (9.4)/Ta (5). Cr films were deposited using DC sputtering; all other films were deposited via RF sputtering. Since deposited film composition may differ from target composition, the films are referred to as MgO<sub>x</sub>, TaO<sub>x</sub>, and SiO<sub>x</sub>. The 20 nm MgO<sub>x</sub> (002) texture layer was sputtered at 200 W and room temperature. The

10 nm hard FePt layer was sputtered at 50 W and 425 °C. The barrier layer was varied from 0.5 nm to 1.5 nm in thickness and was deposited at 10 W (Cr), 50 W (TaO<sub>x</sub>), and 200 W (SiO<sub>x</sub>) at room temperature. The 9.4 nm soft FePt layer was deposited at 50 W and room temperature. The 5 nm Ta capping layer was DC sputtered at base pressures below  $5 \times 10^{-7}$  Torr, Ar gas pressure of 2.5 mTorr, sputtering power of 50 W, and at room temperature. Texture, microstructure, and magnetic properties of the film stacks were investigated using XRD, TEM, AGFM, and PPMS.

### 7.3.2 Results and Discussion

Both high- and low-anisotropy FePt layers demonstrated low surface roughness at their respective barrier interfaces, allowing the barrier material to form a thin, continuous layer, as seen in the TEM cross-sectional image of a Si substrate/MgO (20 nm)/FePt (10)/Cr (1)/FePt (9.4)/Ta (5) film stack, shown in FIG. 7-5. When deposited at 25 mTorr Ar pressure, 50 W DC sputtering power, and 425 °C substrate temperature, the 10 nm hard FePt layer demonstrated significant in-plane ordering, which can be seen from the in-plane  $\theta/2\theta$  XRD pattern and in-plane versus out-of-plane magnetic hysteresis loops shown in FIG. 7-6. The deconvoluted integrated peak intensity ratio  $I_{001}/I_{002} = 1.558$  indicates significant ordering, while the reduced coercive field  $H_c$  and shearing of the out-of-plane hysteresis loop as compared to the in-plane loop reveal primarily in-plane anisotropy, with saturation magnetization of 820 emu/cm<sup>3</sup> and in-plane coercivity of 4.6 kOe at room temperature. The observed in-plane FePt growth is believed to be promoted by the MgO seed layer's rough interface and poor texture. The rough interface between MgO and hard FePt layers seen in FIG. 7-5 and the weak MgO (002) and FePt (111) peaks in the XRD pattern together suggest the FePt grows at various angles, resulting in both in-plane and out-of-plane anisotropy.

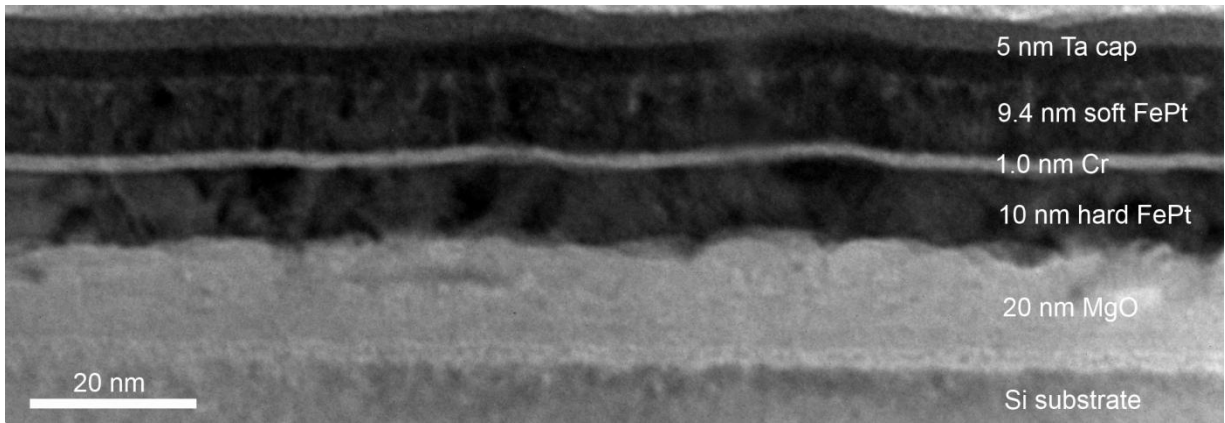


Figure 7-5 TEM cross-sectional image of Si substrate/FePt (10 nm)/Cr (1)/FePt (9.4)/Ta (5) film stack.

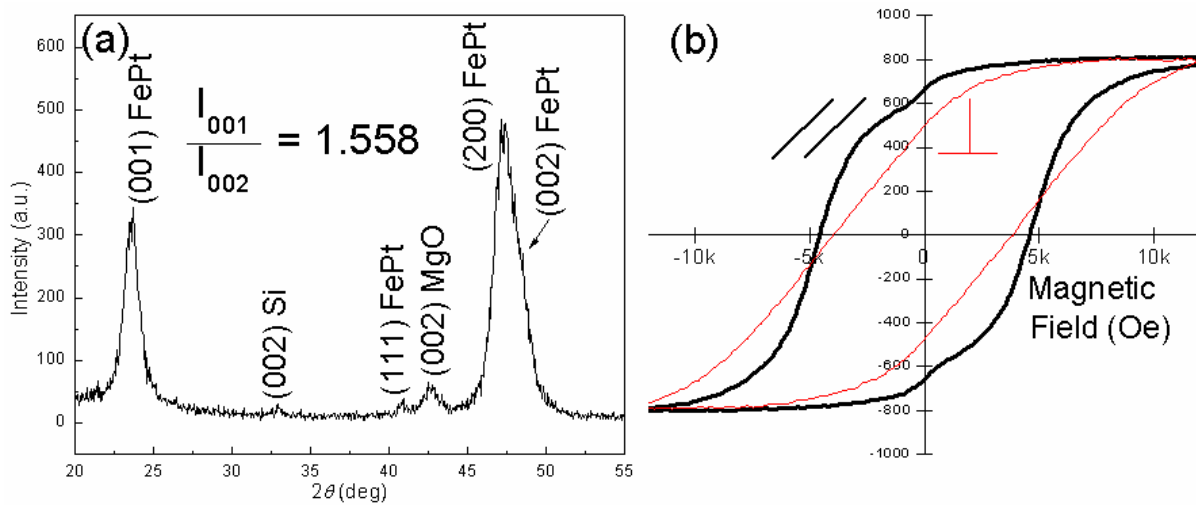


Figure 7-6 (a) In-plane  $\theta/2\theta$  XRD pattern and (b) In-plane (thick, black) versus out-of-plane (thin, red) magnetic hysteresis loops for hard FePt (10 nm)/MgO (20 nm).

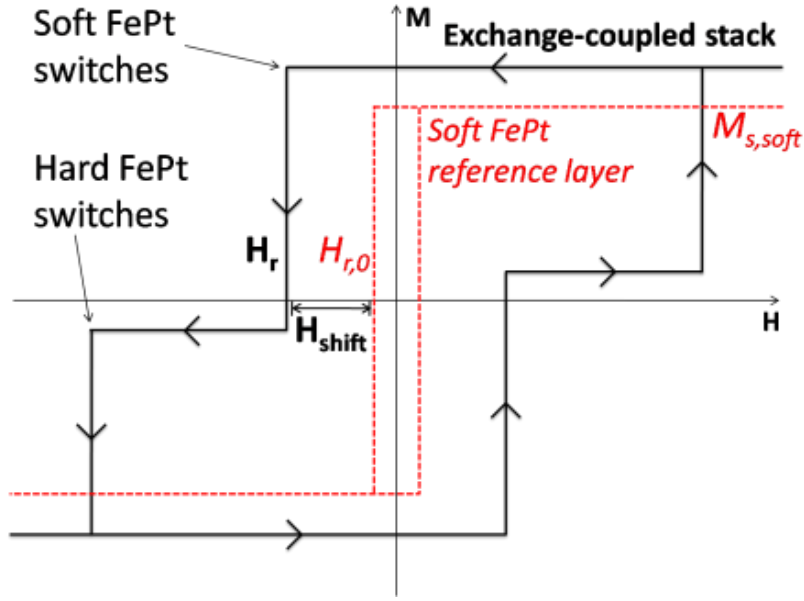


Figure 7-7 Idealized in-plane magnetic hysteresis loop showing shift in reversal field  $H_{\text{shift}} = H_r - H_{r,0}$ .

To determine the exchange coupling energy, the shift in reversal field of the soft FePt layer as a result of exchange coupling was calculated, as illustrated in FIG. 7-7. The hysteresis of a single layer of 9.4 nm soft FePt film deposited on 20 nm MgO<sub>x</sub> (002) was measured at corresponding temperatures as the reference layer; the extracted saturation magnetization  $M_{s,\text{soft}}$  and in-plane coercivity are shown in FIG. 7-8(a). The room temperature hysteresis loop of the reference layer is shown in FIG. 7-8(b), with saturation magnetization of 800 emu/cm<sup>3</sup> and in-plane coercivity of 29 Oe. The thicknesses of the hard (10 nm) and soft (9.4 nm) FePt layers were selected to facilitate extraction of the reversal field inflection point from the M/H loops. In this way, the interlayer exchange coupling energy at temperature  $T$  was calculated according to [2], [3]

$$E_c(T) = H_{\text{shift}}(T) M_{s,\text{soft}}(T) d_{\text{soft}} = [H_r(T) - H_{r,0}(T)] M_{s,\text{soft}}(T) d_{\text{soft}}$$

Equation 7-1

where  $H_r$  is the reversal field with exchange coupling,  $H_{r,0}$  is the reversal field (coercivity) of the soft FePt layer without exchange coupling,  $M_{s,\text{soft}}$  is the saturation magnetization of the soft FePt layer, and  $d_{\text{soft}}$  is the thickness of the soft FePt layer (9.4 nm). The measurements and calculations were performed at 50 K temperature increments from room temperature (300 K) to HAMR operating temperatures (700 K). The magnetic hysteresis loops of a film stack with 1.0 nm Cr barrier layer at various temperatures are shown in FIG. 7-9. Film stacks with TaO<sub>x</sub> and SiO<sub>x</sub> as barrier layer materials showed similar behavior, shown in FIG. 7-10 and 7-11, respectively.

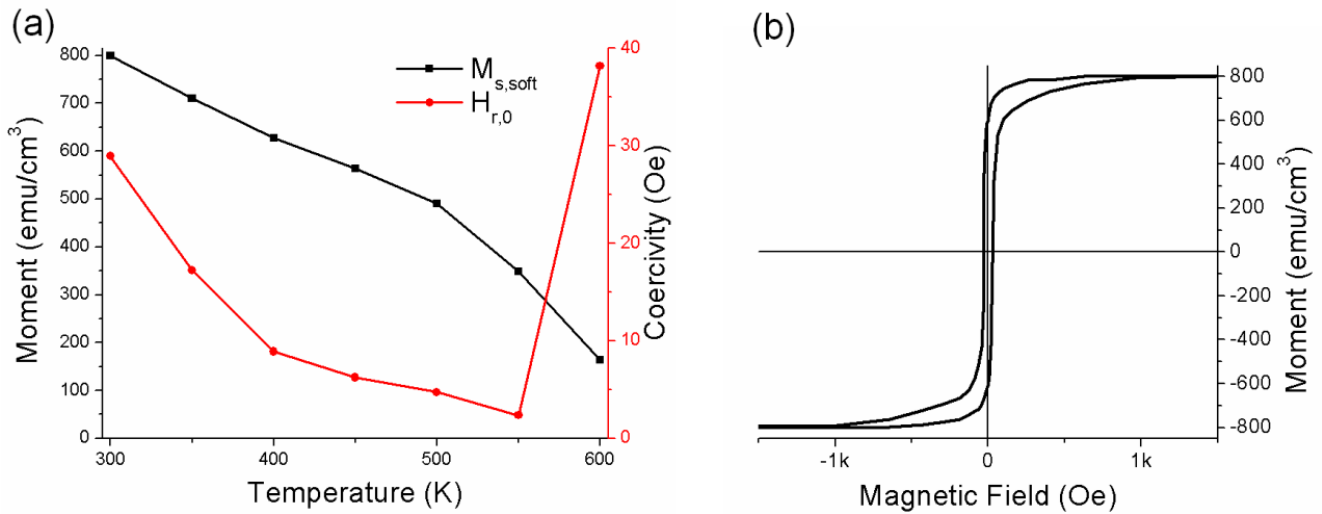


Figure 7-8 (a) In-plane measured temperature dependence of saturation magnetization and coercivity and (b) In-plane room temperature magnetic hysteresis loop for Si substrate/MgO (20 nm)/soft FePt (9.4) film stack.

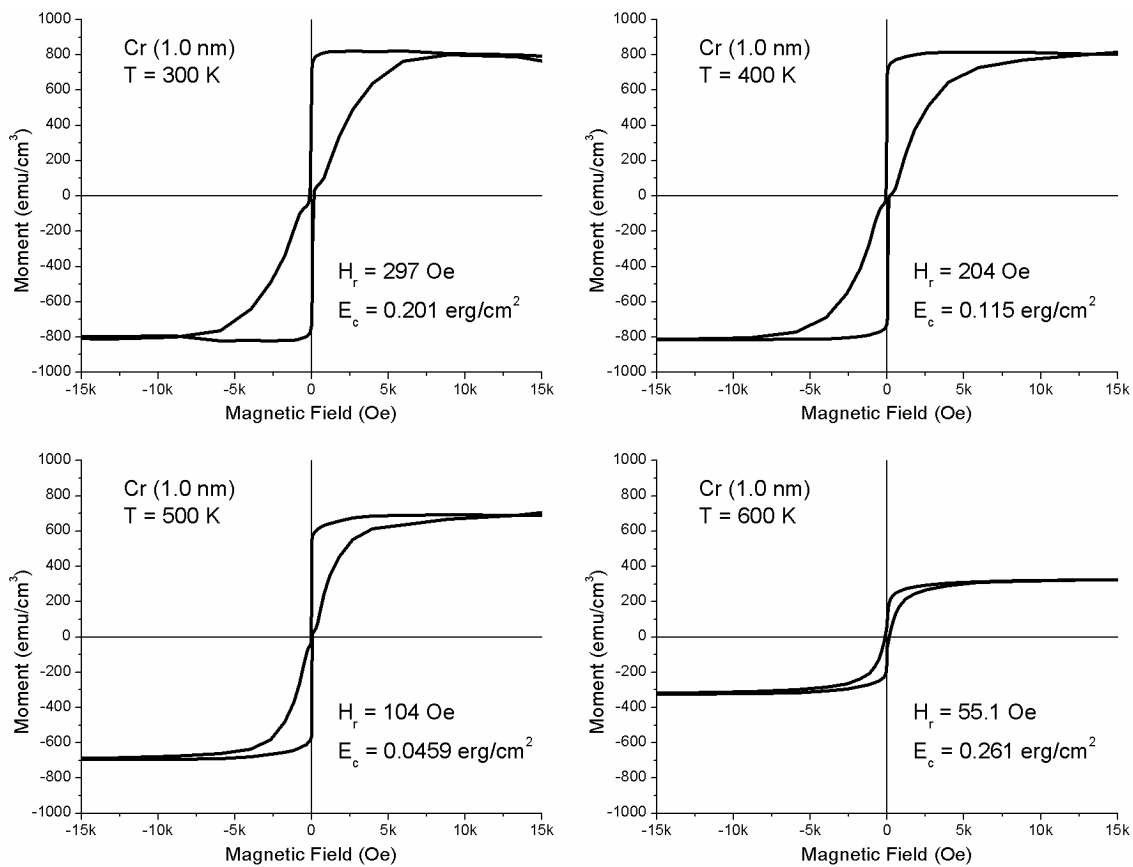


Figure 7-9 In-plane magnetic hysteresis loops for film stack with 1.0 nm Cr barrier layer at various temperatures.

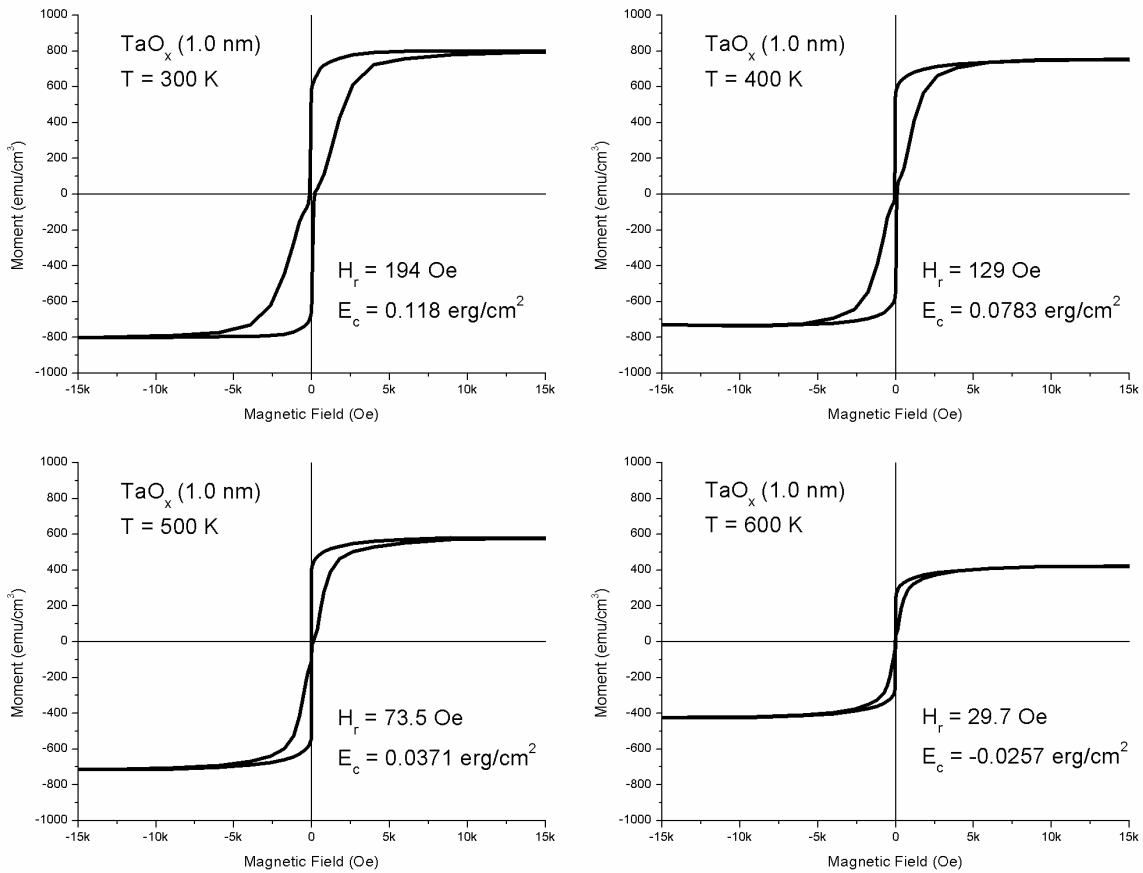


Figure 7-10 In-plane magnetic hysteresis loops for film stack with 1.0 nm TaO<sub>x</sub> barrier layer at various temperatures.

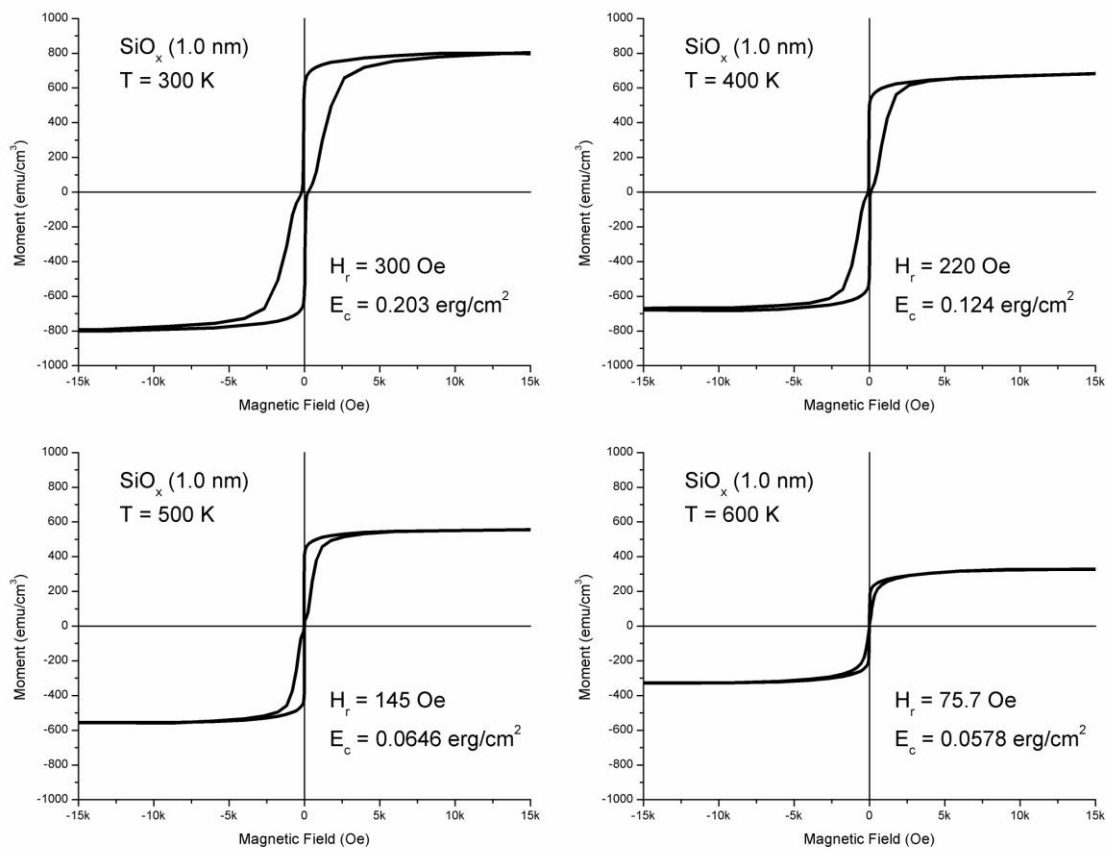


Figure 7-11 In-plane magnetic hysteresis loops for film stack with 1.0 nm SiO<sub>x</sub> barrier layer at various temperatures.

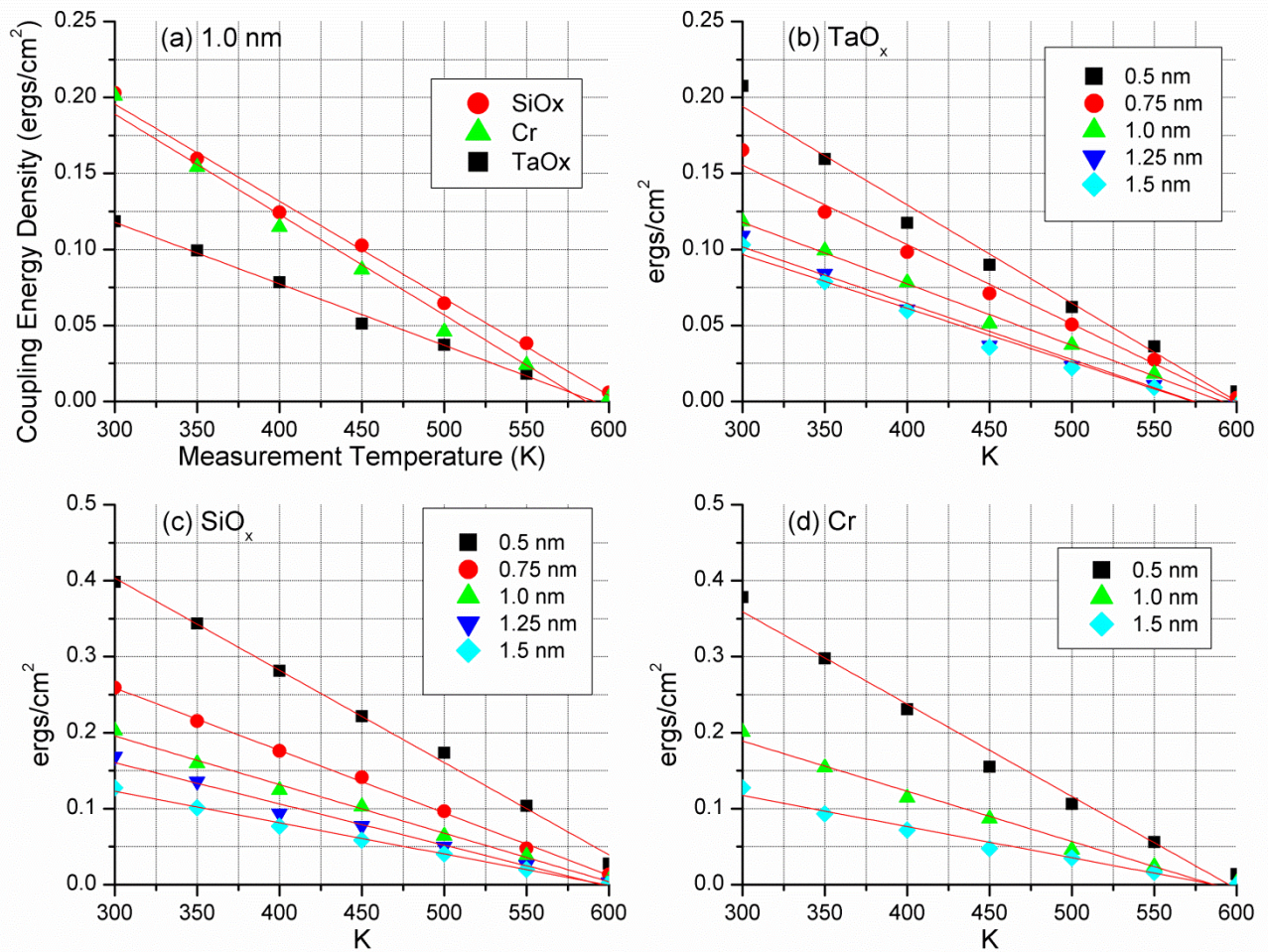


Figure 7-12 Exchange coupling energy density vs. measurement temperature for (a) 1.0 nm barrier layer, (b)  $\text{TaO}_x$ , (c)  $\text{SiO}_x$ , and (d) Cr.

The effects of temperature on interlayer exchange coupling energy density were investigated for  $\text{TaO}_x$ ,  $\text{SiO}_x$ , and Cr barrier layers of thicknesses ranging from 0.5 nm to 1.5 nm at temperatures ranging from 300 K to 700 K and are plotted in FIG. 7-12. The soft FePt layer began to switch at applied fields of 30-50 Oe, which corresponds well with the coercivity of the reference soft FePt on MgO, suggesting similar behavior between the reference soft FePt and the soft FePt in the barrier film stack. The interlayer exchange coupling was observed to be well-behaved, decreasing linearly with increasing temperature for each barrier material to 600 K. The

room temperature critical thicknesses for exchange decoupling, defined to be when exchange coupling energy equals  $0.2 \text{ ergs/cm}^2$  [2], were 0.5 nm for  $\text{TaO}_x$ , 1.0 nm for  $\text{SiO}_x$ , and 1.0 nm for Cr, which agree well with previous results [3]. As shown in FIG. 7-12(a),  $\text{TaO}_x$  was significantly more effective as an exchange breaking layer than either  $\text{SiO}_x$  or Cr, both of which demonstrated similar decoupling behavior. Increasing barrier thickness produced diminishing decoupling effect improvements, shown in FIG. 7-13, and exchange coupling invariably became negligible near 600 K, as seen in FIG. 7-12(b), (c), and (d), though this may partly be due to possible annealing effects, discussed later. While the disappearance of exchange coupling as the temperature approaches the Curie temperature agrees well with magnetic theory, the explanation for the linear dependence is less apparent. If the saturation magnetization varies as the inverse of temperature, the observed behavior suggests the shift in reversal field varies as the negative of the square of temperature. The observed exchange behavior is potentially due to barrier pinhole coupling, which has been observed and studied in magnetic recording media [6]. A better understanding of the formation, distribution, and temperature-dependent behavior of pinholes in barrier layers may aid in developing a more complete model of interlayer exchange coupling.

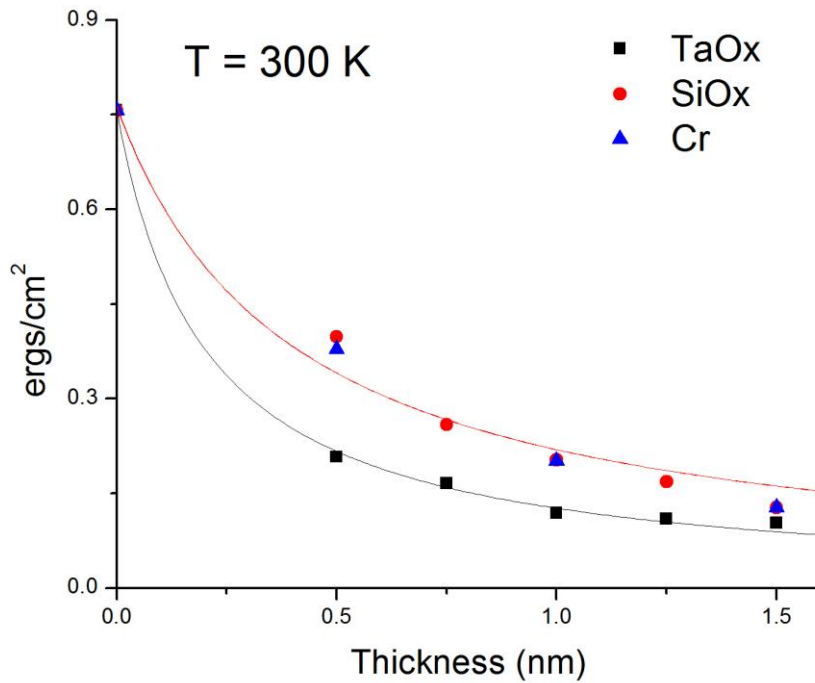


Figure 7-13 Thickness dependence of interlayer exchange coupling energy density for various barrier layer materials.

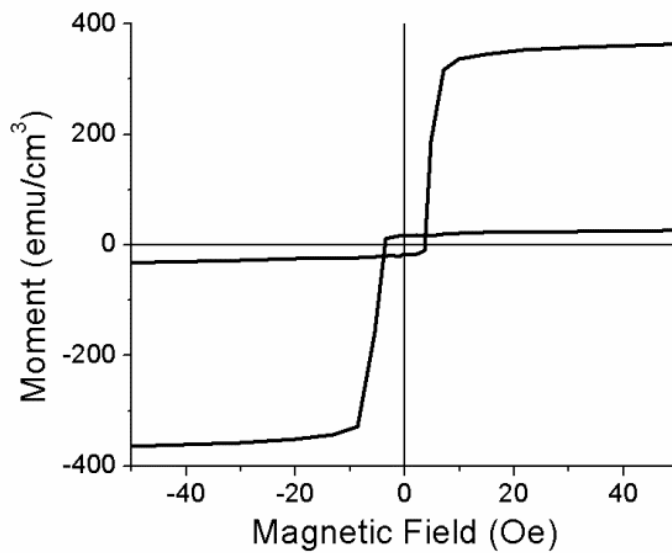


Figure 7-14 Enlarged view of antiferromagnetic behavior shown in hysteresis loop of film stack with 0.5 nm TaO<sub>x</sub> barrier layer at 700 K.

At 600 K and beyond, antiferromagnetic behavior was observed for all samples. An enlarged view of the hysteresis behavior is shown in FIG. 7-14. Samples that were exposed to measurement temperatures over 600 K showed a change in room temperature hysteresis behavior, most notably a large increase of in-plane coercivity. Samples which had only experienced measurement temperatures up to 550 K did not show these changes, instead maintaining the same room temperature hysteresis behavior. It is believed that the observed antiferromagnetic behavior is therefore due to interdiffusion and annealing effects in the soft FePt layer occurring at temperatures between 550 K and 600 K. Since full hysteresis curves were measured at each temperature, film stacks were exposed to high field and high temperature for several hours. It is likely that the soft FePt was annealed during this process. However, for exposure times much shorter than a second and operating temperatures much lower than examined in this study, as in typical STT-MRAM operation, interdiffusion and annealing effects are unlikely to play a significant role.

#### **7.4. Summary**

In this chapter, exchange coupled heterogeneous structures were studied as a way to develop MTJs with both high thermal stability and low critical switching current.

In Section 7.2,  $L1_0$ -FePt/MnAl heterogeneous structures were studied as a way to take advantage of STT potentially being a surface process. Such a structure could exhibit high effective PMA due to  $L1_0$ -FePt and low effective damping due to  $L1_0$ -MnAl. While high-PMA FePt was successfully grown, subsequently depositing MnAl at 300 °C and above resulted in interdiffusion between FePt and MnAl, which drastically degraded magnetic properties of the

film stack. Additions or substitutions to the film stack are likely necessary for further development of such heterogeneous structures.

In Section 7.3, high- and low-anisotropy thin films separated by a thin barrier were examined. FePt-based MTJ film stacks with thin, continuous barrier layers were fabricated and exchange coupling behavior for various barrier materials ( $\text{TaO}_x$ ,  $\text{SiO}_x$ , and Cr), barrier thicknesses, and measurement temperatures were investigated. It was found that exchange coupling energy varied inversely with barrier thickness, with significant exchange coupling energy still observed at barrier thicknesses of around 1 nm. Since scaled MTJs have tunnel barriers below 1 nm, interlayer exchange coupling between the electrodes may be used for partially pinning the free layer, thereby increasing effective anisotropy. Pinning a low-damping free layer by a high-anisotropy reference layer may therefore result in an MTJ with both high effective anisotropy and low effective damping. It was also found that exchange coupling energy decreased linearly with increasing temperature, and was well-behaved across different barrier materials and thicknesses. While the disappearance of exchange coupling near the Curie temperature of FePt agrees well with magnetic theory, the explanation for the linear dependence is less apparent. If the saturation magnetization varies as the inverse of temperature, the observed behavior suggests the shift in reversal field varies as the negative of the square of temperature. The observed antiferromagnetic behavior may be a result of annealing effects in the soft FePt layer as a byproduct of the experimental modeling method. Since full hysteresis curves were measured at each temperature, film stacks were exposed to high field and high temperature for extended periods of time. It is possible portions of the soft FePt were annealed while experiencing the local magnetic field generated by the hard FePt layer below. Hysteresis loops taken at room temperature after high temperature measurements indicated no significant changes

in magnetic properties up to 550 K. However, room temperature-measured coercivity increased once samples experienced measurement at 600 K and above. Nevertheless, for typical STT-MRAM operating temperatures, interdiffusion and annealing effects are unlikely to play a significant role, and exchange coupling can help pin the free layer at these lower temperatures.

These measurements of exchange coupling are also relevant to the application of FePt films for HAMR media, where it is desirable to exchange decouple the grains. For HAMR media applications, TaO<sub>x</sub> was shown to be the most effective segregant by a significant margin. Requiring a thinner layer than either SiO<sub>x</sub> or Cr to achieve the same exchange decoupling, media using TaO<sub>x</sub> segregant can potentially achieve higher grain density and therefore higher signal-to-noise ratio (SNR). Comparing segregants of equal thickness, TaO<sub>x</sub> resulted in negligible exchange coupling energies at slightly lower temperatures than the other segregants, possibly decreasing operating temperature, increasing media lifespan, and further increasing SNR by decreasing thermal noise during write operations.

Overall, this chapter demonstrated that there is potential for exploiting exchange coupling in heterogeneous MTJ structures to achieve both high PMA and low damping. While significant challenges were seen in developing a coupled FePt/MnAl electrode in Section 7.2, the results in Section 7.3 showed that interlayer exchange coupling can cross a thin barrier in a high-anisotropy electrode/barrier/low-anisotropy electrode structure. To take advantage of this, FePt/MgO/MnAl film stacks for MTJs will be explored in Chapter 8.

## 7.5. References

- [1] I. Yulaev, M. V. Lubarda, S. Mangin, V. Lomakin, and E. E. Fullerton, “Spin-transfer-torque reversal in perpendicular anisotropy spin valves with composite free layers,” *Appl. Phys. Lett.*, vol. 99, p. 132502, 2011.
- [2] V. Sokalski, D. E. Laughlin, and J.-G. Zhu, “Experimental modeling of intergranular exchange coupling for perpendicular thin film media,” *Appl. Phys. Lett.*, vol. 95, no. 10, p. 102507, 2009.
- [3] S. D. Granz and M. H. Kryder, “Intergranular Exchange Coupling in FePt:X:FePt (X=B, C, SiO<sub>x</sub>, Cr and TaO<sub>x</sub>) Thin Films for Heat Assisted Magnetic Recording,” *IEEE Trans. Magn.*, vol. 48, no. 11, pp. 2746–2748, Nov. 2012.
- [4] S. D. Granz, “Granular L1<sub>0</sub> FePt:X (001) Thin Films for Heat Assisted Magnetic Recording,” Ph.D. Dissertation, Carnegie Mellon University, Pittsburgh, PA, 2012.
- [5] E. Y. Huang and M. H. Kryder, “Effects of temperature on intergranular exchange coupling in L1<sub>0</sub>-FePt thin films,” *J. Appl. Phys.*, vol. 115, no. 21, p. 213906, Jun. 2014.
- [6] G. Hass, *Physics of Thin Films, Vol. 6*. New York, London: Academic Press, 1971.

## Chapter 8

# FePt/MgO/MnAl Film Stacks for Perpendicular Magnetic Tunnel Junctions (pMTJs)

### 8.1. Introduction

In Chapter 7, exchange coupled heterogeneous structures for the purpose of producing MTJs with both high effective PMA and low effective damping were studied [1]. The results showed promise in taking advantage of cross-barrier exchange coupling between high-anisotropy and low-damping electrodes.

In this chapter, this idea is pursued and  $L1_0$ -ordered FePt/MgO/MnAl for perpendicular magnetic tunnel junctions (pMTJs) are explored. Such a structure could potentially demonstrate both high thermal stability due to high-PMA  $L1_0$ -FePt [2], [3] and low critical switching current due to low-damping  $L1_0$ -MnAl [4]–[6].

### 8.2. Experimental Details

In this study, 1” Si (100) wafers were used as substrates. Wafers were dipped in buffered hydrofluoric acid for 20 seconds prior to loading into the sputtering chamber to strip the native oxide and promote textured growth of MgO (001). Films were sputter-deposited in the Leybold-Heraeus Z-400 Sputtering System #2 at base pressures below  $3 \times 10^{-7}$  Torr. Film stacks had the structure buffer HF-cleaned Si substrate/MgO (5 nm)/FePt (10)/MgO (0.25-5)/MnAl (10). First,

the substrate was heated *in situ* to 425 °C, which helped promote MgO (001) texture. A 5 nm MgO seed layer was then RF sputtered onto the Si substrate. Next, a 10 nm FePt film was RF sputtered. The substrate was allowed to cool to near room temperature, and a 0.25-5 nm MgO barrier layer was subsequently RF sputtered. Finally, the substrate was heated *in situ* to 400 °C and a 10 nm MnAl film was then DC magnetron sputtered from a vacuum hot-pressed Mn<sub>48</sub>Al<sub>52</sub> target. Microstructure and magnetic properties of the film stacks were investigated using TEM and PPMS.

### 8.3. Results and Discussion

Film stacks of buffer HF-cleaned Si substrate/MgO (5 nm)/FePt (10)/MgO (0.25-5)/MnAl (10) with varying MgO barrier layer thickness were fabricated and characterized, with corresponding out-of-plane magnetic hysteresis loops shown in FIG. 8-1. The saturation magnetization is seen to increase with increasing MgO barrier layer thickness, a relationship plotted in FIG. 8-2. Just as in Section 7.2, the reduction in  $M_s$  suggests interdiffusion between FePt and MnAl with MgO barrier layer thickness below 2 nm. Further evidence for this can be seen in the TEM cross-sectional image of a film stack with 1 nm MgO barrier, displayed in FIG. 8-3. The image shows lattice fringes indicating ordering in the dark FePt grains and the upper portions of the lighter MnAl material, but a large amorphous region around the MgO barrier layer. The thin 1 nm MgO film is unable to form a continuous barrier layer due to the large grain size and high roughness of the FePt, which can be seen more clearly in FIG. 8-4.

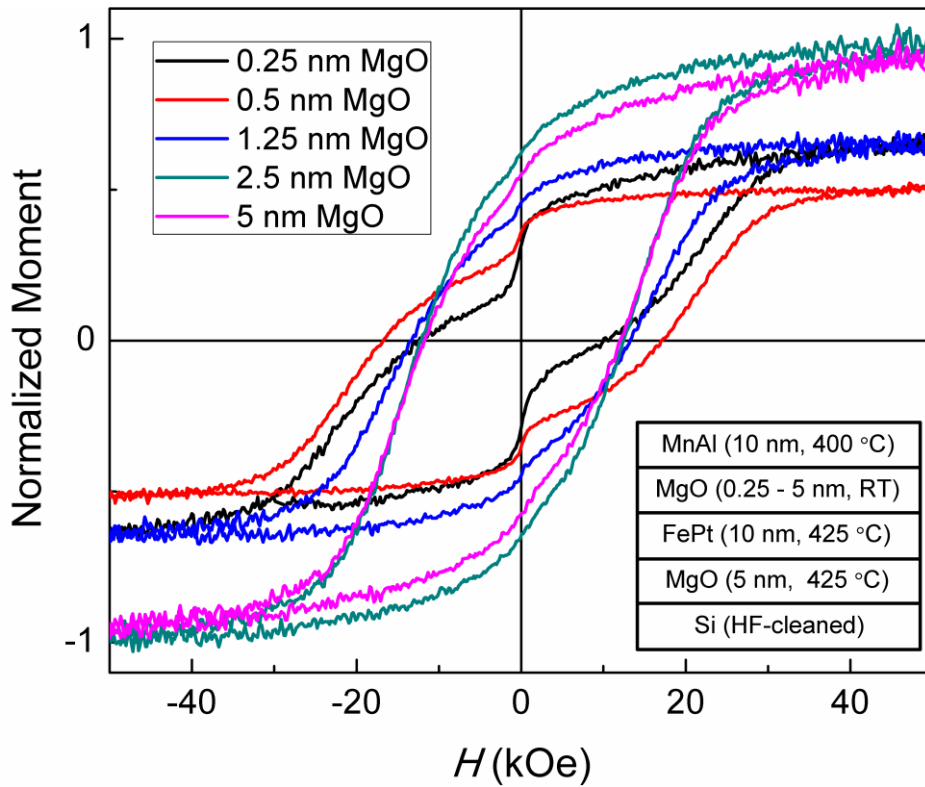


Figure 8-1 Out-of-plane magnetic hysteresis loops of buffer HF-cleaned Si substrate/MgO (5 nm)/FePt (10)/MgO (0.25-5)/MnAl (10) film stacks with varying MgO barrier layer thickness.

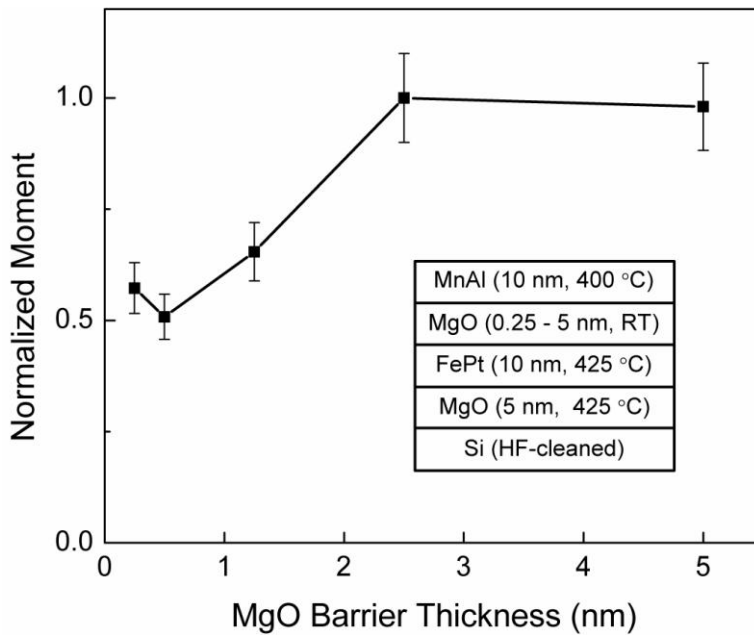


Figure 8-2 MgO barrier layer thickness dependence of saturation magnetization  $M_s$  of buffer HF-cleaned Si substrate/MgO (5 nm)/FePt (10)/MgO (0.25-5)/MnAl (10) film stacks.

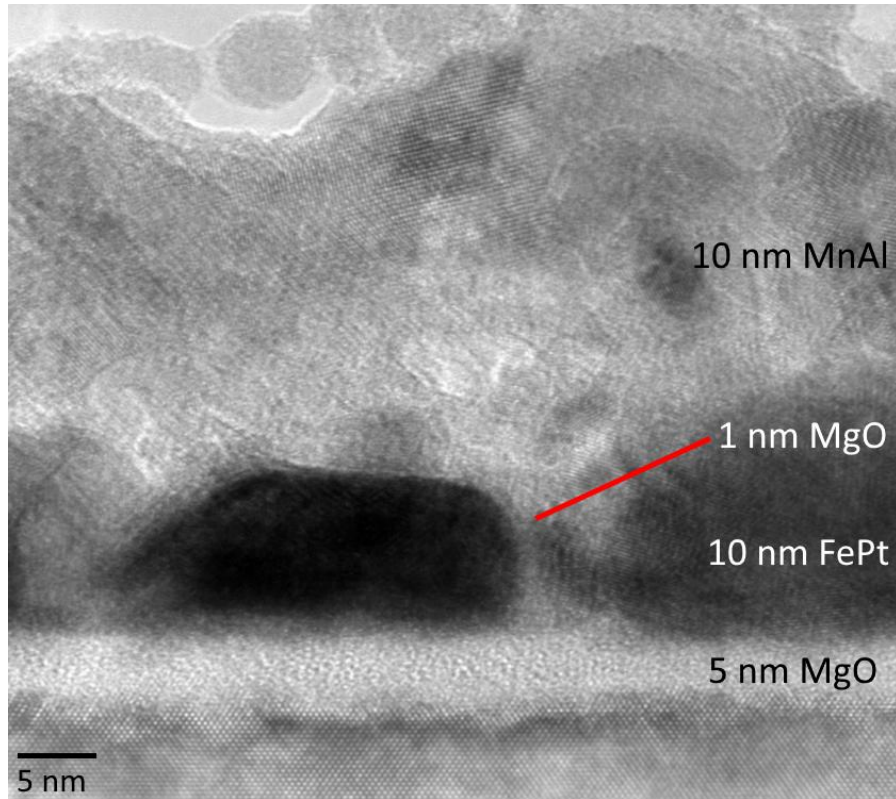


Figure 8-3 Cross-sectional TEM image of buffer HF-cleaned Si substrate/MgO (5 nm)/FePt (10)/MgO (1)/MnAl (10) film stack.

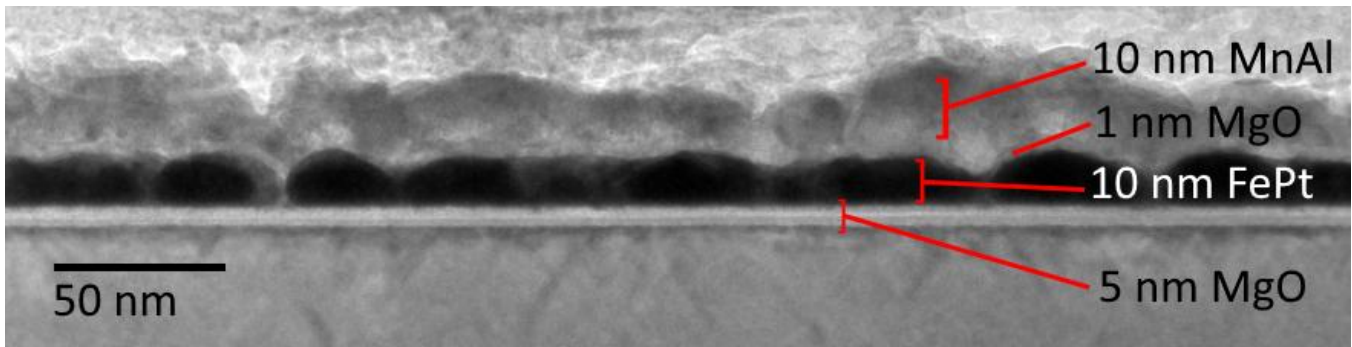


Figure 8-4 Cross-sectional TEM image of buffer HF-cleaned Si substrate/MgO (5 nm)/FePt (10)/MgO (1)/MnAl (10) film stack showing large FePt grains and high film roughness.

On the other hand, film stacks with at least 2 nm of MgO, such as the one with 2 nm MgO shown in FIG. 8-5, do not appear to have the same problem of interdiffusion. From the TEM image, lattice fringes can be seen in the MnAl very near the MgO barrier layer.

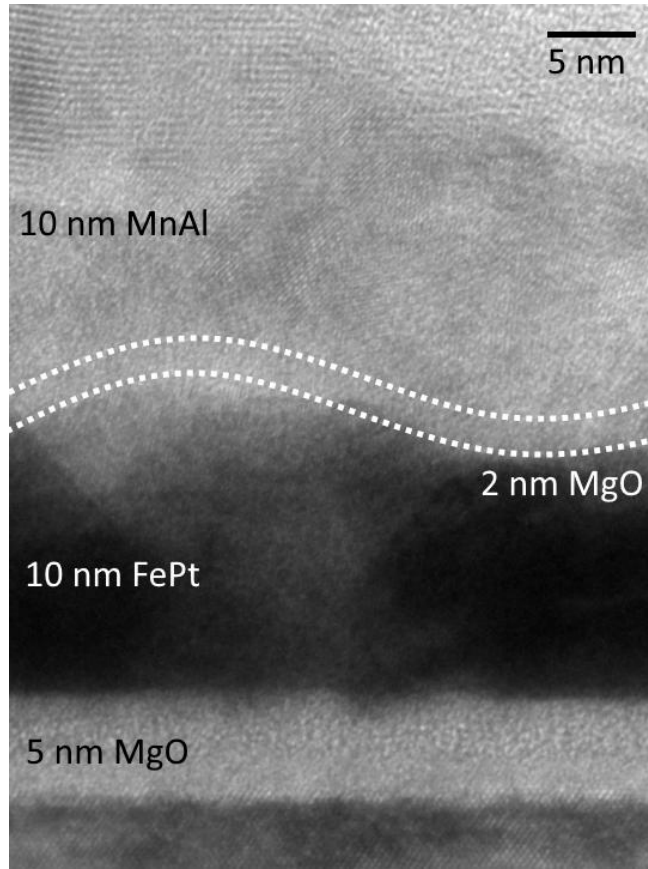


Figure 8-5 Cross-sectional TEM image of buffer HF-cleaned Si substrate/MgO (5 nm)/FePt (10)/MgO (2)/MnAl (10) film stack.

To isolate the magnetic behavior of the MnAl layer, the hysteresis loop of a reference FePt film was subtracted from the loops shown in FIG. 8-1. The results, plotted in FIG. 8-6, indicate a dramatic increase in PMA of the MnAl with increasing MgO barrier layer thickness. This agrees with the previous discussion on interdiffusion. Furthermore, the calculated MnAl contribution in the film stack with 5 nm of MgO is remarkably similar to the measured hysteresis behavior of the Si substrate/MgO (20 nm)/MnAl (30)/Ta (5) film stack optimized in Chapter 4. The data therefore suggest that an FePt/MgO/MnAl MTJ film stack has been developed with high PMA in both electrodes when the MgO thickness is sufficient to prevent interdiffusion, which in this case is about 2 nm.

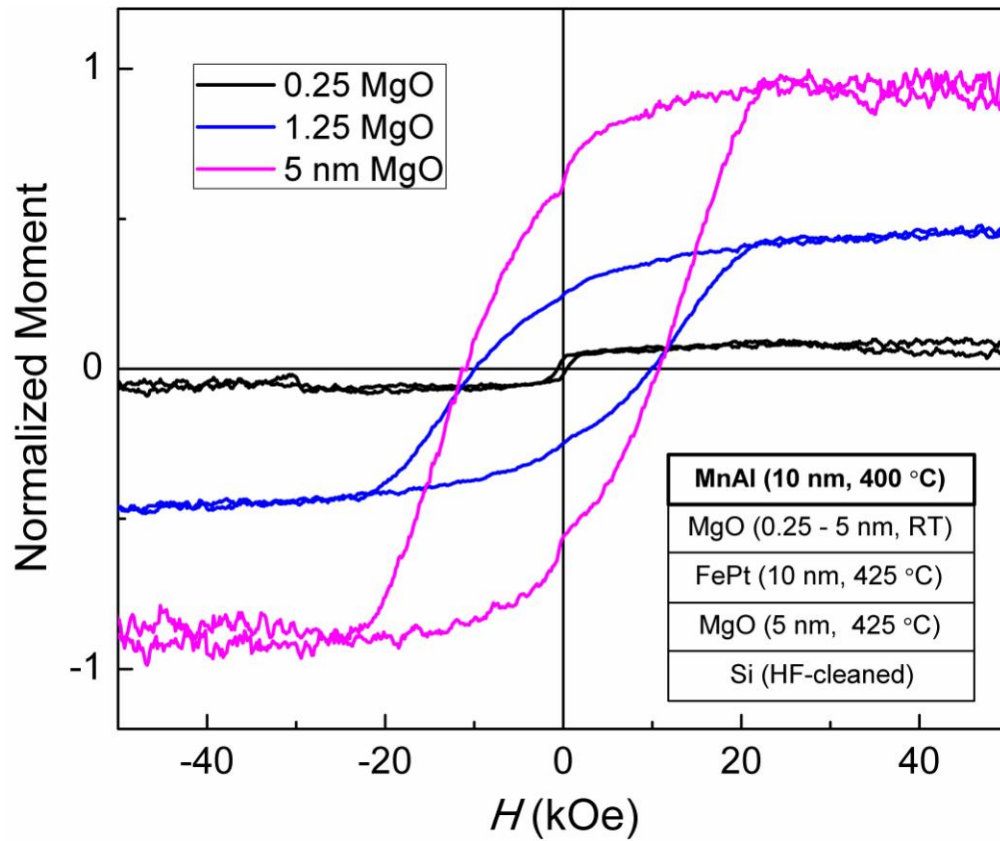


Figure 8-6 Calculated MnAl contribution to out-of-plane magnetic hysteresis loops of buffer HF-cleaned Si substrate/MgO (5 nm)/FePt (10)/MgO (0.25-5)/MnAl (10) film stacks.

## 8.4. Summary

In this chapter,  $L1_0$ -ordered FePt/MgO/MnAl film stacks for pMTJs were explored. Film stacks of buffer HF-cleaned Si substrate/MgO (5 nm)/FePt (10)/MgO (0.25-5)/MnAl (10) with varying MgO barrier layer thickness were fabricated and characterized. From cross-sectional TEM images and magnetic hysteresis loops, it was inferred that film stacks with MgO barrier layer thickness below 2 nm experience significant interdiffusion between the FePt and MnAl. On the other hand, TEM images of film stacks with MgO barrier layers greater than 2 nm showed clear lattice fringes indicating good ordering in the MnAl film, and calculated magnetic hysteresis contributions of the MnAl further supported this conclusion.

Overall, these results show potential for using  $L1_0$ -ordered materials for pMTJs. The results in Section 7.3 demonstrated thin, continuous barrier layers can be achieved for in-plane  $L1_0$ -FePt. With further materials exploration and fabrication optimization, similar results may be possible for  $L1_0$ -ordered materials with high PMA. Additionally, the interdiffusion seen in this chapter may also be alleviated by smoother films. Taken together, the work discussed here and in Chapter 7 suggest interlayer exchange coupling may be useful across a tunnel barrier, potentially enabling  $L1_0$ -based MTJs with both high PMA and low damping. Such a structure could help realize scalable STT-MRAM devices that simultaneously have both high thermal stability and low critical switching current.

## 8.5. References

- [1] I. Yuliev, M. V. Lubarda, S. Mangin, V. Lomakin, and E. E. Fullerton, “Spin-transfer-torque reversal in perpendicular anisotropy spin valves with composite free layers,” *Appl. Phys. Lett.*, vol. 99, p. 132502, 2011.
- [2] S. D. Granz, “Granular  $L1_0$  FePt:X (001) Thin Films for Heat Assisted Magnetic Recording,” Ph.D. Dissertation, Carnegie Mellon University, Pittsburgh, PA, 2012.
- [3] C. S. Kim, “Feasibility of a Multi-bit Cell Perpendicular Magnetic Tunnel Junction Device,” Ph.D. Dissertation, Carnegie Mellon University, Pittsburgh, PA, 2013.
- [4] M. Hosoda, M. Oogane, M. Kubota, T. Kubota, H. Saruyama, S. Iihama, H. Naganuma, and Y. Ando, “Fabrication of  $L1_0$ -MnAl perpendicularly magnetized thin films for perpendicular magnetic tunnel junctions,” *J. Appl. Phys.*, vol. 111, no. 7, p. 07A324, 2012.
- [5] L. J. Zhu, S. H. Nie, and J. H. Zhao, “Recent progress in perpendicularly magnetized Mn-based binary alloy films,” *Chin. Phys. B*, vol. 22, p. 118505, 2013.
- [6] E. Y. Huang and M. H. Kryder, “ $L1_0$ -Ordered MnAl Thin Films With High Perpendicular Magnetic Anisotropy Using TiN Underlayers on Si Substrates,” *IEEE Trans. Magn.*, vol. 51, no. 11, pp. 1–4, Nov. 2015.

# Chapter 9

## Conclusion

### 9.1. Summary of Present Work

The objective of the research conducted herein was to develop  $L1_0$ -ordered materials and thin film stack structures with high perpendicular magnetic anisotropy (PMA) for spin-transfer-torque magnetoresistive random access memory (STT-MRAM) applications. A systematic approach was taken in this dissertation, culminating in exchange coupled  $L1_0$ -FePt and  $L1_0$ -MnAl heterogeneous structures showing great promise for developing perpendicular magnetic tunnel junctions (pMTJs) with both high thermal stability and low critical switching current.

First,  $L1_0$ -ordered MnAl was identified as a suitable candidate material for use in pMTJs for STT-MRAM applications. Its high PMA would enable scalability and high retention, while its low Gilbert damping would allow for low operating power. The existing body of work on the structurally similar  $L1_0$ -FePt could also be leveraged. Using MgO underlayers on Si substrates, sputtered MnAl films were systematically optimized, ultimately producing a Si substrate/MgO (20 nm)/MnAl (30)/Ta (5) film stack, deposited at  $T_s = 530$  °C, that exhibited a high degree of ordering ( $S = 0.94$ ) and large PMA, with out-of-plane  $H_c$  of 8 kOe,  $K_u$  of  $6.5 \times 10^6$  erg/cm<sup>3</sup>,  $M_s$  of 300 emu/cm<sup>3</sup>, and  $M_r/M_s$  of 0.8.

Noting the incompatibility of insulating MgO underlayers with industrial-scale CMOS processes, attention was turned to using conductive underlayers. TiN can be DC sputtered for high deposition rates and is widely used in the semiconductor industry in contacts, with good

conductivity as well as thermal and mechanical reliability. When deposited on buffer HF-cleaned Si substrates, TiN easily formed the (001) texture, which excelled at promoting growth of  $L1_0$ -MnAl. Optimized films of 50 nm MnAl deposited at  $T_s = 400$  °C showed high PMA, with out-of-plane  $H_c$  of 12 kOe,  $K_u$  of  $1.0 \times 10^7$  erg/cm<sup>3</sup>,  $M_s$  of 250 emu/cm<sup>3</sup>, and squareness  $M_r/M_s$  of 0.9. Attempts to use conductive (Mg<sub>0.2</sub>Ti<sub>0.8</sub>)O underlayers did not produce MnAl films with significantly altered growth morphology or improved PMA. The studies confirmed that there are narrow regions of deposition conditions for producing  $\tau$ -MnAl films with high PMA. In particular, the underlayer system and *in situ* deposition temperature are especially important. It was found that the high deposition temperatures contributed to high film roughness. Keeping MnAl films below 10 nm also helped reduce film roughness.

In an effort to reduce ordering temperature and surface roughness of  $L1_0$ -MnAl films, adding other materials (Ni, C, and SiO<sub>x</sub>) to the MnAl film while using various underlayers in conjunction with additions to MnAl was studied. MnAl:Ni films with 3 volume% Ni content deposited on TiN underlayers revealed that surface roughness increased dramatically below the ordering temperature. MnAl:C films with 1 volume% C showed an increase in PMA, while C in excess of the solubility limit (1.7 atomic %) diffused to the grain edges, degrading PMA. MnAl:SiO<sub>x</sub> films demonstrated poor PMA.

Different post-deposition methods, rather than *in situ* annealing were then studied to reduce surface roughness. Rapid thermal annealing (RTA) was found to produce PMA in films at lower annealing temperatures than tube furnace annealing, but tube furnace annealing produced films with higher maximum PMA. However, both processes produced films with lower PMA than *in situ* annealing. Closer examination of microstructure suggested nucleation as an important process in determining PMA of films, with a moderate number of nucleation sites at

the TiN/MnAl interface producing annealed samples with the highest PMA while keeping surface roughness low. However, the PMA of all samples ordered primarily through annealing showed significantly lower PMA (coercivity  $< 1.5$  kOe) than previously optimized samples ordered through high *in situ* deposition temperature (coercivity 8-12 kOe).

As a way to potentially mitigate roughness issues arising from using MnAl-based thin films as both free and reference layers in an MTJ, exchange coupled heterogeneous structures were studied. With careful design and material selection, such structures could achieve both high thermal stability and low critical switching current. Given the high PMA of  $L1_0$ -FePt and low damping of  $L1_0$ -MnAl,  $L1_0$ -FePt/MnAl heterogeneous structures were studied as a way to take advantage of STT potentially being a surface process. High-PMA FePt coupled to moderate-PMA MnAl was successfully grown, though attempting to deposit the MnAl at 300 °C and above resulted in interdiffusion between the two materials, which drastically degraded magnetic properties of the film stack. High- and low-anisotropy thin films separated by a thin barrier were examined in the form of in-plane hard-FePt/barrier layer/in-plane soft-FePt film stacks. By investigating the exchange coupling behavior of the FePt layers across different barrier materials ( $TaO_x$ ,  $SiO_x$ , and Cr), thicknesses and measurement temperatures, it was found that significant exchange coupling energy was still observed at barrier thicknesses of around 1 nm. Since scaled MTJs have tunnel barriers below 1 nm, interlayer exchange coupling between the electrodes may be used for partially pinning the free layer, thereby increasing effective PMA. Pinning a low-damping free layer by a high-PMA reference layer may therefore result in an MTJ with both high effective PMA and low effective damping. It was also found that exchange coupling energy decreased linearly with increasing temperature, and was well-behaved across different barrier materials and thicknesses.

Lastly, heterogeneous  $L1_0$ -ordered FePt/MgO/MnAl film stacks were explored for pMTJs. Film stacks with MgO barrier layers thinner than 2 nm showed significant interdiffusion between the FePt and MnAl, while film stacks with thicker MgO barrier layers exhibited good ordering and high PMA in both the FePt and MnAl films.

## 9.2. Conferences and Publications

Chapter 4 described the optimization of MnAl thin films on silicon, with an optimized film stack structure of Si substrate/MgO (20 nm)/MnAl (30)/Ta (5) showing out-of-plane  $H_c$  of 8 kOe,  $K_u$  of  $6.5 \times 10^6$  erg/cm<sup>3</sup>,  $M_s$  of 300 emu/cm<sup>3</sup>, and  $M_r/M_s$  of 0.8. Significant portions of this work were presented at the 59<sup>th</sup> Magnetism and Magnetic Materials Conference in Honolulu, 2014, and published in the Journal of Applied Physics, Reference [1].

Chapter 5 described the investigation of TiN as an underlayer for growing  $L1_0$ -ordered MnAl thin films on silicon, with an optimized film stack structure of Si substrate/TiN (10 nm)/MnAl (50)/Ta (5) showing out-of-plane  $H_c$  of 12 kOe,  $K_u$  of  $1.0 \times 10^6$  erg/cm<sup>3</sup>,  $M_s$  of 250 emu/cm<sup>3</sup>, and  $M_r/M_s$  of 0.9. Significant portions of this work were presented at the Intermag Conference in Beijing, 2015, and published in the IEEE Transactions on Magnetics, Reference [2].

Section 7.3 described the study of interlayer exchange coupling between high- and low-anisotropy in-plane FePt thin films separated by a thin barrier, characterizing the well-behaved, linear dependency of exchange coupling energy on measurement temperature and inverse dependency on barrier layer thickness. Significant portions of this work were presented at the 58<sup>th</sup> Magnetism and Magnetic Materials Conference in Denver, 2013, and published in the Journal of Applied Physics, Reference [3].

Chapter 8 described the characterization of FePt/MgO/MnAl film stacks for pMTJs, with fabricated samples suggesting high PMA in both ferromagnetic layers when using MgO barrier layers at least 2 nm thick. Significant portions of this work were submitted for presentation at the 61<sup>st</sup> Magnetism and Magnetic Materials Conference in New Orleans, 2016, and will be submitted for publication in AIP Advances.

### 9.3. Recommendations for Future Work

In order to realize scalable, low-power STT-MRAM, pMTJs with both high effective PMA and low effective damping must first be developed. While the progress on  $L1_0$ -ordered thin films discussed in this dissertation is encouraging, significant challenges remain. In light of this, below are some directions that may be worth pursuing.

1. Explore/modify underlayer and capping layer systems for promoting growth of  $L1_0$ -ordered films. TiN has proven to be a very good seed layer for this, but a modified underlayer system that promotes improved film wetting and reduced agglomeration may further reduce  $L1_0$ -MnAl ordering temperature and therefore film roughness. Appropriate capping layers may also promote ordering at the film surface while keeping film roughness low by restricting agglomeration and clumping. For example, Liao et al. have successfully used  $\text{FeO}_x$  capping layers to order 4 nm thick, continuous FePt films while reducing the film roughness [4].
2. More in-depth study of adding materials to MnAl thin films. Given the equipment available, film compositions were difficult to adjust. The method of alternating nominally sub-nanometer layers of materials inherently had large margins of error. A sweep with finer

material compositions may reveal methods of reducing MnAl ordering temperature and film roughness.

3. Examine annealing tradeoffs more thoroughly, perhaps in the context of specific STT-MRAM applications. Depending on the target niche, certain performance aspects (speed, retention, power) are more important than others. It may be acceptable in particular circumstances to sacrifice one metric for another.
4. Develop exchange-coupled film stacks to achieve both high effective PMA and low effective damping. It would also be useful to study STT behavior of such heterogeneous systems electrically, to experimentally verify whether or not STT is truly a surface process.
5. Investigate effects of utilizing cross-barrier exchange coupling in pinning the free layer. MTJs employing heterogeneous structures can potentially exhibit both high thermal stability and low critical switching current.
6. Explore other  $L1_0$ -ordered materials with low damping. Many Mn-based alloys have been shown to be suitable, and may demonstrate different film morphologies and coupling behavior. FePt may also be a viable candidate, given the existing large body of research for its use in HAMR media. In that application, the low fly height of the head poses limitations on the roughness of the media film to be in the nanometer range. Some of the methods used in the HDD industry to achieve smooth films may therefore be adapted for pMTJs.

## 9.4. References

- [1] E. Y. Huang and M. H. Kryder, "Fabrication of MnAl thin films with perpendicular anisotropy on Si substrates," *J. Appl. Phys.*, vol. 117, no. 17, p. 17E314, May 2015.
- [2] E. Y. Huang and M. H. Kryder, " $L1_0$ -Ordered MnAl Thin Films With High Perpendicular Magnetic Anisotropy Using TiN Underlayers on Si Substrates," *IEEE Trans. Magn.*, vol. 51, no. 11, pp. 1–4, Nov. 2015.
- [3] E. Y. Huang and M. H. Kryder, "Effects of temperature on intergranular exchange coupling in  $L1_0$ -FePt thin films," *J. Appl. Phys.*, vol. 115, no. 21, p. 213906, Jun. 2014.
- [4] J.-W. Liao, K.-F. Huang, L.-W. Wang, W.-C. Tsai, W.-C. Wen, C.-C. Chiang, H.-J. Lin, F.-H. Chang, and C.-H. Lai, "Highly (001)-oriented thin continuous  $L1_0$  FePt film by introducing an  $\text{FeO}_x$  cap layer," *Appl. Phys. Lett.*, vol. 102, no. 6, p. 62420, 2013.